Pontifícia Universidade Católica
do Rio de Janeiro

Carlos Eduardo Sánchez Pérez

Microscale Flows of Thixotropic Liquids

Tese de Doutorado

Thesis presented to the Programa de Pós–graduação em Engenharia Mecânica of PUC-Rio in partial fulfillment of the requirements for the degree of Doutor em Engenharia Mecânica.

Advisor : Prof. Márcio da Silveira Carvalho
Co-advisor: Dr. Danmer Paulino Maza Quinones

Rio de Janeiro
May 2023

Pontifícia Universidade Católica
do Rio de Janeiro

Carlos Eduardo Sánchez Pérez

Microscale Flows of Thixotropic Liquids

Thesis presented to the Programa de Pós–graduação em Engenharia Mecânica of PUC-Rio in partial fulfillment of the requirements for the degree of Doutor em Engenharia Mecânica. Approved by the Examination Committee.

Prof. Márcio da Silveira Carvalho
Advisor
Departamento de Engenharia Mecânica – PUC-Rio

Dr. Danmer Paulino Maza Quinones
Co-advisor
Departamento de Engenharia Mecânica – PUC-Rio

Prof. Paulo Roberto de Souza Mendes
Departamento de Engenharia Mecânica – PUC-Rio

Prof. Roney Leon Thompson
Departamento de Engenharia Mecânica – UFRJ, Brazil

Prof. Cezar Otaviano Ribeiro Negrão
Departamento de Engenharia Mecânica e de Materiais – UFTPR, Brazil

Prof. Jaewook Nam
School of Chemical and Biological Engineering – SNU, South Korea

Rio de Janeiro, May the 12th, 2023

Carlos Eduardo Sánchez Pérez

Carlos Sanchez received a bachelor's degree in Chemical Engineering from Universidad de Los Andes (ULA-Venezuela) in 2003 and a master's degree in Natural Gas Technology from NTNU-Norway in 2012.

Bibliographic data

Sánchez Pérez, Carlos Eduardo

Microscale Flows of Thixotropic Liquids / Carlos Eduardo Sánchez Pérez; advisor: Márcio da Silveira Carvalho; co-advisor: Danmer Paulino Maza Quinones. – 2023.

111 f.: il. color. ; 30 cm

Tese (doutorado) - Pontifícia Universidade Católica do Rio de Janeiro, Departamento de Engenharia Mecânica, 2023

Inclui bibliografia

1. Engenharia Mecânica – Teses. 2. tixotropia;. 3. modelo independente no tempo;. 4. suspensões de partículas;. 5. fluidez;. 6. histerese;. I. Carvalho, Márcio. II. Maza, Danmer. III. Pontifícia Universidade Católica do Rio de Janeiro. Departamento de Engenharia Mecânica. IV. Título.

CDD: 621

I dedicate this work to my parents.

Acknowledgments

To my family, especially to my parents, for their support and inspiration besides the long physical distance between us.

To my advisor, Prof. Márcio Carvalho, for his trust and excellent technical guidance. His vast knowledge and experience has encouraged me throughout all my academic research.

To my co-advisor, Dr. Danmer Maza, for your invaluable help in many aspects of my academic research. He was very important in incorporating the time-independent model and the thixotropic model into the existing software.

To Professor, Paulo Roberto de Souza Mendes, for helping us during the first steps of this work. His help was very important in the selection of the thixotropic model and its understanding.

To the researchers, Dr. Jorge Avendano and his wife Lisbeth Manchego, for helping and guiding me when I arrived to Brazil and Rio de Janeiro.

To my colleagues and research staff of the LMMP group for their friendship and good times shared during these years.

To CNPq, CAPES and PUC-Rio, for the funding without which this research could not have been accomplished.

This study was financed in part by the Coordenação de Aperfeiçoamento de Pessoal de Nível Superior - Brasil (CAPES) - Finance Code 001.

Abstract

Sánchez Pérez, Carlos; Carvalho, Márcio (Advisor); Maza, Danmer (Co-Advisor). **Microscale Flows of Thixotropic Liquids**. Rio de Janeiro, 2023. 111p. Tese de doutorado – Departamento de Engenharia Mecânica, Pontifícia Universidade Católica do Rio de Janeiro.

Many particle suspensions behave as thixotropic-viscous materials and they are present in different industrial processes, including coating applications. Specifically, the production of battery electrodes involves slot coating of a thixotropic liquid. In most cases, the flow of slurries and other particle suspensions is described by using a time-independent model that assumes the viscosity to be solely a function of the local deformation rate. However, the viscosity of thixotropic fluids is associated to the evolution of its microstructuring level, which does not change instantaneously with the shear stress (or deformation rate). In the case of imposing constant shear stress (or shear rate), the microstructure evolves until reaching an equilibrium state; but this process takes time. Even in a steady-state flow, the liquid flows through regions where there are significant changes in the levels of shear stress and the flow is transient in a Lagrangian point of view. Therefore, assuming that the viscosity at each point of the flow is the steady-state viscosity described by a time-independent model may lead to an inaccurate flow description. The relative magnitude of the characteristic response time of the liquid and the residence time of the flow becomes an important parameter. This is particularly relevant in small scale flows with very small residence time. Flows of a thixotropic-viscous liquid through a constricted microcapillary and in a slot coating process were analyzed here using two rheological models: a time-independent model (TIM) and a thixotropic model that takes into account the liquid time-dependent response. The resulting set of fully coupled, non-linear equations was solved by the Galerkin and SUPG Finite Element Method. The results show that the use of a TIM to describe thixotropic viscous materials, such as some particle suspensions, can lead to very large errors on the predicted flow behavior. Furthermore, time-independent models are not able to predict complex flow phenomena, like hysteresis, which could lead to unstable flows. These inaccuracies highlight the need for a more complete model that takes into account time-dependency of the flowing liquid in a certain range of flow parameters.

Keywords

thixotropy; time-independent model; particle suspensions; fluidity; hysteresis;

Resumo

Sánchez Pérez, Carlos; Carvalho, Márcio; Maza, Danmer. **Escoamentos a Microescala de Líquidos Tixotrópicos**. Rio de Janeiro, 2023. 111p. Tese de Doutorado – Departamento de Engenharia Mecânica, Pontifícia Universidade Católica do Rio de Janeiro.

Muitas suspensões de partículas se comportam como materiais tixotrópicos e estão presente em muitos processos industriais, incluindo aplicações de revestimentos de filmes finos. Especificamente, operações de extrusão de fluidos tixotrópicos estão envolvidos na produção de eletrodos de baterias. Na maioria dos casos, o escoamento de suspensões de partículas é descrito por modelos independentes no tempo, que assumem que a viscosidade como uma função somente da taxa local de deformação local. No entanto, a viscosidade dos fluidos tixotrópicos é associada com a evolução do seu nível de microestruturação que não muda instantaneamente com a tensão (ou taxa de deformação). No caso da imposição de uma tensão constante (ou taxa de cisalhamento), a microstrutura evolui até alcançar um estado de equilíbrio, porém este processo leva tempo. Mesmo em escoamentos em regime permanente, o líquido escoa através de regiões onde tem mudanças significativas nos níveis de tensão, sendo assim o escoamento transiente de um ponto de vista Lagrangiano. Então, assumir que a viscosidade, em todo ponto do escoamento, é à viscosidade em regime permanente pode gerar uma descrição errada do escoamento. A magnitude relativa do tempo de resposta do líquido e do seu tempo de residência torna-se num parâmetro importante, especialmente em escoamentos em pequena escala com tempos de residência muito curtos. O escoamento de um líquido tixotrópico através de um microcapilar com constrição e no processo de revestimento por extrusão foram analisados aqui, usando dois modelos reológicos: um modelo independente no tempo (TIM) e um modelo tixotrópico que leva em conta a resposta transiente do líquido. O conjunto de equações não lineares foi resolvido utilizando o método de Galerkin/SUPG de elementos finitos. Os resultados mostram que o uso de um modelo simples TIM para descrever materiais tixotrópicos, como suspensões de partículas, pode levar a erros muito significativos na predição do comportamento de escoamento. Além disso, os modelos independentes no tempo não têm a capacidade de predizer certos fenômenos de escoamento, como a histerese, que pode gerar escoamentos instáveis. Essas imprecisões indicam a necessidade de usar um modelo mais completo que considere a resposta transiente do líquido.

Palavras-chave

tixotropia; modelo independente no tempo; suspensões de partículas; fluidez; histerese;

Table of contents

List of figures

List of tables

List of Abbreviations and Symbols

Abbreviations

TEVP	-	Thixotropic-elasto-viscoplastic
TVP	-	Thixotropic-viscoplastic
TV	-	Thixotropic-viscous materials
TIM	-	Time independent model
GNM	-	Generalized Newtonian model
HB	-	Herschel-Buckley model
expt'l data	-	Experimental data
PBM	-	Population balance models
SKM	-	Structural kinetics models
FDM	-	Finite difference method
FVM	-	Finite volume method
FEM	-	Finite element method
CFD	-	Computational Fluid Dynamics
SUPG	-	Streamline-Upwinding Petrov-Galerking
thix	-	Thixotropic

Greek Symbols

φ - Particle volume fraction
η - Local viscosity
$\dot{\gamma}$ - Shear rate
$\dot{\boldsymbol{\gamma}}$ - Strain rate tensor
η_0 - Zero-shear viscosity (Maximum viscosity)
η_∞ - Infinite-shear viscosity (Minimum viscosity)
σ - Shear stress intensity
$\boldsymbol{\sigma}$ - Shear stress tensor
σ_y - Yield stress
Ω_{cy} - Fitting parameter in Carreau-Yasuda model
η_{adj} - Fitting parameter
η_{solv} - Viscosity of the solvent
φ_m - Filling factor at maximum packing
φ_c - Crowding factor
$[\eta]$ - Intrinsic viscosity
κ - Rate constant
θ - Static contact angle (downstream)
θ_d - Dynamic contact angle (upstream)
θ_S - Static contact angle (upstream)
λ - Structure parameter
η_λ - Structural viscosity
$\eta_{\lambda=0}$ - Residual viscosity
η_S - Structural viscosity

Greek Symbols

γ_e - Elastic strain
γ_v - Viscous strain
γ - Total strain
Ψ_1 - Retardation time
Ψ_2 - Relaxation time
η_v - Total shear viscosity
$\ddot{\gamma}$ - Derivative of the shear rate
η_{SS} - Steady-state viscosity
λ_{SS} - Structure parameter at steady-state condition
ϕ_v - Total fluidity
ϕ_S - Structural fluidity
ϕ_∞ - Fluidity for a fully unstructured material
ϕ_0 - Fluidity for a fully structured material
ϕ_v^* - Normalized or dimensionless fluidity
ϕ_{eq}^* - Normalized equilibrium fluidity
σ_i - Initial Shear stress
σ_f - Final Shear stress
ρ - Density
ψ_i - Basis function in FEM
Ω - Domain
Γ - Domain's border
Ω^e - Element's Domain
Γ^e - Element Domain's border
ω - Element's coordinate
χ_i - Element's coordinate
Ω' - Computational Domain
Γ' - Computational Domain's border
Φ_j - Coefficient associated to ϕ_v
$\Delta \boldsymbol{C}$ - Increment of vector $\boldsymbol{C}$
ϵ - Tolerance of the Residuum norm
σ_w - Wall stress
ξ - Dimensionless distance
τ - Dimensionless wall stress
σ^* - Stress value when $\phi_{eq}^* = 0.95$
Λ - Thixotropy number
$\overline{\Delta P}$ - Ratio between pressure drops at the constriction
α - Dimensionaless downstream velocity

Roman Symbols

t_a - Avalanche time
t_c - Construction time
K - Consistency index
K' - Fitting factor
m - Fitting factor
n - Flow behavior index, number of terms in a summation
a - Fitting parameter in Carreau-Yasuda model
B - Einstein's coefficient
P_{vac} - Vacuum pressure
h - Thickness of the coated liquid layer
q - Volumetric flow rate per unit of width
V_w - Speed of the moving substrate
h_0 - Thickness of coated film for zero-vacuum pressure
h_{min} - Minimum thickness of coated film
t - Time
a, b, c, d, f, e - Fitting parameters of the evolution equation of λ
k_1 - Breakdown constant in evolution equation of λ
k_2 - Build-up constant in evolution equation of λ
J_S - Shear modulus of the microstructure
$\overset{\triangledown}{M}$ - Upper convective derivative
M - Generic variable
$\boldsymbol{v}$ - Velocity vector
^{T} - Index which denotes a transpose matrix or tensor
t_{eq} - Characteristic time of a liquid in evolution equation of λ
$F()$ - Function in fluidity evolution equation
$H()$ - Heaviside function
s - Exponent which depends on fluidity
$\boldsymbol{T}$ - Total stress tensor
$\boldsymbol{I}$ - Identity tensor
$\boldsymbol{b}$ - Body forces
p - Pressure
II - Second invariant of a tensor
tr - Trace of a tensor
c_i - Coefficient in FEM
R_c - Weighting residual of mass conservation equation
$\boldsymbol{R_m}$ - Weighting function in momentum conservation eq.
W_c - Weighting function in R_c
$\boldsymbol{W_m}$ - Weighting function in $\boldsymbol{R_m}$
m - Number of terms in a summation
$\boldsymbol{J}$ - Jacobian matrix
J_T - Jacobian transformation matrix
u - Velocity component in x direction
v - Velocity component in y direction
f_x - Force in x direction
f_y - Force in y direction

Roman Symbols

$\hat{\boldsymbol{n}}$ - Unit normal vector
U_j - Coefficient associated to u
V_j - Coefficient associated to v
P_j - Coefficient associated to p
$\boldsymbol{R}$ - Residual vector
$\boldsymbol{C}$ - FEM coefficient vector
$\boldsymbol{\mathcal{D}_\omega}$ - Symmetric tensor in elliptic mesh generation
$\boldsymbol{R_E}$ - Weighting residual of elliptic mesh equation
$\boldsymbol{W_E}$ - Weighting function in $\boldsymbol{R_E}$
R_t - Weighting residual of evolution equation of fluidity
W_t - Weighting function in R_t
h^U - Upwind coefficient in Petrov-Galerkin basis function
k - index associated to the number of the iteration
$\boldsymbol{J}^{-1}$ - Inverse of the Jacobian matrix
$\boldsymbol{u}$ - Velocity vector
f_b - Part of the function F
f_c - Part of the function F
u_{max} - Maximum velocity in x direction
r - Radial distance in cylindrical coordinates
z - Axial distance in cylindrical coordinates
Z - Axial distance in cylindrical coordinates
r_c - Critical radius
R - Radius of the capillary
D - Diameter of the capillary
d - Diameter at capillary's throat
${}_2F_1$ - Hypergeometric function
$(a)_i, (b)_i, (c)_i$ - Pochhammer symbols or rising factorial numbers
$(a^*)_i, (b^*)_i, (c^*)_i$ - Pochhammer symbols or rising factorial numbers
$(d)_i$ or $(d^*)_i$ - Parameter of a hypergeometric function
Q - Volumetric flow rate
$< u >$ - Average velocity
$\overline{D}$ - Dimensionless constriction ratio
l - Constriction length
$\bar{l}$ - Dimensionless constriction length
Str - Structure number
Mu - Mutation number
P_{amb} - Ambient pressure
P_{atm} - Atmospheric pressure
P_g - Gas pressure
P_{vac} - Pressure at vacuum box (absolute)
$P_{vac,g}$ - Pressure at vacuum box (gauge)
s_c - Arc length variable of the free surface
$\boldsymbol{t}$ - Tangent unit vector

Roman Symbols

X_{dcl} - Position of the dynamic contact line
X_{scl} - Position of the static contact line
b - Length of feed slot
x_c - Critical distance
H - Coating bead gap
G - Coating gap-film thickness ratio
S - Dimensionless feed slot height
$\overline{P_v}$ - Dimensionless vacuum pressure
f_I and f_{II} - Functions used in downstream slot coating analysis
$\boldsymbol{\wp}$ - Vector of flow parameters

1
Introduction

There are interesting and important fluids in industry and other human activities that do not show the linear Newtonian behavior. The mechanical behavior of complex liquids, such as polymeric solutions, waxy oils, muds, pharmaceutical and cosmetic products, paints, clay suspensions, processed food, among others [5, 10], cannot be described by a simple linear relationship between shear stress and rate of strain.

A common behavior of complex liquids is that the viscosity varies with the deformation rate, which is often modeled by empirical and time-independent models (TIM) like Bingham, Power-law and Carreau. Table 1.1 presents the functional form and corresponding parameters of these models.

Table 1.1: Selected rheological models at steady state condition

Name	Viscosity equation
Simple viscous models	
Power-law [11]	$\eta = K\dot{\gamma}^{n-1}$
Carreau - Yasuda [12]	$\eta = \eta_\infty + (\eta_0 - \eta_\infty)[1 + (\Omega_{cy}\dot{\gamma})^a]^{\frac{n-1}{a}}$
Visco-plastic models, for $\sigma \geq \sigma_y$	
Bingham [13]	$\eta = \sigma_y\dot{\gamma}^{-1} + K$
Herschel-Bulkley [14]	$\eta = \sigma_y\dot{\gamma}^{-1} + K\dot{\gamma}^{n-1}$
Lin et al. [15] (bentonite/laponite s.)	$\eta = \eta_{adj}(\sigma/\sigma_y)^{-1} + K'(\sigma/\sigma_y)^m + \eta_\infty$

σ: shear stress, σ_y: yield stress stress; K: consistency index; n: flow-behavior index; η_0: zero-shear viscosity; η_∞: infinite-shear viscosity ; η_{adj}, m, Ω_{cy}, and K' are fitting factors

The viscosity of the models presented in table 1.1 is solely a function of the shear rate. Examples of non-linear relations between the shear stress and shear rate for different fluids are shown in Fig. 1.1a. According to this non-linear behavior, non-Newtonian fluids can be subdivided into three groups: shear-thinning or pseudoplastic, viscoplastic, shear-thickening or dilatant [1].

Pseudoplasticity is the most common behavior of many different non-Newtonian fluids. It is characterized by the decrease of viscosity as shear rate increases. The fluids, which exhibit this behavior, are usually mathematically modeled by the Power-law and Carreau-Yasuda models (shown in table 1.1), where the value of n is lower than 1.

Dilatant fluids exhibit the opposite behavior to pseudoplasticity, the viscosity increases with increasing shear rate. They are also mathematically modeled by the Power-law, but $n>1$.

Viscoplasticity is characterized by the existence of yield stress, which must be exceeded before the liquid starts flowing (i.e. $\sigma \geq \sigma_y$). Otherwise, the material will deform elastically (or moves like a rigid body), if the external shear stress applied (σ) is lower than the yield stress [1]. Viscoplastic fluids are usually modeled by Bingham and Herschel-Bulkley models. A Bingham plastic fluid has a linear flow curve for $\sigma \geq \sigma_y$. In a most general fashion, viscoplastic fluids are usually characterized by Herschel-Bulkley model.

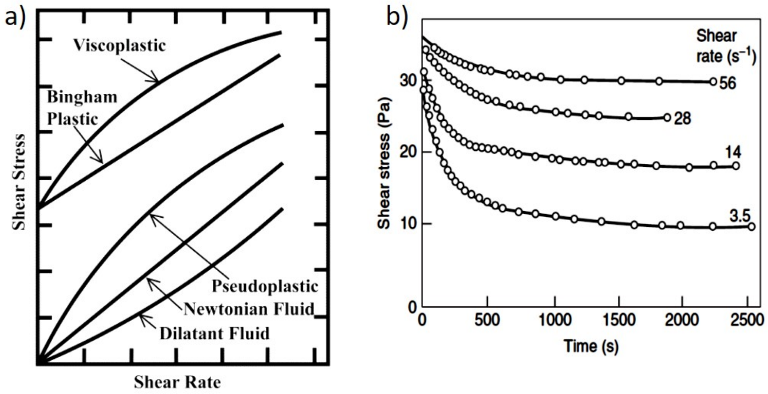

Figure 1.1: Time-independent vs time-dependent viscosity fluids: a) Different kind of time-independent non-Newtonian fluids, b) Representative data showing thixotropy in a 54% (by weight) red mud suspension [1]

The viscosity of a liquid as a function of shear rate is usually measured in rotational rheometers, where a shear rate is imposed according to the selected rotational velocity. Then, the resulting torque is measured and the corresponding shear stress is evaluated. The local viscosity is just the ratio between shear stress and shear rate. At each imposed shear rate, it takes some time for the shear stress to reach a steady state in complex liquids, as indicated in Fig. 1.1b. This time-dependent behavior is associated with the evolution of the liquid microstructure. For instance, many particle suspensions, like that shown Fig. 1.1b, show a viscosity dependence on both shear rate and time. In the example shown in Fig. 1.1b , the steady values are just achieved for times larger than 2000 s at the lowest shear rate.

1.1
Definition of thixotropy

Freundlich [16] introduced the term of thixotropy, when rheology was emerging as a discipline. However, the term was coined, by Peterfi [17], from the Greek words: Θίξιζ (**Thixis**: shaking or shearing) and τρέπω (**Trepos**: turning or changing). Nowadays, thixotropy is generally defined as: continuous decrease of viscosity with time, while a constant stress is applied to a sample that has been previously at rest, and the subsequent recovery of viscosity in time as the flow ceases [5, 18]. Time-dependence also implies "fluid memory" which is associated with shear history [5].

Thixotropy is usually associated with reversible microscopic arrangements of the particles in a suspension [2, 5, 9, 18, 19, 20, 21]. Different microstructure arrangements, and their effect on the macroscopic rheological properties of thixotropic materials, are illustrated in Fig. 1.2. Initially, there is a highly structured material that is not flowing. However, if this material is under shaking or shearing it will start flowing. Eventually, the liquid will be completely unstructured and its viscosity may achieve a minimum value. As this process is reversible, if the material is allowed to rest, the initial microscopic arrangement is recovered when the liquid stops flowing.

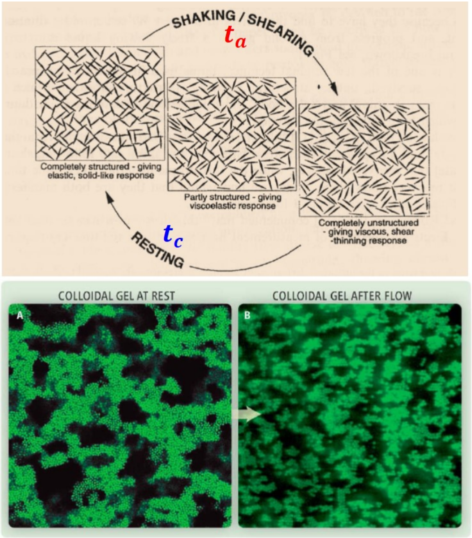

Figure 1.2: Sketch of breakdown and build-up of a 3D thixotropic structure. t_a and t_c are the characteristic times of the thixotropic material (Adapted from [2, 3])

The times associated to changes in the particle arrangement at microscopic scale are called characteristic times. They are denoted as t_a and t_c in Fig. 1.2. t_a is the avalanche time and it is associated to the breakage of interparticle bonds. On the opposite case, the construction time (t_c) is associated with the microstructure build-up. When the rates of breakage and formation of interparticle bonds are balanced, a steady-state or equilibrium condition is achieved. As a result, macroscopic rheological properties, like local viscosity, also have steady-state values at this condition. Otherwise, these properties are time-dependent.

The opposite behavior to thixotropy is anti-thixotropy or rheopexy (in some literature). The viscosity of the fluids that belongs to this class increases as the liquid is under shaking or shearing.

Both thixotropic and anti-thixotropic behaviors are reversible by definition [5, 19], although irreversible microstructure changes are also present in everyday life. Some examples of irreversible microstructure changes are associated to chemical reactions, like reacting polymers or in drying cement [5]. Nevertheless, these kind of applications are beyond to the scope of this thesis.

Shear stress history also affects the viscosity of time-dependent fluids. The shear stress of a time-independent liquid is unaffected by the direction of change of the shear rate. Figure 1.3 shows the shear stress-shear rate curves of two slurries. The curve of the slurry B (Black line) is the same whether the shear rate has been increased or decreased during the experiment. That is the behavior of a time-independent liquids. For slurry A (red line), the shear stress measured as the shear rate has been raised is higher than the value obtained as the shear rate has been decreased.

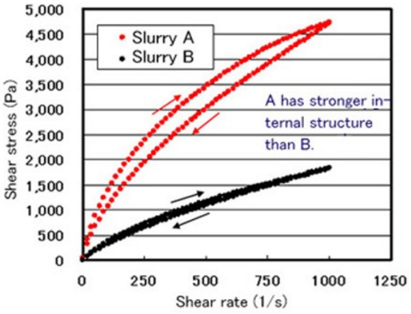

Figure 1.3: Hysteresis loop of a thixotropic slurry of lithium-ion battery (A), retrieved from [4]

The hysteresis loop, shown in Fig. 1.3, is characteristic of a time-dependent liquid. Generally speaking, the larger the enclosed area, stronger is the time-dependent behavior of the material [1]. Likewise, structural hysteresis is an inherent property of time-dependent liquids. The features of a hysteresis loop also depend on duration of the shearing, the rate of increasing/decreasing of shear rate and the past shear history of the sample [1].

It is possible to obtain a flow curve (steady-state viscosity curve) for a particular thixotropic liquid, but it is necessary to allow it enough time to accommodate itself to new flow conditions. For example, considering the red mud suspension presented in Fig. 1.1b, there is an unique viscosity curve if the viscosity at each shear rate is obtained after 2000 s (i.e. the viscosity values become time-independent). So, in this case, the viscosity is solely a function of the shear rate from this time and onward. On the other hand, there could be different viscosity curves for times lower than about 2000s and hysteresis loops are registered for this time range. Considering an equilibrium expression for viscosity in a complex flow, at which liquid particles are subjected to shear stress changes as they flow through different regions at time scales lower than the time required to achieve an equilibrium value of viscosity, may lead to significant errors in the flow description.

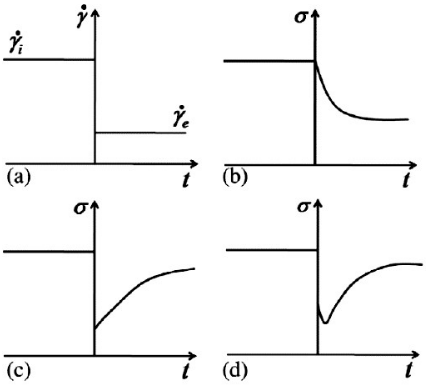

Figure 1.4: Various types of response to a sudden reduction in shear rate (a): b) viscoelastic; c) inelastic thixotropic; d) most general [5]

During the last decades, rheologists have striven to distinguish thixotropic from viscoelastic behavior. In both cases, the stress evolution after a step change in shear rate varies with time until reaching steady state. The key experiment to distinguish both kind of fluids is a step down of shear rate [5], as shown in Fig. 1.4. Viscoelastic fluids present a sustained decrease of the stress (Figure 1.4b) . On the other hand, thixotropic fluids show an instantaneous drop of the stress and an overall recovery of it after some time. Inelastic thixotropic materials show a gradual increase of the stress, just after of the sudden drop (Figure 1.4c). However, in the most general case, they have a fast relaxation time and they finally experience a gradual and slow increase of their stress, and viscosity, until achieving a stable value (Figure 1.4d).

Most thixotropic materials present time-dependent features in combination with plastic and viscoelastic responses. Materials that present this behavior are classified as thixotropic-elasto-visco-plastic (TEVP) materials [9, 18, 19, 22]. Elasticity is not present in ideal thixotropic materials. They are classified as thixotropic-visco-plastic (TVP) materials. An example of liquid that presents this response is laponite suspension. Among TVP materials, there are few examples that present very low or null values of yield stress. The last group is referred to thixotropic-viscous (TV) materials.

After considering thixotropic characterization, it is necessary to discuss thixotropic modeling. This topic is addressed in chapter 2 in more detail. Most models are based on empirical parameters and phenomenological equations. In addition, most models are restricted to ideal thixotropic materials. The works by Souza Mendes and Thompson [9, 23, 24] presented two models applicable to both TVP and TEVP materials. One of them is based on the traditional structure parameter (λ) [24], reported by the vast majority of the literature, while the other is based on the concept of fluidity (i.e. reciprocal of viscosity) [9].

1.2
Rheological modeling of particle suspensions

Particle suspensions are characterized by solid particles dispersed in a liquid phase. Despite the Newtonian nature of the solvent, the addition of solid-dispersed phase introduces different non-Newtonian behaviors [25]. In many cases, the addition of particles in a certain solvent is done to fulfill a particular application.

Despite the nature of the solvent, there are many factors that influence the rheological properties of a suspension, as for instance, the size of the particles. For example, colloidal systems (i.e. particle size smaller than 1 μm [26]), like clay suspensions, usually exhibit thixotropic characteristics [27]. Furthermore, thixotropy has also been found in macroscopic or non-Brownian suspensions, at which particle arrangements are also responsible for the increased liquid viscosity [28]. Other variables that affect suspension rheological properties are particle volume fraction (φ), inter-particle interaction forces, particle shape, spacial arrangement of the particle, and size- and shape- distribution of the particles [25]. Non-spherical particles strengthen the thixotropic nature of particle suspensions since they may form 3D arrangements in lower volume fraction than that for spherical particles [2].

In spite of the complex nature of particle suspensions, they are usually modeled by equations that do not consider the time-dependency originated by the evolution of the particle structure. In fact, these equations describe the liquid viscosity as a function of the deformation rate only. Non-Newtonian models like Bingham, Power-Law, Carreau, shown in table 1.1, are usually employed to describe how the viscosity varies with shear rate.

The simplest model for shear-thinning fluids is the Power-law or Ostwald-de-Walde equation. This model has important shortcomings, like the inability of predicting the low and high shear plateaus η_0 and η_∞. Therefore, it is just adequate in a very restricted operability range far from viscosity plateaus. Despite this and other disadvantages, the Power-law model is the most widely used in the literature dealing with industrial engineering applications [1]. On the other hand, Carreau-Yasuda model is able to predict the viscosity plateaus and it is used when a better description of the flow is necessary.

A drawback of the Carreau-Yasuda model is its inability to model visco-plastic fluids (i.e. materials which needs an initial stress to start flowing). Table 1.1 presents models that are used to describe visco-plastic liquids. Bingham and Herschel-Buckley (HB) are widely used to model this class of fluids. The latter is largely used to describe viscoplastic liquids that show shear-thinning behavior. However, it is unable to predict viscosity plateaus. Lin et al. [15] proposed a model which considers η_0 and η_∞ in the description of viscoplastic liquids. Furthermore, Souza Mendes et al. [9] also proposed a steady-state model for a laponite suspension with similar features as part of their thixotropic model. The last model is discussed in detail in section 2.2.2.

As mentioned before, the rheological response of particles suspensions strongly depends on the particle concentration. In fact, works, like Lin et al. [15], have demonstrated the effect of the solid-phase concentration on rheological parameters such as yield stress, consistency and flow indexes [25, 15]. Table 1.2 presents common models to describe how the viscosity changes with particle concentration. As the concentration increases, the complexity of the required equation increases as well. For example, Einstein's model is only valid for very diluted suspensions. Furthermore, particle interactions, shape and distribution of particles, and other factors might restrict the applicability range of a particular model.

Table 1.2: Selected rheological models based on particle concentration at steady state condition

Name	Viscosity equation
Rigid spherical particles	
Einstein [29]	$\frac{\eta}{\eta_{solv}} = 1 + B\varphi$
Krieger-Dougherty [30]	$\frac{\eta}{\eta_{solv}} = \left(1 - \frac{\varphi}{\varphi_m}\right)^{-[\eta]\varphi_m}$
Non-spherical particles	
Santamarıa-Holek & Mendoza [31]	$\frac{\eta}{\eta_{solv}} = \left[1 - \left(\frac{\varphi}{1-c_m\varphi}\right)\right]^{-[\eta]}$

B: Einstein's coefficient, φ_m: filling fraction at maximum packing, $c_m = 1 - \varphi_c/\varphi_c$ where φ_c is the crowding factor, $[\eta]$: intrisic viscosity.

Precise flow models of particle suspensions should consider that particle concentration φ is not uniform throughout the domain. Shear-induced particle migration models, like that by Phillips et al. [32], are used to evaluate local particle concentration in a flow.

The use of a time-independent model to describe flow of particle suspensions and other complex liquids may lead to strong inaccuracies. In these models, the local viscosity is just a function of the local shear rate, and in some cases also a function of the local particle concentration. As discussed before, it takes some time for the viscosity to reach a steady-state value after a step change in shear rate. TIM are not able to describe this behavior. It can be very important if the flow characteristic time is in the same order of the avalanche or construction time of the liquid.

Grillet et al. [6] compared measured viscosity values of a suspension, of polydisperse alumina in polyether triamine, and values obtained from the Carreau-Yasuda model during step changes of shear rate. As expected, the model could not capture the transient response of the suspension under changes in the equilibrium conditions. However, as the steady-state condition is achieved, the time-independent model has an excellent agreement with the experimental data, as shown in Fig. 1.5. The data about shear rate history and other parameters are presented in table 1.3. The viscosity rate constant (κ) is obtained from exponential fitting of the experimental data and it is inversely proportional to the liquid characteristic time (i.e. t_a or t_c). In the case of an increase of shear rate, κ is inversely proportional to the avalanche time. Otherwise, $\kappa \propto 1/t_c$.

Table 1.3: Shear history data from Fig.1.5 [6]

Time (s)	Shear rate (s^{-1})	Steady-state viscosity at 70ºC (Pa.s)	Rate constant (s^{-1})
Pre-shearing (t<0)	2.00	-	-
0 - 1999.7	0.02	58.2	0.002
2000 - 2199	0.20	11.3	0.068
2200 - 2399.7	2.00	4.2	0.102
2401.2 - 3398.7	0.20	11.2	0.010

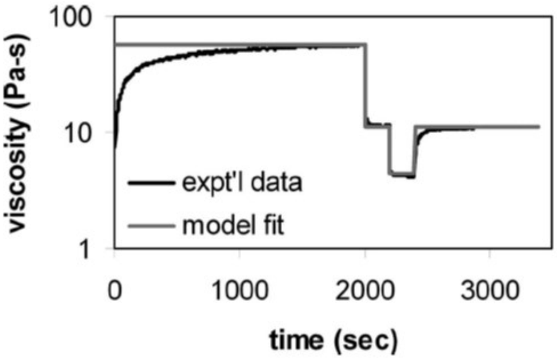

Figure 1.5: Viscosity of an alumina suspension at 70ºC (expt'l data) vs Carreau-Yasuda (model fit) [6]

Analyzing figure 1.5 and table 1.3, it is possible to affirm that the major errors in modeling thixotropic flows by TIM are related to large characteristic times. For example, t_c is about 2000 s in the first segment while t_a is lower than about 15 s in the second and third segments respectively. Then, it is possible to explain the very poor fitting by Carreau-Yasuda model during the first build-up step while it has a much better performance in the microstructure breaking stages.

According to the results shown above, it might be possible to affirm that it is adequate to employ TIM in case of short thixotropic characteristic times. However, it might be very arbitrary to determine when the time is short or large. As a result, it should be useful to establish a time of reference. In a Lagrangian frame of reference (i.e. frame of reference that moves with the material particle), a residence time might be a good choice. Actually, the ratio between the liquid characteristic time and the flow residence time is defined as thixotropy number [33]. The latter parameter defines the importance of thixotropy impact in complex flows.

1.3
Small scale flows explored

In the present work, we have been particularly interested in small scale flows, which generally present very short residence times and consequently large thixotropic numbers.

First, the flow of thixotropic liquid through a constricted microcapillary is analyzed. Despite its simplicity, the flow kinematics show regions of fully-developed flow, regions of structure breakdown near the constriction , and regions of buildup near the expansion. In order to evaluate the importance of thixotropy in the flow, the flow predictions of a TIM and thixotropic model are compared at different flow conditions. A sketch of a constricted capillary is shown in Fig 1.6.

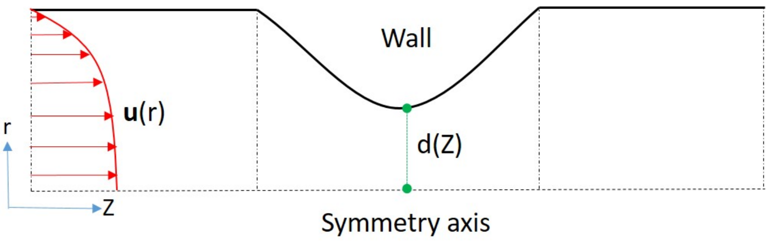

Figure 1.6: Sketch of half micro-channel with a constriction

The second application considered is the flow that occurs in slot coating process. Coating is an industrial process where one or more liquid layers are deposited on a surface; then they are dried or cured to form solid films to serve a particular purpose [34]. This technique is used in the manufacturing of many products, including battery production. A sketch of this flow is shown in Fig. 1.7. The suspension is pumped and delivered into a coating die. Then, the coating liquid is applied onto a solid surface (substrate) through a narrow slot. As a result, the suspension fills the gap between the adjacent die lip and the substrate. The area covered by the suspension in the gap, bounded by the upstream and downstream gas-liquid interfaces, is called *coating bead.*

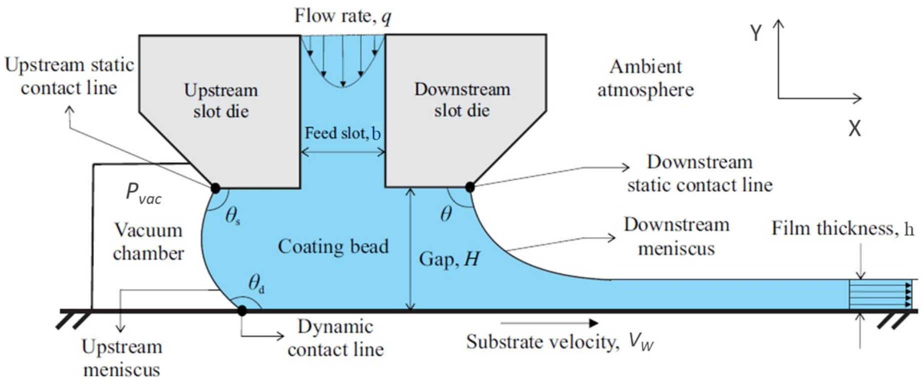

Figure 1.7: Sketch of the slot coating process (Adapted from [7])

To maintain a stable coating bead and/or produce a thin deposited film without defects, the upstream gas pressure is usually below ambient pressure (P_{vac} shown in Fig. 1.7) by employing a vacuum chamber (Beguin (1954) as cited by Rebouças et al.[35]). However, in some specific processes where thick film is produced, vacuum pressure is not necessary [36].

Slot coating belongs to a class of coating methods known as *pre-metered coating.* The thickness of the coated liquid layer (h) is set by the flow rate (q) fed into the die and the speed of the moving substrate (V_w), i.e. $h = q/V_w$. Therefore, it is independent of other process variables [37]. Thus pre-metered methods are ideal for high precision coating. However, the uniformity of the deposited layer and therefore the quality of the product depend on other parameters, such as liquid viscosity and its rheology, vacuum pressure applied, superficial tension, coating gap, slot die configuration, etc [38]. As a result, there are limits in operating conditions of slot coating. Working beyond these limits leads to a coating product with defects.

The most common defects related to the operating limits of slot coating are: air entrainment, dripping and rivulets [38]. One of these operating limits defines the minimum coated film thickness achievable (h_{min}), which is also called *low flow limit.* Beyond this limit, the downstream free surface penetrates into the coating bead. This phenomenon occurs since this air-liquid interface is very curved, so it becomes unstable. As a result, it is registered a periodic variation in the transverse section in the film thickness deposited onto the solid surface. Eventually, the non-uniformity leads to alternating stripes of coated and uncoated layers, called *rivulets* [38, 39]. The other two operating limits are defined by the vacuum pressure applied. If P_{vac} is too low, for a given film thickness (h) , the downstream meniscus invades the coating bead and rivulets could be formed in the coated layer. In the case of a too high P_{vac}, the upstream meniscus invades the vacuum chamber. This phenomenon is called dripping, at which the pre-metered characteristic of slot coating is lost.

The region bounded by the operating limits mentioned above, at which a coating product is delivered with acceptable quality, is defined as *coating window*. Figure 1.8 offers a sketch of typical coating window for Newtonian fluids. Defining the limits of these windows is a difficult task, even for Newtonian fluids. Nevertheless, there is extensive literature about coating windows for Newtonian liquids. For instance, Higgings and Scriven [40] analytically defined the vacuum pressure and film thickness operating ranges, extending the work of Ruschak [41]. The work by Higgings and Scriven [40] presents the visco-capillary model used as a reference for coating of Newtonian liquids. Furthermore, Carvalho and Kheshgi [37] presented a more extensive analysis about the *low flow limit*; including theory, numerical and experimental work. According to the latter paper, h_{min} could be much lower than that predicted by the visco-capillary model at high capillary numbers.

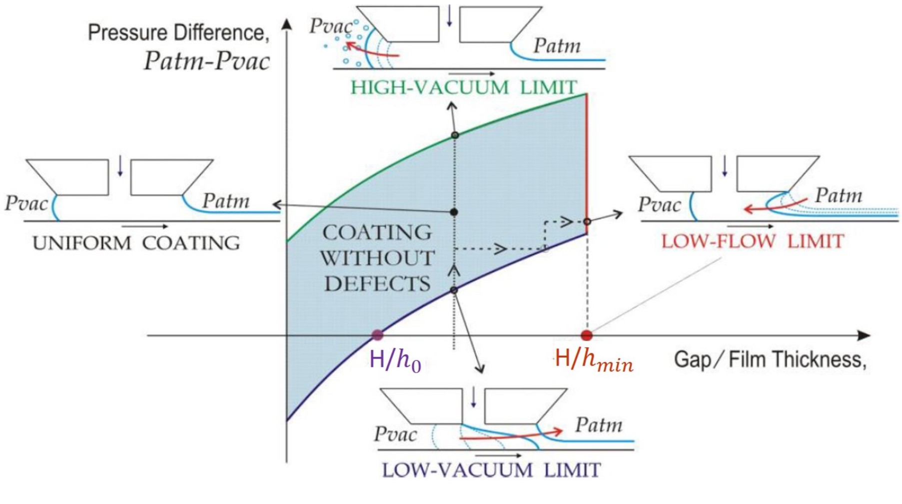

Figure 1.8: Sketch of a typical coating window for Newtonian fluids (Adapted from [8])

Yoon et al. [36] discuss the use of slot coating without applying vacuum. Without vacuum pressure, slot coating is only able to provide thick coating films, which are usually in the order of half of the coating gap. However, there is demand of this kind of products for thick coated films, as for instance, battery electrodes and membrane coatings. The model by Yoon et al. [36] is restricted to Newtonian fluids, although they argue that the same principles might be applied to non-Newtonian fluids. However, battery slurries are usually strongly non-Newtonian fluids with time-dependent behavior, which are not taken into account in the available literature.

In the case of non-Newtonian coating, the literature is much more restricted. However, there are various works where the rheology of the coating liquid is considered. Many of this works have incorporated generalized Newtonian equations into the visco-capillary method. For instance, Tsuda [42] uses the Power-law model and the pressure field equation proposed by Higgings and Scriven [40]. The results show variations on the operability parameters compared to the Newtonian models. Koh et al.[43] and Creel et al. [44] incorporated a more complex model, e.g. Carreau, to obtain the coating window for complex fluids.

Lee et al.[45] incorporated viscoelastic liquids in their analysis by using the Oldroyd-B equation (for a constant shear viscosity). They compared the solutions for Newtonian liquids. Siqueira and Carvalho [7] determined the operability limits for non-colloidal particle suspensions. The inclusion of time-dependence response adds much more complexity and computing costs in modeling a complex thixotropic flow. On the other hand, modeling complex flows of thixotropic materials using models that neglect time-dependent effects may lead to inaccurate predictions [33, 46]. In the particular case of slot coating of particle suspensions, the inaccurate prediction of the process limits may lead to the prediction of process conditions that will yield products with defects.

1.4
Objectives

The main goal of this work is to analyze small scale flows of thixotropic liquids and determine the range of parameters at which neglecting the time-dependent effect leads to inaccurate results.

Predictions were obtained using two rheological models: a thixotropic model, where time-dependency is considered, and a time-independent model. It was considered two small scale steady state flows of a non-Newtonian suspension, which exhibits shear-thinning and thixotropy.

In small scale flows, the residence times are usually very short and typically much lower than the characteristic times of thixotropic liquids.

1.5
Outline

This thesis is divided in six chapters.

In this chapter, Chapter 1, a brief introduction to the problem is presented.

Chapter 2 is a literature review about the different thixotropic models that have been discussed in the literature and it is presented the model used in this work

Chapter 3 provides a description of the numerical method used to solve the resulting differential equations.

The results of the flow though a constricted microcapillary is presented in Chapter 4.

Chapter 5 provides the results of slot coating flow modeling.

Finally, conclusions and future steps are presented in Chapter 6.

2
Thixotropy Modeling

Thixotropy modeling is a difficult task. There are many complex phenomena involved, which are difficult to put all together in a single model. Barnes [2] argues that an ideal model should consider the physics behind thixotropy at microscopic level, and consider for example: size and orientation angle of particles, and density of the entanglements. The simplest models predict that these parameters change instantaneously. However, the author explains that the rheology-determining physical entity (i.e. microstructure) takes time to change when the flow field around it has changed or is changing. Therefore, it would be possible to predict the overall flow behavior if it is known how microstructure change with stress.

Some authors have tried to consider the microstructure nature of thixotropic materials as well its evolution in the rheological model. These models are called microstructural models [2, 18]. Fractal theory, population balance and other considerations have also been employed. However, these models are still under development and their applicability is restricted. In fact, most population balance models (PBM) focus mainly on the dynamics of aggregate size distribution instead of rheological properties, although there is a growing interest in constructing thixotropic constitutive models from them [18].

On the other hand, most research has been focused on studying the impact of the microstructure changes on the bulk rheology. An example of this class of models is structural kinetics models (SKM), which will be described in the next section. These models have been the mostly used in research and industry so far. However, they are restricted to thixotropic visco-plastic liquids. Souza Mendes and Thompson [10, 24, 9] incorporated thixotropic liquids with visco-elastic features in their models by employing mechanical analogues as described in section 2.2. Other class of models uses a rational continuum mechanics approach, where memory functions have been used [47, 48, 49]. Nonetheless, their applicability has been very restricted so far [5].

2.1
Structural kinetics models (SKM) for inelastic thixotropic materials

Most models used to describe thixotropic liquids use a kinetic approach to represent rupture and formation of bonds in the microstructure. A scalar and empirical structure parameter λ is used to associate the degree of material structuring to its bulk rheology. Despite the empirical nature of these models, they have been relatively successful to describe inelastic thixotropic liquids. The models, under this category, follow two general equations. The first relates the stress to the deformation rate and structure level, while the second defines the rate of structuring change [5, 50]:

$$\sigma(t) = f_1[\lambda(t), \dot{\gamma}(t)] \ , \tag{2-1}$$

$$\frac{d\lambda}{dt} = f_2[\lambda(t), \dot{\gamma}(t)] \ . \tag{2-2}$$

For visco-plastic materials, Eq.2-1 is written as:

$$\sigma(t) = \sigma_y[\lambda(t)] + \eta_\lambda[\lambda(t), \dot{\gamma}(t)]\dot{\gamma}(t) + \eta_{\lambda=0}[\dot{\gamma}(t)]\dot{\gamma}(t) \ , \tag{2-3}$$

the first term on the right-hand side of Eq. (2-3) represents the yield stress, while η_λ and $\eta_{\lambda=0}$ are the structural and residual viscosities respectively. The latter is related to the viscosity for a fully unstructure material. It is usually assumed as a constant value (i.e. Newtonian behavior) or a Power law function of the shear rate. Different expressions of the terms $\sigma_y[\lambda(t)]$ and $\eta_\lambda(\lambda(t), \dot{\gamma(t)})$ are presented in table 2.1.

Table 2.1: Some relations between rheological parameters and the structure parameter λ [5]

Author(s)	$\sigma_y(\lambda)$	$\eta_\lambda(\lambda, \dot{\gamma})$
Moore (1959)	-	$\lambda\eta_0$
Worrall & Tuliani (1964)	$\sigma_{y,0}$	$\lambda\eta_0$
Tiu & Boger (1974)	$\lambda\sigma_{y,0}$	$\lambda K_0\dot{\gamma}^{n-1}$
Houska (1980)	$\lambda(\sigma_{y,0} - \sigma_{y,\infty}) + \sigma_{y,\infty}$	$\lambda K_0\dot{\gamma}^{n-1}$
Nguyen & Boger (1985)	$\lambda\sigma_{y,0}$	-
Toorman (1997)	$\lambda\sigma_{y,0}$	$\lambda\eta_0$
Coussot et al. (2002)	-	$\lambda^a\eta_\infty$

Regarding the evolution equation of λ, it is given by Eq. 2-4. Expressions for the breaking up and build-up components have been proposed in the literature and are shown in table 2.2.

$$\frac{d\lambda}{dt} = -k_1\dot{\gamma}^a\lambda^b + [k_2(1-\lambda)^c + k_3\dot{\gamma}^f\sigma^d(1-\lambda)^e] \tag{2-4}$$

Table 2.2: Expressions for the kinetic equations [5]

Author(s)	Breakdown	Build-up	
		(Brownian)	(Shear)
Worrall & Tuliani (1964)	$k_1\lambda\dot{\gamma}$	-	$k_3\dot{\gamma}(1-\lambda)$
Houska (1980)	$k_1\lambda^a\dot{\gamma}$	$k_2(1-\lambda)$	-
Coussot et al. (2002)	$k_1\lambda\dot{\gamma}$	k_2	-
Pinder (1964)	$k_1\lambda^2$	k_2	-
Lee & Brodkey (1971)	$k_1\sigma\lambda^b$	$k_2(1-\lambda)^c$	$k_3\sigma^d(1-\lambda)^e$
Yziquel et al. (1999)	$k_1\lambda\sigma\dot{\gamma}$	$k_2(1-\lambda)$	-
Burgos (2001)	$k_1\dot{\gamma}e^{a\dot{\gamma}}\lambda$	$k_2(1-\lambda)$	-

According to table 2.1, the terms from Eq. 2-1 are usually fitted in different ways depending on the measured rheological response. Some works like Souza Mendes [10, 19] and Souza Mendes and Thompson [23, 24] have tried to unify thixotropic rheological equations in a constitutive model that is able to describe the mechanical behavior of both inelastic and TEVP materials. In fact, the models presented in this section are unable to describe viscoelastic behavior in thixotropic liquids.

Regarding the evolution equation of λ, the terms of the equation are also fitted using one of the models that have been proposed in the literature (as shown in table 2.2).

2.2
Models based on mechanical analogues

In order to incorporate viscoelastic behavior in thixotropic models and solve other issues presented in SKM, models based on mechanical analogues have been proposed, such as those by Souza Mendes [19] and Souza Mendes and Thompson [24]. The proposed models are based on Jeffreys mechanical analogue, sketched in Fig. 2.1a. The inelastic version of the model is sketched in Fig. 2.1b.

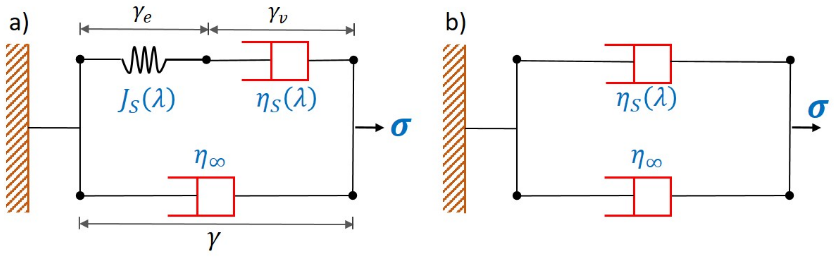

Figure 2.1: a) Representation of a TEVP liquid respond, and, b) representation of a inelastic liquid respond by Jeffreys analogues

In the analogue presented in Fig. 2.1a, J_S represents the elastic component of the material and it is called the shear modulus of the microstructure,

η_S is the structural viscosity, and η_∞ is the viscosity for the fully unstructured liquid. The total strain γ can be split into the elastic γ_e and viscous γ_v strains.

Based on the mechanical analogue presented in Fig. 2.1a, Souza Mendes [19] proposed the model presented in Eq. (2-5). This equation resembles the Oldroyd-B equation for viscoelastic fluids.

$$\dot{\gamma} + \Psi_2 \ddot{\gamma} = \frac{1}{\eta_v}(\sigma + \Psi_1 \dot{\sigma}) \ , \tag{2-5}$$

where, $\Psi_1 = \eta_S / J_S$, $\Psi_2 = \frac{\eta_\infty}{\eta_v}\Psi_1$, and $\eta_v \equiv \eta_S + \eta_\infty$. Ψ_1 and Ψ_2 are the relaxation and retardation times respectively.

Equation (2-5) can be generalized for 3D flows. Therefore, the shear stress intensity, defined as $\sigma \equiv \sqrt{(1/2) tr \boldsymbol{\sigma}^2}$ (tr is the tensor's trace) , is replaced by the tensor $\boldsymbol{\sigma}$ in Eq. (2-5). The shear rate ($\dot{\gamma}$) is replaced by the tensor $\dot{\boldsymbol{\gamma}}$ (i.e. $\dot{\boldsymbol{\gamma}} = (\nabla \cdot v) + (\nabla \cdot v)^T$). Furthermore, time derivatives are substituted by upper convective derivatives:

$$\dot{\boldsymbol{\gamma}} + \Psi_2 \overset{\triangledown}{\dot{\boldsymbol{\gamma}}} = \frac{1}{\eta_v}\left(\boldsymbol{\sigma} + \Psi_1 \overset{\triangledown}{\boldsymbol{\sigma}}\right) \ , \tag{2-6}$$

$$\text{where,} \quad \overset{\triangledown}{M} = \frac{DM}{Dt} - M \cdot (\nabla \boldsymbol{v}) - (\nabla \boldsymbol{v})^T \cdot M \ , \tag{2-7}$$

$\overset{\triangledown}{M}$ is an generic upper convective derivative, defined in Eq. (2-7). The term $\frac{DM}{Dt}$ is the total derivative defined as $\frac{DM}{Dt} \equiv \frac{\partial M}{\partial t} + \boldsymbol{v} \cdot \nabla M$.

Equation (2-6) can be reduced to a viscous fluid, as shown in Eq. (2-8), which may represent the behavior of inelastic thixotropic materials. Ψ_1 and Ψ_2 are equal to zero for this kind of thixotropic fluids regardless their time-dependent nature.

$$\dot{\boldsymbol{\gamma}} = \frac{1}{\eta_v}\boldsymbol{\sigma} \tag{2-8}$$

2.2.1
Structure parameter approach

According to this approach, the material time dependency is associated to the variation of the structure parameter λ with time. This approach has the same principles of the SKMs for the λ's evolution equation. Since this parameter is just an auxiliary variable, the viscosity of the thixotropic material is given as a function of λ and viscosity of reference. For example, Souza Mendes [10, 19] considers the following expression:

$$\eta_v(\lambda) = \left(\frac{\eta_0}{\eta_\infty}\right)^{\lambda} \eta_\infty \ , \tag{2-9}$$

where, η_0 is the viscosity at steady-state condition when the liquid is fully structured, while η_∞ corresponds to the viscosity for the fully unstructured thixotropic liquid . In addition, equation (2-9) is used to estimate the structure parameter at equilibrium condition (λ_{SS}):

$$\lambda_{SS}(\dot{\gamma}) = \left[\frac{ln(\eta_{SS}(\dot{\gamma})) - ln(\eta_\infty)}{ln(\eta_0) - ln(\eta_\infty)}\right] \tag{2-10}$$

There are several rheological time-independent models, which can be used to obtained the expression $\eta_{SS}(\dot{\gamma})$, like Herschel-Buckley (HB) model. Souza Mendes and Dutra [51] proposed a modification of the HB model, Eq. 2-11, where the infinite viscosity prediction (when $\sigma < \sigma_y$) is substituted by a low shear-rate viscosity plateau (η_0), followed an abrupt viscosity drop at the yield stress value.

$$\sigma = \left[1 - exp\left(\frac{-\eta_0\dot{\gamma}}{\sigma_y}\right)\right](\sigma_y + K\dot{\gamma}^n) \tag{2-11}$$

Souza Mendes [10] proposed an evolution equation, Eq. 2-12, with similar features to that employed for SKMs. However, this equation is applicable to 3D flows. Furthermore, the breakdown term $f(\sigma)$ depends on shear stress instead of shear rate, as shown in Eq. 2-13. Likewise, this parameter is equal to zero when $\sigma = 0$ and increases monotonically as stress increases. Actually, Souza Mendes [10] argues that it is more adequate to consider shear stress and not shear rate, since the former is responsible for the inter-particle bonds rupture.

$$\frac{D\lambda}{Dt} = \frac{\partial\lambda}{\partial t} + \boldsymbol{v}\cdot\nabla\lambda = \frac{1}{t_{eq}}\left[(1-\lambda)^a - f(\sigma)\lambda^b\right] \ , \tag{2-12}$$

where, t_{eq} is the characteristic time associated to the λ change, while a and b are positive dimensionless constants. In case of equilibrium condition is achieved, i.e. $\frac{D\lambda}{Dt} = 0$, the function $f(\sigma)$ would be correlated to the liquid structure parameter λ_{SS} at steady-state condition. Then, the $f(\sigma)$ could be expressed as:

$$f(\sigma) = \frac{[1-\lambda_{SS}(\dot{\gamma})]^a}{(\lambda_{SS}(\dot{\gamma}))^b}\left(\frac{\sigma}{\eta_v(\lambda)\dot{\gamma}}\right)^c \tag{2-13}$$

Combining Eq. 2-12 and Eq. 2-13, we have:

$$\frac{D\lambda}{Dt} = \frac{1}{t_{eq}}\left\{(1-\lambda)^a - [1-\lambda_{SS}]^a\left(\frac{\lambda}{\lambda_{SS}}\right)^b\left(\frac{\sigma}{\eta_v(\lambda)\dot{\gamma}}\right)^c\right\} \tag{2-14}$$

2.2.2
Fluidity approach

Souza Mendes et al. [9] proposed an alternative approach to describe the mechanical response of the liquid. The level of structuring of the material is not characterized by the structure parameter λ but rather by fluidity (ϕ_v). The latter parameter is traditionally defined as the reciprocal of the viscosity [52]:

$$\eta_v = \frac{1}{\phi_v} \tag{2-15}$$

The main advantage of this model, when compared to existing phenomenological models for thixotropic materials, is that the evolution equation that describes the microscopic state only involves material functions that are directly measurable by means of standard rheological tests. In addition, the model assumes that there is a one-to-one relation between the local fluidity ϕ_v and the local microscopic state of the liquid.

Due to the advantages listed above, this model was selected as the thixotropic rheological model used in this work. The analyses presented here consider the flow of laponite suspension. The mechanical response of the liquid is described by the analogue sketched in Fig. 2.2 for inelastic thixotropic liquids.

Having in mind that $\eta_v = \eta_s + \eta_\infty$ and the analogue sketched in Fig. 2.2:

$$\frac{1}{\phi_v} = \frac{1}{\phi_s} + \frac{1}{\phi_\infty} \ , \tag{2-16}$$

where, ϕ_∞ is the fluidity of the liquid when it is fully unstructured and ϕ_s is the structural fluidity, which is directly related to the level of structuring of the material. It reaches a minimum value ϕ_{s0} when the material is fully structured. According to the analogue, ϕ_v approaches ϕ_∞ asymptotically as the structuring level becomes low enough that $\phi_s >> \phi_\infty$ and it reaches the minimum value ϕ_0 when the material is fully structured.

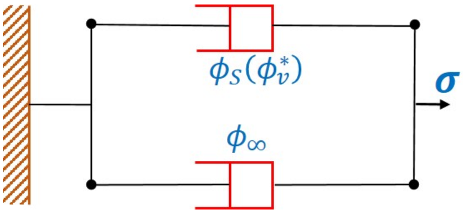

Figure 2.2: Representation of the inelastic liquid respond by a Jeffreys analogue

A dimensionless fluidity, which ranges from 0 to 1, can be defined as:

$$\phi_v^* = \frac{\phi_v - \phi_0}{\phi_\infty - \phi_0} \tag{2-17}$$

$\phi_v^* = 0$ corresponds to the maximum level of structuring, whereas $\phi_v^* = 1$ corresponds to the minimum level of structuring of the liquid. The level of structuring, and therefore the fluidity, changes as the liquid flows through regions of different stress values. The rate of change of the structuring level is a function of the structuring level itself; the more structured is the material, the faster its microstructure tends to break upon the imposition of a higher stress. The rate of change of the material structure is also a function of the local stress. Therefore, the rate of change of the normalized fluidity of the material, which characterizes the level of structuring, is written as:

$$\frac{D\phi_v^*}{Dt} = \frac{\partial\phi_v^*}{\partial t} + \boldsymbol{v}\cdot\nabla\phi_v^* = F(\phi_v^*, \sigma) \ , \tag{2-18}$$

where, σ is the current shear stress intensity, defined as $\sigma \equiv \sqrt{(1/2)tr\boldsymbol{\sigma}^2}$. In a steady state flow from the Lagrangian point of view, $\frac{D\phi_v^*}{Dt} = 0$ and $F(\phi_{eq}^*(\sigma), \phi_v^*) = 0$. Therefore, $\phi_v^* = \phi_{eq}^*(\sigma)$, where $\phi_{eq}^*(\sigma)$ is the equilibrium fluidity evaluated at the current stress state σ. It is obtained directly from the flow curve of the liquid. Since ϕ_{eq}^* is a function of the stress only, eq. 2-18 can be written as:

$$\frac{D\phi_v^*}{Dt} = \frac{\partial\phi_v^*}{\partial t} + \boldsymbol{v}\cdot\nabla\phi_v^* = F(\phi_v^*, \phi_{eq}^*(\sigma)) \tag{2-19}$$

The function $F(\phi_v^*, \phi_{eq}^*(\sigma))$ can be obtained by imposing step changes in the stress and measuring the transient evolution of the shear rate [9]. The structure construction and destruction dynamics can be analyzed by imposing downward and upward step changes.

Souza Mendes et al. [9] used a 2 wt% suspension of Laponite RD (Rockwood Additives Ltd.) in water with 0.4 mol/L NaCl concentration. The pH was adjusted to 10 with 0.04 mol/L of NaOH. We used this liquid as reference here, the functional form of ϕ_{eq}^* and $F(\phi_v^*, \phi_{eq}^*(\sigma))$ and their respective rheological parameters used in the analyses presented in this thesis correspond to those associated with the laponite suspension.

The rheological parameters presented in the work by Souza Mendes et al. [9] were obtained by fairly standard rheological tests with a AR-G2 TA instruments controlled-stress rheometer. They checked the inelastic behavior of the laponite suspension employed. Then, it was determined the yield stress (σ_y) and the zero-shear-rate fluidity (ϕ_0) were obtained by a creep test. It consists in imposing a shear stress (σ_f) to a sample initially at rest. After gradually increasing σ_f, it was found that $\sigma_y \approx 6$ Pa. Regarding ϕ_0, Souza Mendes et al. [9] assummed that it is about zero since they do not observed a

Newtonian plateau in the low stress range. However, this values is not strictly equal to zero. Actually, Lin et al. [15] worked with laponite and bentonite suspensions and they registered ϕ_0 (i.e. $\eta_0 = 1/\phi_0$) in the range of $10^{-5} - 10^{-3}$ $(\mathrm{Pa.s})^{-1}$.

The equilibrium fluidity ϕ^*_{eq} expression (Eq. 2-20), plotted in Fig. 2.3, is obtained by curve fitting the steady-state shear viscosity measurements. In the case of time-dependent fluids, it is necessary to allow enough time to ensure achieving a real steady-state condition. The data is well fitted by Eq. 2-20. The model parameters come from the curve fitting procedure:: $K = 1\ Pa.s^n$, $n = 0.32$, and $\phi_\infty = 64.1(Pa.s)^{-1}$ (i.e. $\eta_\infty = 1/\phi_\infty$). $H(\sigma - \sigma_y)$ is the Heaviside step function which is equal to 1 when $\sigma > \sigma_y$, otherwise it is equal to zero.

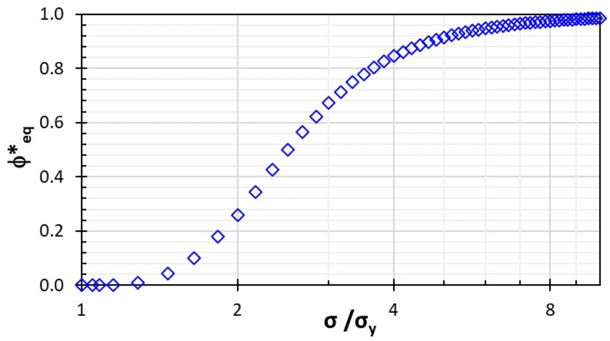

Figure 2.3: Normalized equilibrium fluidity as function of the ratio of shear stress and yield stress, for a laponite suspension with $\sigma_y = 6\ Pa$

$$\phi^*_{eq} = \frac{\frac{1}{\sigma}\left[\frac{|\sigma-\sigma_y|}{K}\right]^{1/n} H(\sigma - \sigma_y)}{(\phi_\infty - \phi_0) + \frac{1}{\sigma}\left[\frac{|\sigma-\sigma_y|}{K}\right]^{1/n}} \tag{2-20}$$

To obtain the functional form of $F(\phi^*_v, \phi^*_{eq}(\sigma))$, it is necessary to perform two kind of experiments: microstructure construction and destruction experiments. In the first experiment, the liquid is allowed to achieved an equilibrium condition by at a fixed shear stress σ_i. Suddenly, the stress is decreased to σ_f. Then, the transient respond of the shear rate $(\dot\gamma)$ is registered until achieving a new equilibrium condition, the latter is referred as $\phi^*_{eq}(\sigma_f)$ or just ϕ^*_{eq}. The input and output of the construction experiment are illustrated in Fig. 2.4.

As shown in Fig. 2.4, there is a sudden decrease in the output shear rate at t=0 (when the transient respond is started to be registered). The liquid response is due to the rheological nature of time-dependent fluids. Since the microstructure needs time to accommodate itself to new flow conditions (in this case a change in shear stress), the liquid viscosity does not change immediately and it takes time to achieve the equilibrium value. In the case of $\sigma_f < \sigma_y$, the final fluidity will tend to ϕ_0 and $\phi^*_{eq} = 0$. As a result, the liquid would tend to gel and stop flowing. Otherwise, $\phi^*_{eq} > 0$ and the thixotropic material will

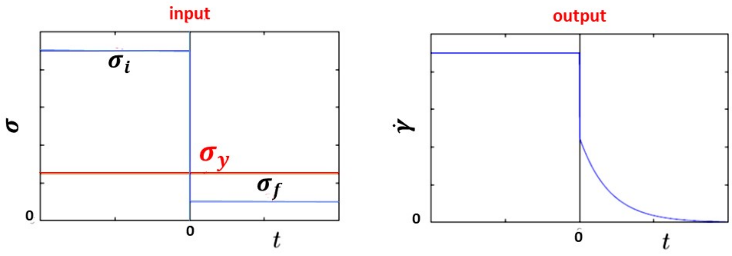

Figure 2.4: Input and output of the microstructure construction experiment, adapted from [9]

remain as a liquid but the level of liquid microstructuring is higher than at the beginning of the experiment, as reflected in Fig. 2.5.

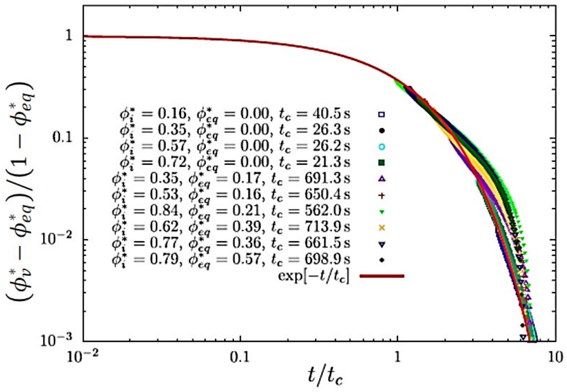

Figure 2.5: Output data and curve fitting of the microstructure construction experiment for a laponite suspension, adapted from [9]

The experimental data plotted in Fig. 2.5 nicely collapse in the same fitting curve, represented by Eq. 2-21. Souza Mendes et al. [9] averaged the construction time, according to the case: if $\phi_{eq}^* > 0$ or $\phi_{eq}^* = 0$. In the first case, the average t_c was 663 s. In the second case, t_c was 29 s.

$$\frac{\phi_v^* - \phi_{eq}^*}{1 - \phi_{eq}^*} = \exp\left(-t/t_c\right) \tag{2-21}$$

Diferentiating Eq. 2-21, it is possible to get an expression for the build-up rate (i.e. $\phi_{eq}^* < \phi_v^* \leq 1$):

$$\frac{D\phi_v^*}{Dt} = -\frac{(\phi_v^* - \phi_{eq}^*)}{t_c}, \quad \phi_{eq}^* < \phi_v^* \leq 1 \tag{2-22}$$

It is clear that the construction time t_c is the time scale for the build-up of the microstructure. It is also a characteristic time of thixotropy , because, as $t_c \to 0$, the rate described by Eq. 2-22 becomes infinite. It means an instantaneous change of ϕ_v^* which implies no-thixotropy. On the other hand, the larger the t_c the more thixotropic the material is [9].

The expression of $F(\phi_v^*, \phi_{eq}^*(\sigma))$, in the range of $0 < \phi_v^* \leq \phi_{eq}^*$, is obtained from the microstructure destruction experiment. The principles are similar to those for the construction experiment. However, in this case, σ_f is always higher than σ_y as shown in Fig. 2.6. In the beginning, the thixotropic material which is not flowing (σ_i<σ_y). Then, it is imposed an increase of stress (i.e. from σ_i to σ_f). Then, the evolution of the shear rate until achieving a steady-steady condition is recorded. The delay time between the application of the test and the onset of observable flow is called as avalanche time, t_a. Since in the beginning, the material is not flowing, $\phi_{eq}^*(\sigma_i) = 0$. The final equilibrium condition achieved is denoted as $\phi_{eq}^*(\sigma_f)$ or just ϕ_{eq}^* in Fig. 2.7.

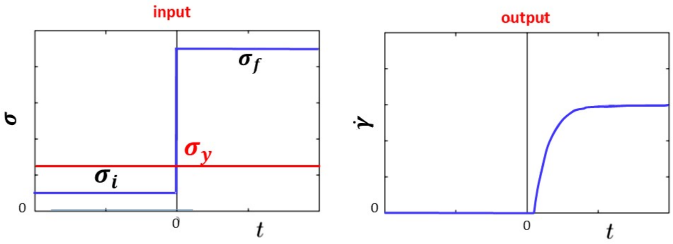

Figure 2.6: Input and output of the microstructure destruction experiment, adapted from [9]

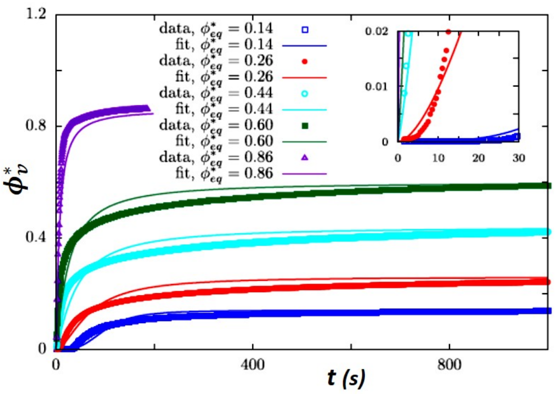

Figure 2.7: Output data and curve fitting of the microstructure destruction experiment for a laponite suspension, adapted from [9]

Fig. 2.7 presents the measured value of the fluidity during the microstructure destruction experiments at different conditions. The data is well fitted by Eq. 2-23. The parameter s is a positive exponent which depends on ϕ_{eq}^*. Likewise, ta also depends on ϕ_{eq}^*, as shown in Fig. 2.8.

$$\phi_v^* = \left(\phi_{eq}^* + \frac{\phi_0}{\phi_\infty - \phi_0}\right)\frac{t^s}{t_a^s + t^s} - \frac{\phi_0}{\phi_\infty - \phi_0} \tag{2-23}$$

The trend of the curves, shown in Fig. 2.8, is physically meaningful. For

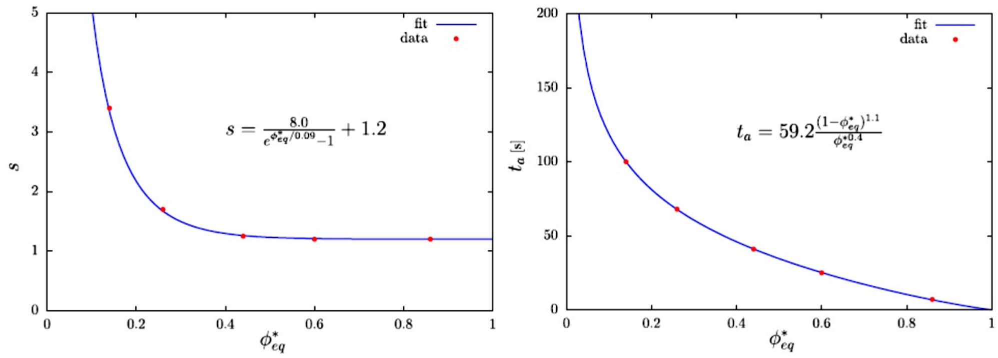

Figure 2.8: a) The exponent s, b) the avalanche time; as a function of the equilibrium fluidity (adapted from [9])

example, as the difference between the applied stress (σ_f) and σ_y increases the values of ta and s decreases. Eventually, if σ_f is large enough, the associated ϕ^*_{eq} would approximately equal to 1 (which represents the maximum achievable level of destruction of the microstructure). Then, in this extreme case, the liquid's respond tends to be instantaneous since $t_a \rightarrow 0$. Regarding the exponent s, it tends to be equal to 1.2 when $\phi^*_{eq} \rightarrow 1$.

Diferentiating Eq. 2-23 and making some arrangements and considerations, like $\phi_\infty >> \phi_0$, it is obtained an expression for the rate of microstructure breakdown, shown as:

$$\frac{D\phi^*_v}{Dt} = \frac{s}{t_a\phi^*_{eq}}\left(\phi^*_{eq} - \phi^*_v\right)^{\frac{s+1}{s}} \phi^{*\,\frac{s-1}{s}}_v, \quad 0 < \phi^*_v \leq \phi^*_{eq} \tag{2-24}$$

To sum up, the rate of buildup and breakdown of the liquid structure, i.e. $F(\phi^*_v, \phi^*_{eq}(\sigma))$, is given by:

$$F(\phi^*_v, \phi^*_{eq}(\sigma)) = \begin{cases} \frac{s}{t_a\phi^*_{eq}(\sigma)}\left(\phi^*_{eq} - \phi^*_v\right)^{\frac{s+1}{s}} \phi^{*\,\frac{s-1}{s}}_v, & 0 < \phi^*_v \leq \phi^*_{eq} \\ \\ -\frac{(\phi^*_v - \phi^*_{eq})}{t_c}, & \phi^*_{eq} < \phi^*_v \leq 1 \end{cases} \tag{2-25}$$

The functional form for $0 < \phi^*_v \leq \phi^*_{eq}$ represents the breakdown dynamics. For the laponite suspension, the avalanche time t_a and the exponent s are a function of the equilibrium fluidity, as shown in Fig. 2.8. By curve fitting, is obtained:

$$t_a = 59.2\frac{(1-\phi^*_{eq})^{1.1}}{\phi^{*\ 0.4}_{eq}} \ , \tag{2-26}$$

$$s = \frac{8.0}{e^{\phi^*_{eq}/0.09}-1} + 1.2 \ . \tag{2-27}$$

The functional form for $\phi^*_{eq} < \phi^*_v \leq 1$ represents the structure buildup dynamics. For the laponite suspension, the construction time (t_c) is 663 s when $\phi^*_{eq} > 0$. It is important to note that the presented funcional form of F represents the behavior of the laponite suspension used as the base liquid in our analysis. Other systems may present different funcitonal forms, but the procedure to describe the transient response remains the same, no matter the liquid system of interest.

3
Computational solution

This chapter summarizes the set of partial differential equations (PDE) used to describe the flow of thixotropic liquids and the numerical approach used to compute approximate solutions.

3.1
Conservation equations

Liquid flow is described by mass and momentum conservation equations:

$$\frac{D\rho}{Dt} + \rho(\nabla \cdot \boldsymbol{v}) = 0, \tag{3-1}$$

$$\rho \frac{D\boldsymbol{v}}{Dt} = \rho \left[\frac{\partial \boldsymbol{v}}{\partial t} + \boldsymbol{v} \cdot \nabla \boldsymbol{v} \right] = \nabla \cdot \boldsymbol{T} + \rho \boldsymbol{b}. \tag{3-2}$$

Making some considerations for the particular cases studied in the present work, Eqs. 3-1 and 3-2 can be simplified. For example, we consider incompressible fluids (i.e. $\frac{D\rho}{Dt} \equiv 0$), steady-state flows (i.e. $\frac{\partial \boldsymbol{v}}{\partial t} = 0$), and negligible body forces (i.e. $\boldsymbol{b} \approx 0$). The simplified mass and momentum equations become:

$$\nabla \cdot \boldsymbol{v} = 0, \tag{3-3}$$

$$\rho \boldsymbol{v} \cdot \nabla \boldsymbol{v} = \nabla \cdot \boldsymbol{T}, \tag{3-4}$$

where $\boldsymbol{v}$ is the velocity vector, ρ is the liquid density, $\boldsymbol{T}$ is the stress tensor. The stress tensor is split as $\boldsymbol{T} = -p\boldsymbol{I} + \boldsymbol{\sigma}$, where p is the pressure field, $\boldsymbol{I}$ is the identity tensor, and $\boldsymbol{\sigma}$ is the extra stress. In the case of inelastic fluids, as explained in the previous chapter, the shear stress tensor ($\boldsymbol{\sigma}$) and the strain-rate tensor ($\dot{\boldsymbol{\gamma}}$) are related by the Newton's law of viscosity, where η_v is the local viscosity of the liquid.

$$\boldsymbol{\sigma} = \eta_v \dot{\boldsymbol{\gamma}} \quad \text{or} \quad \dot{\boldsymbol{\gamma}} = \phi_v \boldsymbol{\sigma}, \tag{3-5}$$

ϕ_v is called fluidity and it is just the reciprocal of viscosity (i.e. $\phi_v = 1/\eta_v$).

Since viscosity or fluidity are scalar values, most generalized Newtonian models relate viscosity to strain-rate intensity as $\eta_v = \eta_v(\dot{\gamma})$. The strain-rate intensity ($\dot{\gamma}$) is usually called *deformation rate*, and it is calculated as a function of the second invariant (II) of the tensor, as follows [53]:

$$\dot{\gamma} = \sqrt{\frac{1}{2} II} = \sqrt{\frac{1}{2} tr \dot{\boldsymbol{\gamma}}^2} = \sqrt{\frac{1}{2} \sum_i \sum_j \dot{\gamma}_{ij} \dot{\gamma}_{ji}} \ , \tag{3-6}$$

where $\dot{\gamma}_{ij}$ is defined as $\dot{\gamma}_{ij} = \partial_i v_j + \partial_j v_i$ in index notation. In 2D Cartesian coordinates, the second invariant is calculated by the expression Eq. 3-7 and the resulting shear rate is given by Eq. 3-8:

$$II = 4\left[\left(\frac{\partial v_x}{\partial x}\right)^2 + \left(\frac{\partial v_y}{\partial y}\right)^2\right] + 2\left(\frac{\partial v_x}{\partial y} + \frac{\partial v_y}{\partial x}\right)^2 , \tag{3-7}$$

$$\dot{\gamma} = \sqrt{\frac{1}{2}\left\{4\left[\left(\frac{\partial v_x}{\partial x}\right)^2 + \left(\frac{\partial v_y}{\partial y}\right)^2\right] + 2\left(\frac{\partial v_x}{\partial y} + \frac{\partial v_y}{\partial x}\right)^2\right\}} \ . \tag{3-8}$$

The stress intensity (σ) is evaluated from the extra stress tensor in the same way.

In complex flows, even in most 2D Newtonian flows, there is no analytical solutions for the governing PDE. As a result, it is necessary to solve the set of coupled differential equations by numerical methods. Most of these methods imply discretizing the domain. In the case of time-independent fluids that can be described by steady-state models, in a domain with fix boundaries, it is only necessary to discretize Eqs 3-3 and 3-4 coupled with chosen viscosity function. In the case of flows of thixotropic liquids, it is necessary to include the evolution equation of the structure parameter or fluidity. In the present work, it was selected the model proposed by Souza Mendes et al.[9], which is based on fluidity. The evolution of this variable is given by Eq. 3-9, where the time-dependency is considered from the Lagrangian frame of reference.

$$\boldsymbol{v} \cdot \nabla \phi_v^* - F(\phi_v^*, \phi_{eq}^*(\sigma)) = 0 \ , \tag{3-9}$$

where, ϕ_v^* is a normalized fluidity, while the functional forms of $\phi_{eq}^*(\sigma)$ and $F(\phi_v^*, \phi_{eq}^*(\sigma))$ are those that correspond to the laponite suspension used by Souza Mendes et al.[9], and are defined as:

$$\phi_v^* = \frac{\phi_v - \phi_0}{\phi_\infty - \phi_0} \ , \tag{3-10}$$

$$\phi^*_{eq}(\sigma) = \frac{\frac{1}{\sigma}\left[\frac{|\sigma-\sigma_y|}{K}\right]^{1/n} H(\sigma-\sigma_y)}{(\phi_\infty - \phi_0) + \frac{1}{\sigma}\left[\frac{|\sigma-\sigma_y|}{K}\right]^{1/n}}, \tag{3-11}$$

where $H(\sigma - \sigma_y)$ is the Heaviside function,

$$F(\phi^*_v, \phi^*_{eq}(\sigma)) = \begin{cases} \frac{s}{t_a \phi^*_{eq}}(\phi^*_{eq} - \phi^*_v)^{\frac{s+1}{s}} \phi^{*\,\frac{s-1}{s}}_v, & 0 < \phi^*_v \leq \phi^*_{eq} \\ \\ -\frac{(\phi^*_v - \phi^*_{eq})}{t_c}, & \phi^*_{eq} < \phi^*_v \leq 1 \end{cases} \tag{3-12}$$

For the time-independent model, it was considered the equilibrium fluidity expression Eq. 3-11.

For the sake of simplicity, the explanation of the numerical and computational methodology starts by the time-independent model in section 3.2.1. Then, time-independent flows with non rigid boundaries (i.e. free surfaces) are incorporated in section 3.2.2. Finally, more complexity is added and thixotropic fluids are incorporated in section 3.2.3.

3.2
Discretizing the system of differential equations by the Finite Element Method

There are different methods used to numerically solve a system of non-linear differential equations. Most of them involve discretization of the domain and the differential equations. As a result, the system of differential equations becomes in a set of algebraic equations. Then, the system of equations is solved by linear algebra methods. Depending on the discretization method and the refining of the domain grid, the numerical solution might be more or less accurate. Higher accuracy usually implies in higher computational costs.

The oldest way of discretization is the finite difference method (FDM). It is usually used with structured grids. The most widely applied method in computational fluid dynamics (CFD) is the finite volume method (FVM). This method is very versatile and can be employed in both structured and non-structured grids. It discretizes directly the integral form of the conservation laws [54]. However, its approximation is typically zeroth order and requires very fine mesh to achieve accurate results.

The finite element method (FEM) is a higher order variational method. It is a generalization of variational (i.e. the Rayleigh (1876) and the Ritz (1908)), and weighted-residual (i.e. the Galerkin (1915), least squares, collocation, etc) methods [55, 56]. The domain is divided into elements. Figure 3.1 presents a mesh used to discretize the flow domain in one example explored here, the flow through a constricted microcapillary. Quadrilateral elements were used in the

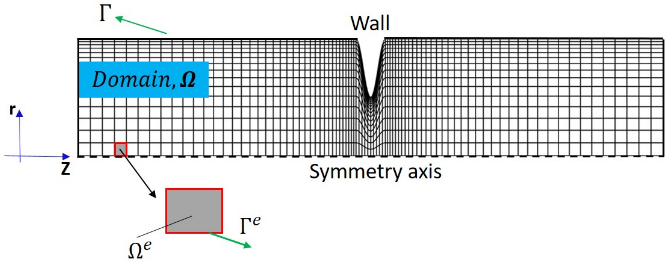

Figure 3.1: Finite discretization of a constricted micro-channel

analyses presented in this thesis.

The finite element method is based on the idea that the solution u of a differential equation can be represented as a linear combination of appropriately selected basis functions ψ_i in the entire domain of the problem [55, 56]:

$$u = \sum_{i=1}^{N} c_i \psi_i \tag{3-13}$$

The coefficients c_i are then determined such that the differential equation is satisfied, often, in a weighted-integral sense [55]. The algebraic system of equations that leads to the solution of the coefficients of the linear expansion is obtained by setting N weighted residual equations to zero. The functions used to compute the weighted residuals are called the weighting functions.

3.2.1
Weighted residual equations for the time-independent model

In this section, the *weak-form* of Eqs. 3-3 and 3-4 is presented. In this way, Newtonian flow dynamics problems are solved by employing the Finite Element Method (FEM). However, this methodology can be applied to time-independent fluids as well considering local instead of global viscosity (or fluidity). Carvalho and Valerio [56] provide a detailed explanation about discretizing the mass and momentum conservation equations which is briefly presented here. The weighted forms of these equations are written as:

$$R_c = \int_{\Omega} [\nabla \cdot \boldsymbol{v}] W_c d\Omega = 0 \ , \tag{3-14}$$

$$R_m = \int_{\Omega} [\rho \boldsymbol{v} \cdot \nabla \boldsymbol{v} - \nabla \cdot \boldsymbol{T}] \cdot \boldsymbol{W_m} d\Omega = 0 \ , \tag{3-15}$$

where, W_c and $\boldsymbol{W_m}$ are weighting functions, which should be carefully selected. W_c is a scalar function, while $\boldsymbol{W_m}$ is a vectorial function. R_c and R_m are the weighted residues for the mass and momentum conservation laws. The domain area is denoted as Ω (as in Fig. 3.1) thus the integral of Eqs. 3-14 and 3-15 are surface integrals.

Splitting up Eq. 3-15:

$$R_m = \int_\Omega \rho(\boldsymbol{v}\cdot\nabla v)\cdot\boldsymbol{W_m}d\Omega - \int_\Omega(\nabla\cdot\boldsymbol{T})\cdot\boldsymbol{W_m}d\Omega = 0 \tag{3-16}$$

Eq. 3-16 can be expressed in a more convenient way, by using the identity $\boldsymbol{T}:\nabla\boldsymbol{W} = \nabla\cdot(\boldsymbol{T}\cdot\boldsymbol{W}) - (\nabla\cdot\boldsymbol{T})\cdot\boldsymbol{W}$, and the Gauss-Green-Ostrogradskii theorem as:

$$R_m = \int_\Omega \rho(\boldsymbol{v}\cdot\nabla\boldsymbol{v})\cdot\boldsymbol{W_m}d\Omega + \int_\Omega \boldsymbol{T}:\nabla\boldsymbol{W_m}d\Omega - \oint_\Gamma(\hat{\boldsymbol{n}}\cdot\boldsymbol{T})\cdot\boldsymbol{W_m}d\Omega = 0 \tag{3-17}$$

Considering a 2D flow in Cartesian coordinates, the terms of Eq. 3-17 can be expressed as:

$$(\boldsymbol{v}\cdot\nabla\boldsymbol{v})\cdot\boldsymbol{W_m} = W_1\left(u\frac{\partial u}{\partial x} + v\frac{\partial u}{\partial y}\right) + W_2\left(u\frac{\partial v}{\partial x} + v\frac{\partial v}{\partial y}\right)\ , \tag{3-18}$$

$$\boldsymbol{T}:\nabla\boldsymbol{W_m} = \frac{\partial W_1}{\partial x}T_{xx} + \frac{\partial W_1}{\partial y}T_{xy} + \frac{\partial W_2}{\partial x}T_{yx} + \frac{\partial W_2}{\partial y}T_{yy}\ , \tag{3-19}$$

$$(\hat{\boldsymbol{n}}\cdot\boldsymbol{T})\cdot\boldsymbol{W_m} = f_x W_1 + f_y W_2\ , \tag{3-20}$$

where, f_x and f_y are components of a force in the domain border. $\hat{\boldsymbol{n}}$ is an unitary normal vector. Since the time-independent model is a generalized Newtonian model (GNM), the components of the tensor $\boldsymbol{T}$ are evaluated as: $T_{ij} = -pI_{ij} + \eta_v(\partial_i v_j + \partial_j v_i)$.

The terms expressed in Eqs. 3-18, 3-19, and 3-20 are substituted into Eq. 3-17. In addition, the method of Galerkin is usually employed to solve this kind of problems. The weighting functions are equal to basis functions. The vectorial weighting function $\boldsymbol{W_m}$ belongs to a 2n-dimensional space which is generated for the following functions:

$$\underbrace{\boldsymbol{W_m} = \begin{bmatrix} W_1 \\ W_2 \end{bmatrix}}_{\text{Space dim} = 2n} \tag{3-21}$$

$$\left\langle \underbrace{\begin{bmatrix}\psi_1\\0\end{bmatrix},\begin{bmatrix}\psi_2\\0\end{bmatrix},\ldots,\begin{bmatrix}\psi_n\\0\end{bmatrix}}_{n\text{ functions}},\underbrace{\begin{bmatrix}0\\\psi_1\end{bmatrix},\begin{bmatrix}0\\\psi_2\end{bmatrix},\ldots,\begin{bmatrix}0\\\psi_n\end{bmatrix}}_{n\text{ functions}}\right\rangle$$

Defining the space of weighting functions in that way, the momentum components in the conservation equation can be decoupled. Therefore, the first n basis functions correspond to the first component of momentum conservation equations since $W_2 = 0$. Likewise, the last n functions correspond to the second component of the momentum conservation equation since $W_1 = 0$.

3.2.2
Free surface flows

Free surfaces, like those present in slot coating processes, adds much more complexity in the discretization and solution of the resulting algebraic equations. In fact, it is necessary to make other considerations compared to those explained in the previous section. Actually, the position of free surfaces and the corresponding physical domain are part of the problem to be solved. Since they are unknown a priori, it is convenient to employ a fixed/reference computational domain to solve the problem. Therefore, the mapping between the computational domain and the physical domain makes the original free-surface problem highly non-linear [57].

Previous works in our research group, like Valdez [8], Siqueira [57] , and Romero [58], considered Newtonian and non-Newtonian flows in slot coating applications. As a result, their computing work and expertise were used as reference and adapted to the rheological models employed in this work. So, it is only presented a summary of the considerations made in the works cited above and the adaptations made.

Beyond the considerations and equations for a time-independent fluid, explained in the previous section, it is necessary to consider the aspects presented as follows. Firstly, it is convenient to employ a computational domain (Ω') to get the solution in the unknown physical domain (Ω). The borders of both domains are Γ and Γ' respectively. In order to transform the expressions defined in Ω into equivalent equations defined in Ω', a mapping is employed. In this mapping, the position vector $\boldsymbol{x} = (x_1, x_2)$ from the physical domain is linked to a vector $\boldsymbol{\omega} = (\omega_1, \omega_2)$, which belongs to the computational domain Ω', as sketched in Fig. 3.2.

The transformation is carried out using the Jacobian matrix of the change of coordinates:

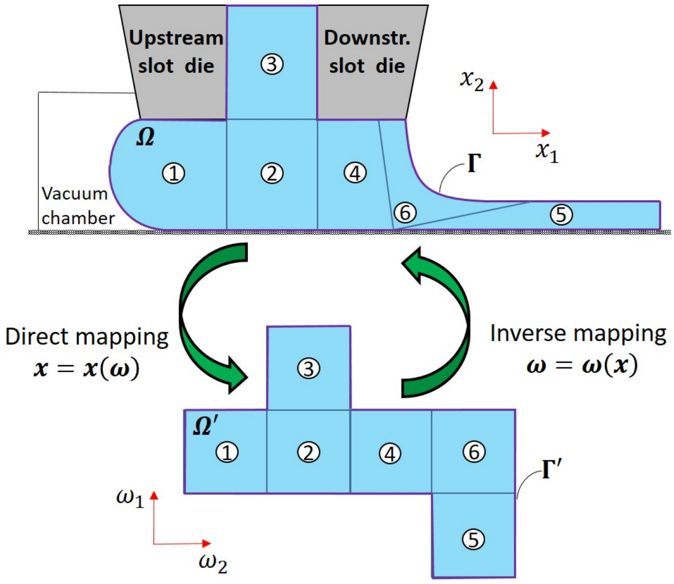

Figure 3.2: Mapping scheme between the physical and computational domain in a slot coating process

$$\frac{\partial \boldsymbol{x}}{\partial \boldsymbol{\omega}} = J_T = \begin{pmatrix} \frac{\partial x_1}{\partial \omega_1} & \frac{\partial x_2}{\partial \omega_1} \\ \frac{\partial x_1}{\partial \omega_2} & \frac{\partial x_2}{\partial \omega_2} \end{pmatrix} \tag{3-22}$$

The mapping, shown above, can be done by different techniques. The most common ones are: the method of splines [59, 60], elliptic mesh generation [61, 62], and the domain deformation method [63]. The present work makes use of elliptic mesh generation, at which the inverse mapping $\boldsymbol{\omega}(\boldsymbol{x})$ is the solution of an elliptic differential equation:

$$\nabla \cdot (\boldsymbol{\mathcal{D}}_\omega \cdot \nabla \boldsymbol{\omega}) = 0 \ , \tag{3-23}$$

where $\boldsymbol{\mathcal{D}}_\omega$ is a symmetric tensor of diffusion-like coefficients, which controls the spacing between the iso-lines of ω_1 and ω_2.

The mapping equation, i.e. Eq. 3-23, is also solved by the Finite Element Method. After some arrangements and applying the Gauss-Green-Ostrogradskii theorem, the weak form of Eq. 3-23 can be expressed as:

$$\begin{aligned} R_E \;=\; & \int_{\Omega'} (\nabla \boldsymbol{W_E} \cdot \boldsymbol{\mathcal{D}}_\omega \cdot \nabla \boldsymbol{\omega}) ||J_T||\, d\Omega' + \\ & - \oint_{\Gamma'} \hat{\boldsymbol{n}} \cdot (\boldsymbol{\mathcal{D}}_\omega \cdot \nabla \boldsymbol{\omega}) \cdot \boldsymbol{W_E} \frac{d\Gamma}{d\Gamma'}\, d\Gamma' \;=\; 0 \end{aligned} \tag{3-24}$$

where $||J_T||$ is the determinant of J_T. The weighting functions of $\boldsymbol{W_E}$ are the same for $\boldsymbol{W_m}$. Galerkin´s method is also used, and therefore the basis and weight functions are the same. Regarding the position of a 2D free surface can be expressed as:

$$\boldsymbol{x} = \begin{bmatrix} x \\ y \end{bmatrix} = \begin{bmatrix} \sum\limits_{j=1}^{n} X_j \psi_j \\ \sum\limits_{j=1}^{n} Y_j \psi_j \end{bmatrix} \tag{3-25}$$

With Eq. 3-24 and the residual equations presented in the previous section, R_c and R_m, we have the system of coupled equations to obtain a flow solution in a free boundary problem.

3.2.3
Weighted residual equations for the thixotropic model

In the case of thixotropic liquids, the non-Newtonian model includes an extra differential equation, which describes the evolution equation of fluidity. The weak form of this evolution equation of fluidity is presented as follows:

$$R_t = \int_{\Omega'} [\boldsymbol{v} \cdot \nabla \phi_v^* - F(\phi_v^*, \sigma)] W_t \|J_T\| \, d\Omega' = 0 \ , \tag{3-26}$$

where ϕ_v^* is dimensionless fluidity which ranges from 0 to 1. W_t is the weighting function for the fluidity evolution equation.

Gathering all weak forms of the differential equations, considering the mapping between the physical and computational domain, and substituting the weighting functions W_i by basis functions (Excepting in the weighted residual equation for fluidity and the reason is explained in the next section); we have the following set of weighting residuals:

$$R_{ci} = \int_{\Omega'} (\nabla \cdot \boldsymbol{v}) \, \psi_{ci} \|J_T\| \, d\Omega' \ , \tag{3-27}$$

$$\begin{aligned} \boldsymbol{R_{mi}} = & \int_{\Omega'} \rho (\boldsymbol{v} \cdot \nabla \boldsymbol{v}) \psi_{mi} \|J_T\| \, d\Omega' + \int_{\Omega'} \boldsymbol{T} \cdot \nabla \psi_{mi} \|J_T\| \, d\Omega' + \\ & - \oint_{\Gamma'} (\hat{\boldsymbol{n}} \cdot \boldsymbol{T}) \psi_{mi} \frac{d\Gamma}{d\Gamma'} \, d\Gamma' \ , \end{aligned} \tag{3-28}$$

$$\boldsymbol{R_{Ei}} = \int_{\Omega'} \nabla \psi_{Ei} \cdot (\boldsymbol{\mathcal{D}}_{\omega} \cdot \nabla \boldsymbol{\omega}) \|J_T\| \, d\Omega' - \oint_{\Gamma'} \hat{\boldsymbol{n}} \cdot (\boldsymbol{\mathcal{D}}_{\omega} \cdot \nabla \boldsymbol{\omega}) \psi_{Ei} \frac{d\Gamma}{d\Gamma'} \, d\Gamma' \ , \tag{3-29}$$

$$R_{ti} = \int_{\Omega'} [\boldsymbol{v} \cdot \nabla \phi_v^* - F(\phi_v^*, \sigma)] \vartheta_{\phi i} \|J_T\| \, d\Omega' \ , \tag{3-30}$$

where ψ_{ki} are basis functions and $\vartheta_{\phi i}$ are the weighting functions used for fluidity, "i" is the index referred to degree of freedom.

3.2.4
Expansion of the unknown fields

According to the FEM formulation, the independent variables of the problem are written as a linear combination of a finite number of basis functions:

$$\boldsymbol{v} = \sum_{j=1}^{n} \boldsymbol{V_j} \psi_{mj} \ , \tag{3-31}$$

$$\boldsymbol{x} = \sum_{j=1}^{n} \boldsymbol{X}_j \psi_{Ej} \ , \tag{3-32}$$

$$p = \sum_{j=1}^{m} P_j \psi_{cj} \ , \tag{3-33}$$

$$\phi_v^* = \sum_{j=1}^{n} \Phi_j \psi_{\phi j} \ . \tag{3-34}$$

Usually, the basis functions ψ_{ki} are piecewise polynomials of low degree. The basis functions used to expand the unknown fields, presented in Eqs. 3-31 - 3-34, are listed in table 3.1.

Table 3.1: Basis functions used to expand the unknown fields.

Variable	Basic function
$\boldsymbol{v}$	Lagrangian biquadratic
$\boldsymbol{x}$	Lagrangian biquadratic
p	Linear discontinuous
ϕ_v^*	Lagrangian biquadratic

Galerkin's method (weighting functions = basis functions) is used to solve the elliptic mesh generation, mass and momentum conservation equations (denoted as ψ_{ki} in Eqs. 3-27 - 3-29). The use of Galerkin's method for Eq. 3-30 generates numerical instabilities which affect the accuracy of the solution. This phenomenon is remarkable in differential equations which are strongly convective (i.e. with strong hyperbolic terms) [57]. The solution, of this issue, is the implementation of the Streamline-Upwinding Petrov-Galerkin (SUPG) formulation, where the fluidity weighting function is defined as:

$$\vartheta_\phi = \psi_\phi + h^U (\boldsymbol{v} \cdot \nabla \psi_\phi) \ , \tag{3-35}$$

where, ψ_ϕ is the basis function and h^U is the upwind coefficient, which was fixed according to the characteristic size of the smallest element in the computational mesh.

3.2.5
Element analysis

The computational domain is discretized with quadrilateral elements. Accordingly, each element contains nine nodes: one at each corner, one at the midpoint at each side and one at the center. Figure 3.3 provides some details of the element features.

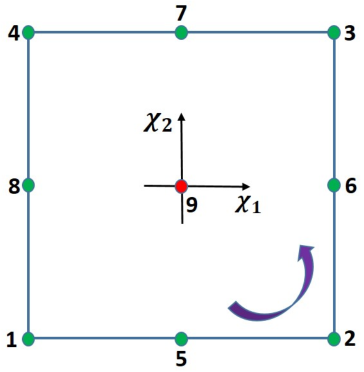

Figure 3.3: Representation of the quadrilateral finite elements used to discretize the flow domain

The velocity field, fluidity field and mesh coordinates are evaluated in all nodes. Therefore, each these variables contains 9 degrees of freedom per element. The center of each element, in particular, has also 3 degrees of freedom related to the pressure field. The number of degrees of freedom for each variable of the problem for a given element is summarized in the following table 3.2.

Table 3.2: Degrees of freedom of each variable per element

Variable	Degree of freedom
$\boldsymbol{v}$	9
$\boldsymbol{x}$	9
p	3
ϕ_v^*	9

It is important to note that pressure and fluidity are scalars, while velocity and mesh coordinate are vectors. Therefore, the components of the vector considered in the problem (i.e. 2D or 3D) should be taken into account in estimating the total degrees of freedom in the simulation.

3.3
Solution of systems of non-linear equations by the Newton method

To get an acceptable solution of the system of equation mentioned above, it is set a maximum tolerance (ϵ) of the L_2-norm of the global residual vector $\boldsymbol{R}(\boldsymbol{C},\boldsymbol{\wp})$. $\boldsymbol{C}$ is the vector of the unknowns, while $\boldsymbol{R}$ is the residual vector obtained from Eqs. 3-27 - 3-30. $\boldsymbol{\wp}$ is a vector of flow parameters which also affects the value of $\boldsymbol{R}$. The residual vector is satisfied if:

$$\boldsymbol{R}(\boldsymbol{C},\boldsymbol{\wp}) = \boldsymbol{0} \tag{3-36}$$

The non-linear system (Eq. 3-36) is solved by Newton's method, at which the solution update is the solution of the system:

$$\boldsymbol{J}\Delta\boldsymbol{C} = -\boldsymbol{R}(\boldsymbol{C}^k, \boldsymbol{\wp}) \ , \tag{3-37}$$

and,

$$\boldsymbol{C}^{k+1} = \Delta\boldsymbol{C} + \boldsymbol{C}^k \ , \tag{3-38}$$

$\boldsymbol{J}$ is Jacobian matrix, defined as:

$$J_{ij} = \frac{\partial R_i}{\partial C_j} \ . \tag{3-39}$$

The elements of the Jacobian matrix can be obtained in an analytical or a numerical way. Due to the complexity of the problem, in the present work, they were obtained by a numerical method which considers central derivatives as shown as follows:

$$J_{ij} = \frac{R_i(C_1, ..., C_j + \epsilon, ...) - R_i(C_1, ..., C_j - \epsilon, ...)}{2\epsilon} \tag{3-40}$$

The iterative process begins with a initial guess, $\boldsymbol{C}^0$, and it continues until Eq. 3-36 is satisfied. It means that the L_2 norm of the residual and solution vectors should satisfy the following expression:

$$||\Delta\boldsymbol{C}||_2 + ||\Delta\boldsymbol{R}||_2 \leq \epsilon \ , \tag{3-41}$$

where ϵ is usually 10^{-6}.

In each iteration, the resulting Jacobian matrix $\boldsymbol{J}$ is solved by LU decomposition using the Frontal method proposed by Hood [64]. Likewise, it is not necessary inversion of the matrix $\boldsymbol{J}$ and $\Delta\boldsymbol{C}$ is relatively easy to get from Eq. 3-37.

4
Flow through a constricted capillary

This chapter reports the results related to the first situation analyzed in this work: flow through a constricted microcapillary. Despite being simple, a fluid particle flows through a region at which the microstructure is in equilibrium (before the constriction), through a region at which the structure is destroyed (converging section) and through a region at which the microstructure is recovered (diverging section) until reaching equilibrium in the outlet tube. Two rheological models are used. One is able to model thixotropy while the other is a time-independent model that does not takes into account the time dependent effects. The goal of this analysis is to compare the flow behavior predicted by both models employed. This comparison will allow to determine the condition at which a simple time-independent model is able to accurately describe the flow.

In the analysis reported here, we used the laponite suspension used by Souza Mendes et al. [9] as the flowing liquid. Most results and the methodology shown here were published in Sanchez-Perez et al.[65].

4.1
Mathematical model

We consider a small-scale, steady-state flow of a non-Newtonian liquid that exhibits shear-thinning and thixotropy. Gravitational forces are neglected. The flow is described by incompressible mass and momentum conservation equations:

$$\nabla \cdot \boldsymbol{u} = 0 \ , \tag{4-1}$$

and,

$$\rho \boldsymbol{u} \cdot \nabla \boldsymbol{u} = \nabla \cdot \boldsymbol{T}, \tag{4-2}$$

where $\boldsymbol{u}$ is the velocity vector, ρ is the liquid density, $\boldsymbol{T}$ is the stress tensor. The stress tensor is split as $\boldsymbol{T} = -p\boldsymbol{I} + \boldsymbol{\sigma}$, where p is the pressure field, $\boldsymbol{I}$ is the identity tensor, and $\boldsymbol{\sigma}$ is the extra stress. The latter obeys Newton's law of viscosity, $\boldsymbol{\sigma} = \eta_v(\nabla \boldsymbol{u} + \nabla \boldsymbol{u}^T)$, where η_v is the local viscosity of the liquid.

4.1.1
Rheological models

Two different rheological models are considered in the analysis. The first model neglects fluid time-dependent effects and assumes that the viscosity at each point is a function of the local deformation rate $\dot{\gamma}$. From now on, this model is referred here as the *time-independent model (TIM)*.

$$\eta_v = \eta_v(\dot{\gamma}) \tag{4-3}$$

The function $\eta_v(\dot{\gamma})$ is obtained experimentally and it is generally referred to as the liquid flow curve. As liquid of reference was used a laponite suspension, described in section 2.2.2. The yield stress of the laponite suspension was low and we set its value to zero to ease the numerical convergence. In addition, this value was low for the suspension studied. Furthermore, ϕ_0 was fixed at 10^{-3} $(Pa.s)^{-1}$. The latter parameter is not strictly equal to zero and the literature reports it in the range of 10^{-5} – 10^{-3} $(Pa.s)^{-1}$. The flow curve and the corresponding variation of ϕ^*_{eq} with the local stress is presented in Fig. 4.1.

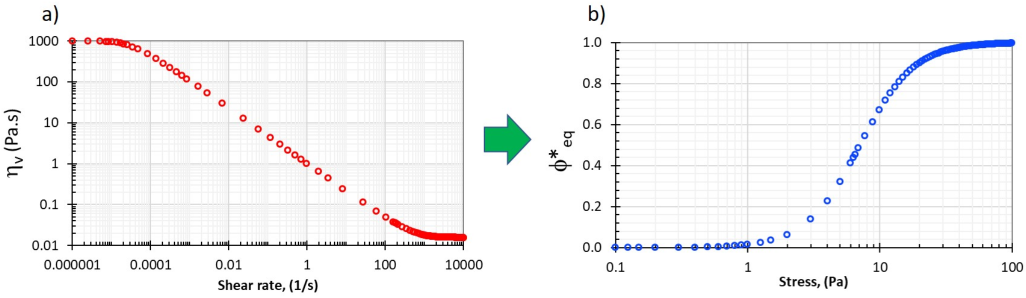

Figure 4.1: a) Steady state viscosity as function of the shear rate; b) Normalized equilibrium fluidity as function of shear stress for a hypothetical suspension with $\sigma_y = 0$ Pa and $\phi_0 = 10^{-3}(Pa.s)^{-1}$

The fluidity equation, ϕ^*_{eq}, shown in Fig. 4.1, is given by:

$$\phi^*_{eq}(\sigma) = \frac{\frac{1}{\sigma}\left[\frac{\sigma}{K}\right]^{1/n}}{(\phi_\infty - \phi_0) + \frac{1}{\sigma}\left[\frac{\sigma}{K}\right]^{1/n}}, \tag{4-4}$$

where for the laponite suspension used as example by Souza Mendes et al. [9], $K = 1$ $Pa.s^n$, $n = 0.32$, $\phi_\infty = 64.1(Pa.s)^{-1}$, and $\phi_0 = 10^{-3}(Pa.s)^{-1}$.

Having in mind the concept of fluidity (i.e. reciprocal of viscosity) and the definition of normalized fluidity, the steady-state viscosity as a function of the local stress is written as:

$$\eta_v(\sigma) = 1/\phi_v = \left[\phi^*_{eq}(\sigma)(\phi_\infty - \phi_0) + \phi_0\right]^{-1} \tag{4-5}$$

The second model takes into account the fluid time-dependent response, and is referred here as the *thixotropic model*. The mechanical response of the liquid is described by the model proposed by de Souza Mendes et al.[9]. The main advantage of this model, when compared to existing phenomenological models for thixotropic materials, is that the evolution equation that describes the microscopic state only involves material functions that are directly measurable by means of standard rheological tests. This model is described in detail in section 2.2.2. The evolution equation for fluidity is written as Eq. 4-6. The function that describes the rate of change of fluidity $F(\phi_v^*, \phi_{eq}^*(\sigma))$ is written using two different functional forms, depending whether the structure is being broken or recovered, as shown in Eq. 4-7.

$$\boldsymbol{v} \cdot \nabla \phi_v^* = F(\phi_v^*, \phi_{eq}^*(\sigma)) \ , \tag{4-6}$$

$$F(\phi_v^*, \phi_{eq}^*(\sigma)) = \begin{cases} f_b = \frac{s}{t_a \phi_{eq}^*(\sigma)} (\phi_{eq}^* - \phi_v^*)^{\frac{s+1}{s}} \phi_v^{*\frac{s-1}{s}}, & 0 < \phi_v^* \leq \phi_{eq}^* \\ \\ f_c = -\frac{(\phi_v^* - \phi_{eq}^*)}{t_c}, & \phi_{eq}^* < \phi_v^* \leq 1 \end{cases} \tag{4-7}$$

where, the avalanche time t_a and the exponent s are a function of the equilibrium fluidity, as shown in the previous chapter.

$$t_a(\phi_{eq}^*) = 59.2 \frac{(1 - \phi_{eq}^*)^{1.1}}{\phi_{eq}^{*\ 0.4}}, \tag{4-8}$$

$$s = \frac{8}{\exp(\phi_{eq}^*/0.09) - 1} + 1.2. \tag{4-9}$$

The functional form for $\phi_{eq}^* < \phi_v^* \leq 1$ represents the structure buildup dynamics. For the laponite suspension, the construction time is $t_c = 663$ s.

For simplicity $F(\phi_v^*, \phi_{eq}^*(\sigma))$, from Eq. 4-7, is written as a single function (not as function by parts) as follows:

$$F(\phi_v^*, \phi_{eq}^*(\sigma)) = H(\phi_v^* - \phi_{eq}^*) f_c + [1 - H(\phi_v^* - \phi_{eq}^*)] f_b \ , \tag{4-10}$$

where, $H(\phi_v^* - \phi_{eq}^*)$ is a smooth Heaviside function, which is given by Eq. 4-11, and it is compared to the traditional Heaviside function in Fig. 4.2.

$$H(\phi_v^* - \phi_{eq}^*) = \frac{1}{2} \left\{1 + tanh[m(\phi_v^* - \phi_{eq}^*)]\right\} \tag{4-11}$$

where, m is a scalar factor which is the steepness intensity of the smoothed Heaviside function. In other words, if m is large the curve will be steep.

It is important to mention that the functional forms presented in Eq. 4-7

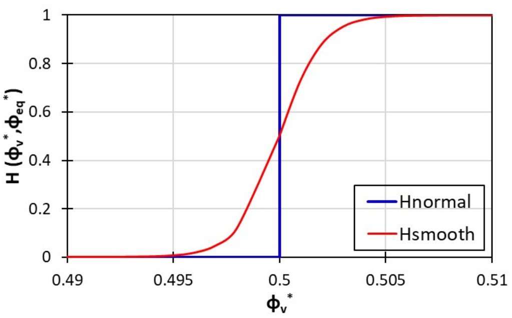

Figure 4.2: Normal and smooth Heaviside functions vs fluidity for ϕ^*_{eq}= 0.5 and m = 500

were proposed based on the rheological response of a laponite suspension. The functional form $F(\phi^*_v, \phi^*_{eq}(\sigma))$ will change with the fluid rheological response.

4.1.2
Flow geometry and boundary conditions

We investigate the flow through a constricted capillary tube. Although simple, the flow kinematics show regions of fully developed flow, at which the fluidity is in equilibrium along every streamline, regions of structure breakdown, in the converging section of the throat, and regions of structure buildup, in the diverging part of the constriction.

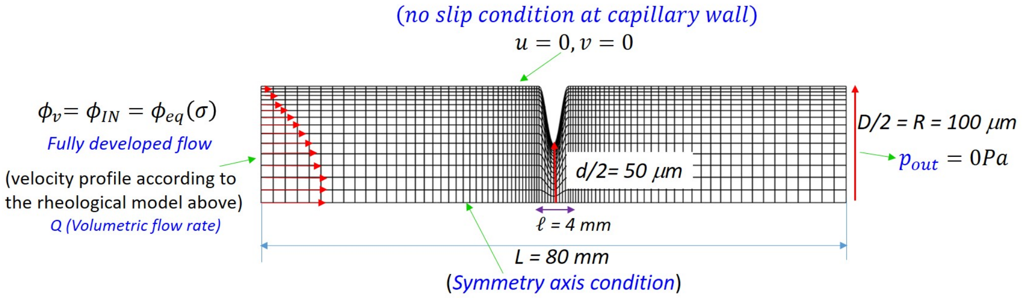

Figure 4.3: Sketch of the flow domain (not to scale).

A sketch of the geometry of the problem is shown in Fig.4.3, where D is the capillary tube diameter and d is the throat diameter, L is the capillary length and l is the length of the constricted portion of the tube.

The boundary conditions for the flow through the constricted capillary are the following. At the synthetic inflow plane, fully developed flow is assumed. The velocity $\boldsymbol{u}(r)$ profile at a set flow rate Q, which corresponds to a equilibrium fluidity $\phi^*_{eq}(\sigma(r))$, is imposed. Along the capillary wall, the no-slip and no-penetration conditions are imposed, i.e. $\boldsymbol{u} = 0$. Vanishing radial velocity and zero shear stress are considered along the symmetry axis. A pressure value $p_{out} = 0$ is imposed along the synthetic outflow plane. Because the fluidity transport equation, Eq. 4-6, is hyperbolic, we only need to impose a fluidity profile along the inlet plane. Because we assume a fully developed flow, the value of the fluidity corresponds to the equilibrium fluidity at the local stress level, i.e. $\phi_v^*(r) = \phi_{eq}^*(\sigma(r))$.

4.1.3
Velocity profile as boundary condition

Looking back the boundary conditions shown in Fig. 4.3, it is possible to appreciate the necessity of imposing a coherent velocity profile at the capillary inlet. In fact, this velocity profile corresponds to a fully developed flow at equilibrium condition. An illustration of this flow is presented in Fig. 4.4.

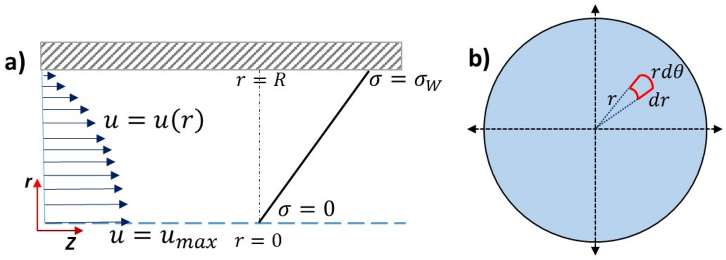

Figure 4.4: Sketch of the microcapillary before the constriction: a) fully developed flow, b) differential area of a portion of liquid

The fully developed velocity profile is obtained from Eq. 4.1. Combining Eqs. 2-8, 2-15, 2-17, and 4-4 and considering $\phi_\infty >> \phi_0$, the local shear rate is written as a function of local stress:

$$\dot{\gamma} = -\frac{du}{dr} = \frac{\sigma}{\eta_\infty + \frac{\sigma}{(\sigma/K)^{1/n}}} \,, \tag{4-12}$$

η_∞ is just the reciprocal of ϕ_∞. The velocity profile is obtained by integrating Eq. 4-12 and considering no slip at the capillary wall, i.e. $\boldsymbol{u}(R) = 0$.

$$u(r) = \int_r^R \frac{\sigma}{\eta_\infty + \frac{\sigma}{(\sigma/K)^{1/n}}} dr \tag{4-13}$$

Making some arrangements and considering the dimensionless radial distance $\xi = r/R$, we have:

$$u(\xi) = R \int_\xi^1 \frac{1}{(\sigma_w \xi)^{-1} \eta_\infty + K^{1/n} [\sigma_w \xi]^{-1/n}} d\xi \,, \tag{4-14}$$

where, σ_w is the wall stress.

The analytical expression for the integral of Eq. 4-14 is obtained by applying the Newton's binomial theorem. Two possible solutions exist:

$$u(\xi) = \frac{R}{1/n + 1}\left(\frac{\sigma_w}{K}\right)^{1/n}\left[{}_2F_1(a,b;c;d|_{\xi=1}) - (\xi)^{1/n+1}{}_2F_1(a,b;c;d|_{\xi})\right] , \qquad (4\text{-}15)$$

$$u(\xi) = \frac{R\sigma_w}{2\eta_\infty}\left[{}_2F_1(a^*,b^*;c^*;d^*|_{\xi=1}) - (\xi)^2{}_2F_1(a^*,b^*;c^*;d^*|_{\xi})\right] , \qquad (4\text{-}16)$$

${}_2F_1(a,b;c;d|_\xi)$ and ${}_2F_1(a^*,b^*;c^*;d^*|_\xi)$ are Gaussian hypergeometric functions, where:

$$a = 1,\ b = \frac{n+1}{1-n},\ c = -\frac{2}{n-1},\ d = -\frac{\eta_\infty\left(\frac{K}{\sigma_w \xi}\right)^{\frac{n-1}{n}}}{K}, \qquad (4\text{-}17)$$

and,

$$a^* = 1,\ b^* = \frac{2n}{n-1},\ c^* = \frac{3n-1}{n-1},\ d^* = -\frac{K}{\eta_\infty\left(\frac{K}{\sigma_w \xi}\right)^{\frac{n-1}{n}}}. \qquad (4\text{-}18)$$

Gaussian hypergeometric functions ${}_2F_1(a,b;c;d)$ for $|d|<1$ are defined by power series [66]:

$${}_2F_1(a,b;c;d) = 1 + \frac{ab}{c}\frac{d}{1!} + \frac{a(a+1)b(b+1)}{c(c+1)}\frac{d^2}{2!} + \ldots = \sum_{i=0}^{\infty}\frac{(a)_i(b)_i}{(c)_i}\frac{d^i}{i!} , \qquad (4\text{-}19)$$

where $(a)_i$, $(b)_i$, and $(c)_i$ are Pochhammer symbols, which are rising factorial numbers defined as:

$$(a)_i = a(a+1)(a+2)(a+3)\ldots(a+i-1) , \qquad (4\text{-}20)$$

$(a)_0$, $(b)_0$, and $(c)_0$ are equal to 1 by definition.

The validity of Eq. 4-15 is restricted to the convergence of the hypergeometric function ${}_2F_1(a,b;c;d)$, where $|d|$ should be lower than 1 in the whole domain. In other words, the critical point ξ_c (defined considering $|d| = 1$) should satisfy the condition: ξ_c>1. At ξ_c=1, it is defined the critical wall stress $\sigma_{w,c}$; which is given by Eq. 4-21. When $\sigma_w < \sigma_{w,c}$, the velocity profile is defined by Eq. 4-15.

$$\sigma_{w,c} = K(K\phi_\infty)^{\frac{n}{1-n}} \qquad (4\text{-}21)$$

For the rheological data by Souza Mendes et al.[9], n=0.32, K=1 $Pa.s^n$, and ϕ_∞=64.1 $(Pa.s)^{-1}$, $\sigma_{w,c}$ is about 7.1 Pa. Therefore, the velocity profile for σ_w<7.1 Pa is defined by Eq. 4-15. Otherwise, the velocity profile is given by Eq. 4-22.

$$u(\xi) = \begin{cases} u_c + u_I(\xi), & 0 \le \xi \le \xi_c \\ \\ u_{II}(\xi), & \xi_c < \xi \le 1 \end{cases} \tag{4-22}$$

where,

$$u_I(\xi) = \frac{R}{1/n+1}\left(\frac{\sigma_w}{K}\right)^{1/n}\left[(\xi_c)^2{}_2F_1(a,b;c;d|_{\xi_c}) - (\xi)^{1/n+1}{}_2F_1(a,b;c;d|_{\xi})\right],$$

$$u_{II}(\xi) = \frac{R\sigma_w}{2\eta_\infty}\left[{}_2F_1(a^*,b^*;c^*;d^*|_{\xi=1}) - (\xi)^2{}_2F_1(a^*,b^*;c^*;d^*|_{\xi})\right],$$

$$u_c = \frac{R\sigma_w}{2\eta_\infty}\left[{}_2F_1(a^*,b^*;c^*;d^*|_{\xi=1}) - (\xi_c)^2{}_2F_1(a^*,b^*;c^*;d^*|_{\xi_c})\right],$$

and,

$$\xi_c = \frac{K}{\sigma_w}(K\phi_\infty)^{\frac{n}{1-n}}.$$

$u_I(\xi)$ and $u_{II}(\xi)$ from Eq. 4-22 were obtained by arranging Eqs. 4-15 and 4-16 respectively and taking ξ_c into account. Since $|d^*| = 1/|d|$, it was considered the velocity profile with ${}_2F_1(a^*,b^*;c^*;d^*|_{\xi})$ when d>1 (i.e. $\xi_c < \xi \le 1$).

To estimate σ_w for a given volumetric flow rate Q, it is necessary to use an iterative numerical methodology. As initial guess, it is estimated by the analytical expression (Eq. 4-23) obtained from Power-law model.

$$\sigma_w = K\left[\frac{(1/n+3)Q}{\pi R^3}\right]^n \tag{4-23}$$

σ_w obtained in Eq. 4-23 can be used to determine the wall stress coherent to Eq. 4-4. The velocity profile is selected according to the value of σ_w calculated. In the case of σ_w<7.1 Pa, it is selected the velocity profile given by Eq. 4-15. Otherwise, it is selected the velocity profile given by Eq. 4-22. Then, the assumed velocity profile is integrated according to Eq 4-24. After that, the computed flow rate value Q (from Eq 4-24) is compared to the set value of the volumetric flow rate. Since Power-law model tends to underestimate correct values of Q, the value of σ_w is gradually increased until approaching the set value of the volumetric flow rate.

$$Q = \int_0^{2\pi}\int_0^R urdrd\theta \tag{4-24}$$

Following the procedure described above, it was estimated the value of

Q at σ_w=7.1 Pa. The corresponding value of Q is 0.135 mm^3/s. Therefore, the velocity profile for Q<0.135 mm^3/s is defined by Eq. 4-15. Otherwise, the velocity profile is defined by Eq. 4-22.

Three velocity profiles are presented in Fig. 4.5. The profiles correspond to Q=3.5, 0.05, and 0.0038 mm^3/s respectively.

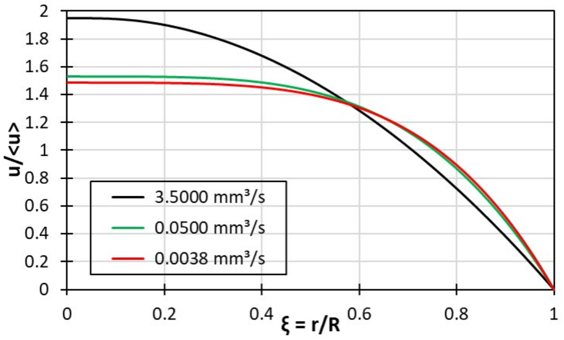

Figure 4.5: Dimensionless velocity profiles at the capillary inlet (n=0.32)

In Fig. 4.5, the velocity profiles are presented as the dimensionless ratio $u/<u>$, where $<u>$ is the average velocity at the inlet (calculated as $Q/\pi R^2$). According to this graph, it is possible to appreciate the similarity between the velocity profiles at Q=0.0038 and 0.05 mm^3/s. On the other hand, the velocity profile for Q=3.5 mm^3/s is completely different compared to the other two shown in the graph.

For very small flow rates Q, the corresponding values of σ_w and d are very small as well. In the case of $d \to 0$: ${}_2F_1(a,b;c;d|_\xi) \to 1$ and the dimensionless form of the velocity profile given by Eq. 4-15 is very similar to that obtained from Power-law model, which is presented in Eq. 4-25. This velocity profile only depends on the parameter n for a fixed value of ξ.

$$\frac{u}{<u>} = \frac{1/n+3}{1/n+1}[1-(\xi)^{1/n+1}] \tag{4-25}$$

As Q increases, d does not tend to zero anymore and the influence of other parameters becomes important. Therefore, it is necessary to use more complex velocity profiles like those presented in Eqs. 4-15 and 4-22.

4.1.4
Dimensionless numbers

A dimensional analysis of the problem suggests the definition of the following dimensionless groups:

1. Constriction ratio, defined as the ratio of throat to capillary diameter:

   $$\overline{D} \equiv \frac{d}{D}.$$

2. Dimensionless constriction length, defined as:

   $$\bar{l} \equiv \frac{l}{D}.$$

3. Reynolds number, which represents the ratio of inertial and viscous forces, defined as:

   $$Re \equiv \frac{4\rho\phi_0}{\pi D}Q.$$

   Because of the small dimension and flow rate range, the maximum Reynolds number of the cases explored here was $\approx 10^{-5}$. Therefore, inertial effects are not important to the dynamics of the flow.

4. Dimensionless wall stress, which quantifies the flow strength in the straight portion of the capillary, defined as:

   $$\tau \equiv \frac{K}{\sigma^*}\Big[\frac{Q}{\pi D^3}(1/n + 3)\Big]^n \frac{l}{D},$$

   where σ^* is the stress value at which the liquid is almost fully unstructured and the dimensionless equilibrium fluidity is equal to $\phi^*_{eq} = 0.95$. For the fluidity model used here, Eq. 4-4, it is given by

   $$\sigma^* = \Big[\frac{0.95}{0.05}K^{1/n}(\phi_\infty - \phi_0)\Big]^{\frac{n}{1-n}}.$$

   For the rheological parameters of the laponite suspension [9], $\sigma^* = 28.3$ Pa. High values of τ indicate that the liquid microstructure in the inlet channel is almost fully broken; the flow through the high deformation rate region near the constriction does not change the liquid microstructure state.

5. Structure number, defined as the ratio of the liquid fluidity at the fully unstructured and fully structured states:

   $$Str \equiv \frac{\phi_\infty}{\phi_0}.$$

6. Power-law index n.

7. Thixotropy number, defined as the ratio of the construction time to the liquid residence time in the constriction region:

$$\Lambda \equiv \frac{4Qt_c}{\pi D^2 l}.$$

This is the inverse of the Mutation number Mu, defined by Mours and Winter [67] and discussed in detail by Jamali and McKinley [68].

All results reported here were obtained considering $Str = 6.41 \times 10^4$, $\overline{D} = 0.5$ and $\bar{l} = 20$.

4.2
Solution method

Numerical solutions were obtained via finite element approximations of Eqs.4-1, 4-2, and 4-6 (when using the thixotropic model) with the appropriate boundary conditions.

The independent variables of the problem, i.e. velocity, pressure and fluidity (for the thixotropic model) fields, are written as a linear combination of a finite number of basis functions. Lagrangian biquadratic functions are used to represent velocity field, linear discontinuous functions are used for the pressure field, and Lagrangian biquadratic functions are used for fluidity. Galerkin's weighting functions are used in the residual equations of mass and momentum conservation, whereas the stabilized Streamline-Upwind Petrov-Galerkin formulation is applied to the fluidity transport equation. The upwinding parameter was defined as the characteristic size of the smallest element in the computational mesh. These methods are explained in more detail in chapter 3.

The flow domain was divided into quadrangular finite elements using a computational mesh with 7,900 elements and 32,431 nodes. Stretching functions were used to concentrate elements near the contraction and channel walls. The solutions were mesh-independent with this level of discretization. The G/SUPG FEM formulation reduces the fully coupled, non-linear set of differential equations to a large, sparse set of coupled, non-linear algebraic equations with 120,993 degrees of freedom for the thixotropic model and 88,562 degrees of freedom for the generalized Newtonian model. The difference corresponds to the fluidity degrees of freedom. The resulting set of non-linear equations was solved by Newton's Method with a numerical Jacobian matrix calculated using a second-order central difference scheme. The tolerance on the L_2-norm of the Newton update and of the global residual vector were both set to 10^{-6}. At each iteration of Newton's Method, the linear system was solved with a frontal solver based on the LU factorization scheme. Solutions were obtained using a computer with an Intel Core i7-7700, 3601 MHz processor, 8.00 GB (RAM), 4 Cores. Each Newton iteration took approximately 39 seconds for the thixotropic model and 7 seconds for the time-independent model.

4.3
Results and discussion

The main goal of the analysis is to compare the flow behavior obtained by the time-independent model, which neglects time-dependent effects, and the thixotropic model. The results reveal at which conditions a simple time-independent model suffices to accurately describe the flow.

4.3.1
Parametric analysis, where $t_a = t_c$

Although the model was presented in the previous section with the rheological parameters of the laponite suspension used by de Souza Mendes et al.[9], we first present results of a parametric analysis to study the effect of the characteristic time of the liquid, represented by the thixotropy number Λ, on the flow dynamics, with all the other dimensionless parameters fixed. Therefore the results discussed next do not represent the behavior of a particular fluid. To simplify the analysis, the equilibrium fluidity ϕ^*_{eq} as a function of the local stress used in the parametric study is that of the laponite suspension [9], described in Eq. 4-4. The avalanche time is set to be equal to the construction time, i.e. $t_a = t_c$, and both are considered as the independent parameters in the analysis. The Structure number is fixed at $S = 6.41 \times 10^4$.

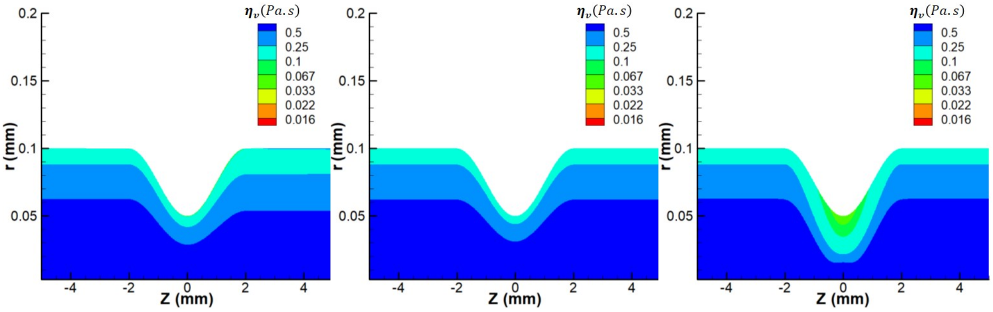

Figure 4.6: Viscosity field near the capillary constriction at $\tau = 0.8$: (a) thixotropic model, $\Lambda = 3.3$, (b) thixotropic model, $\Lambda = 776$, (c) time-independent model.

Figure 4.6 shows the viscosity field predicted by both models at $\tau = 0.8$. The thixotropic predictions shown are at $\Lambda = 3.3$ (a) and $\Lambda = 776$ (b). The

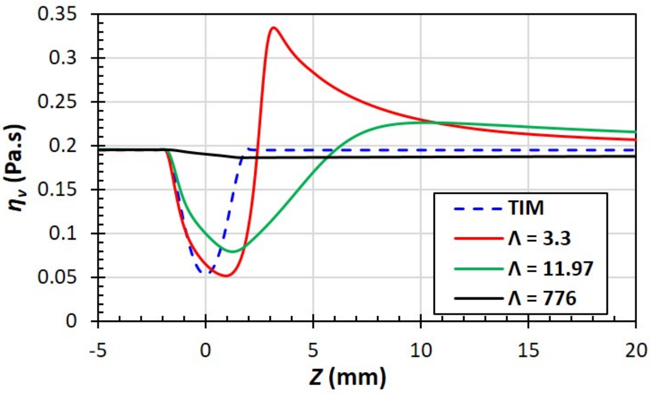

Figure 4.7: Viscosity along the capillary wall for the time-independent model and thixotropic model at different values Λ. $\tau = 0.8$.

viscosity field in the time-independent model predictions is symmetric with respect to $z = 0$; the viscosity is a function of the local deformation rate, which is symmetric in low Reynolds number flow. For the thixotropic model, the viscosity is a function of the liquid structure evolution along a streamline. The viscosity field is not symmetric. At high thixotropy number, the liquid does not have enough time to fully break its structure as it flows through the converging section of the constriction. Clearly the viscosity predicted by the thixotropic model near the throat is higher than that predicted by the time-independent model. The viscosity along the capillary wall for the time-independent model and for the thixotropic model at different values of Λ is shown in Fig. 4.7. Upstream of the constriction, the viscosity is independent of Λ; the flow is fully developed, and the fluidity is only a function of the local stress.

For the time-independent model, the viscosity is lower near the constriction because of the higher shear rate in that region, reaching a minimum value of $\eta = 0.053$ Pa.s. At $\Lambda = 776$, the construction time is so large that the rate of change of the structure level almost vanishes. The viscosity is almost constant along the capillary wall. The higher viscosity in the constriction region leads to larger pressure difference. As the thixotropy number falls, i.e. as the liquid response time decreases, the viscosity in the constriction region falls, approaching the time-independent model profile as $\Lambda \to 0$.

At each set of parameters, the pressure drop Δp^* in the constriction region, from $z = -10$ mm to $z = +10$ mm, was evaluated for both the thixotropic model and time-independent model. The ratio between both pressure drops, defined in Eq. 4-26, was computed as a function of the thixotropy number to evaluate the effect of the time-dependent response of the liquid on the flow characteristics.

$$\overline{\Delta P} \equiv \frac{\Delta p^*_{thix}}{\Delta p^*_{GNM}} \tag{4-26}$$

The results are presented in Fig. 4.8 at dimensionless wall stress $\tau = 0.8$. The pressure drop ratio approaches $\overline{\Delta P} \to 1$ as $\Lambda \to 0$, the time-independent model result is recovered as the construction time approaches zero. The equilibrium fluidity and therefore the steady-state liquid viscosity is reached almost immediately. At very high values of the thixotropy number, the pressure difference ratio is close to $\overline{\Delta P} \approx 1.55$. The pressure difference obtained using the thixotropic model is 55% higher than that predicted by the time-independent model. At these conditions, neglecting the time-dependent behavior of the liquid leads to very inaccurate results.

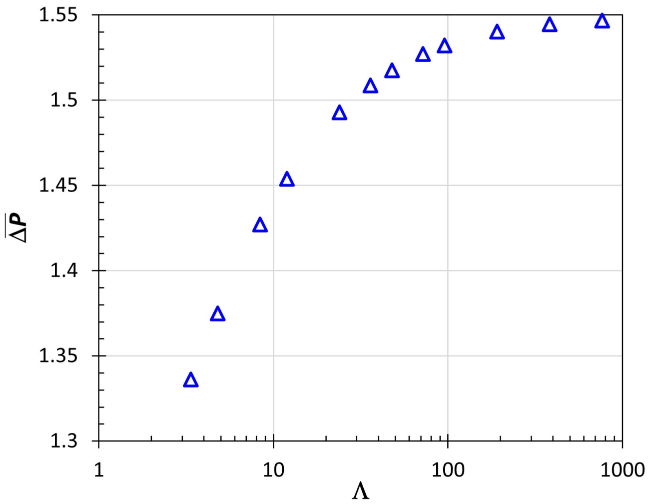

Figure 4.8: Ratio between pressure drop predicted by the thixotropic model and that predicted by the time-independent model as a function of Λ. $\tau = 0.8$.

At higher dimensionless wall stress, e.g. $\tau = 3.82$, the level of structuring of the liquid is smaller and the viscosity along the capillary wall is lower; the shear rate at the straight portion of the capillary is already high enough leading to lower values of viscosity, as indicated in Fig. 4.9. The figure presents the predicted viscosity field for the time-independent model and for the thixotropic model at $\Lambda = 6380$. The liquid structure does not have enough time to be fully destroyed as it flows through the constriction and it takes longer to built the structure back downstream of the capillary throat.

Figure 4.10 presents the viscosity along the capillary wall as a function of the thixotropy number Λ. The viscosity profiles approach the time-independent results as $\Lambda \to 0$. As in the case at lower dimensionless wall stress, the results for the time-independent model show a lower viscosity in the throat. However, the viscosity variation is much smaller. At $\Lambda = 6380$, the rate of change of the

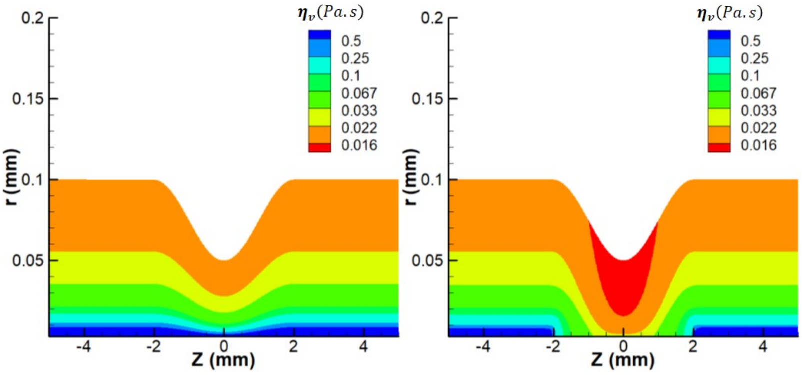

Figure 4.9: Viscosity field near the capillary constriction at $\tau = 3.82$: (a) thixotropic model, $\Lambda = 6380$, (b) time-independent model.

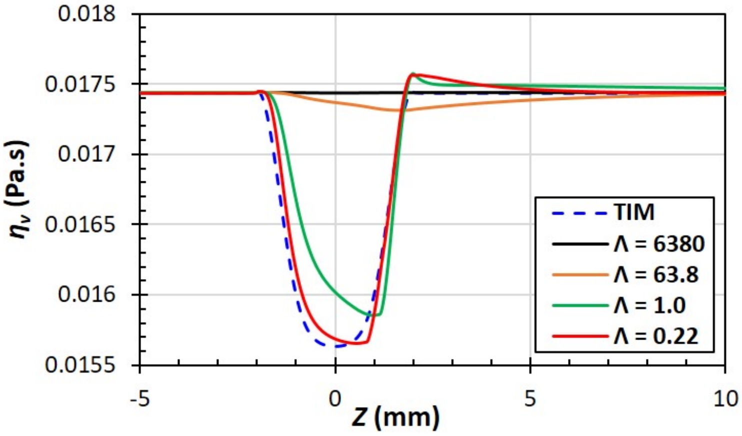

Figure 4.10: Viscosity along the capillary wall for the time-independent model and thixotropic model at different values Λ. $\tau = 3.82$

fluidity almost vanishes, the fluidity is constant along a streamline, leading to an almost constant viscosity along the capillary wall.

Because of the lower viscosity range in the flow, the effect of liquid time-dependency is weaker than in the case at lower dimensionless wall stress, as indicated in Fig. 4.11. As in the previous case, the pressure drop ratio approaches 1 as $\Lambda \to 0$, the time-independent model result is recovered as the construction time approaches zero. However, at very high values of thixotropy number, the pressure difference ratio is only equal to $\overline{\Delta P} \approx 1.1$. The pressure difference obtained using the thixotropic model is only 10% higher than that predicted by the time-independent model.

The results clearly show that the need to consider time-dependent effects on an accurate flow model depends not only on the ratio of the characteristic time of the liquid to the residence time of the flow, characterized here by the thixotropy number Λ, but also to the strength of the flow, represented here by the dimensionless wall stress. The dependence of the thixotropic behavior both

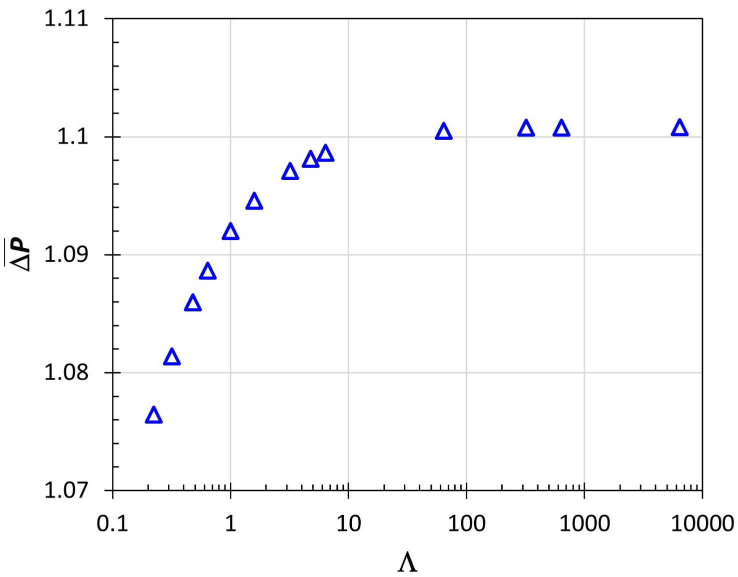

Figure 4.11: Ratio between pressure drop predicted by the thixotropic model and that predicted by the time-independent model as a function of Λ. τ = 3.82.

on the strength and the duration of the shearing history was discussed in detail by Jamali and McKinley [68]. They constructed a general two-dimensional map of thixotropic behavior.

4.3.2
Analysis according to the characteristic times (t_a, t_c) estimated for a laponite suspension

For a given liquid, i.e. fixed rheological parameters, both the thixotropy number and dimensionless wall stress vary with flow rate. The second set of results, discussed next, analyzes the evolution of the flow behavior of a laponite suspension [9] as the imposed flow rate Q varies. The equilibrium fluidity varies with local stress as described in Eq. 4-4. The construction time is fixed at t_c = 663 s and the avalanche time t_a varies with the equilibrium fluidity, as given by Eq. 4-8.

The pressure difference predicted by the thixotropic model is compared to that obtained with the time-independent model at different flow rates, which implies different thixotropy number and dimensionless wall stress. Low flow rates correspond to low thixotropy number and dimensionless wall stress, whereas high flow rates correspond to high thixotropy number and dimensionless wall stress. The results are presented in Fig. 4.12. The ratio of the pressure difference predicted by both models is $\overline{\Delta P} \approx 1$ at the highest flow rate explored, i.e. highest thixotropy number and dimensionless wall stress. At high enough flow rates, the pressure difference predicted by both models are close; the flow behavior is well described by a simple time-independent model

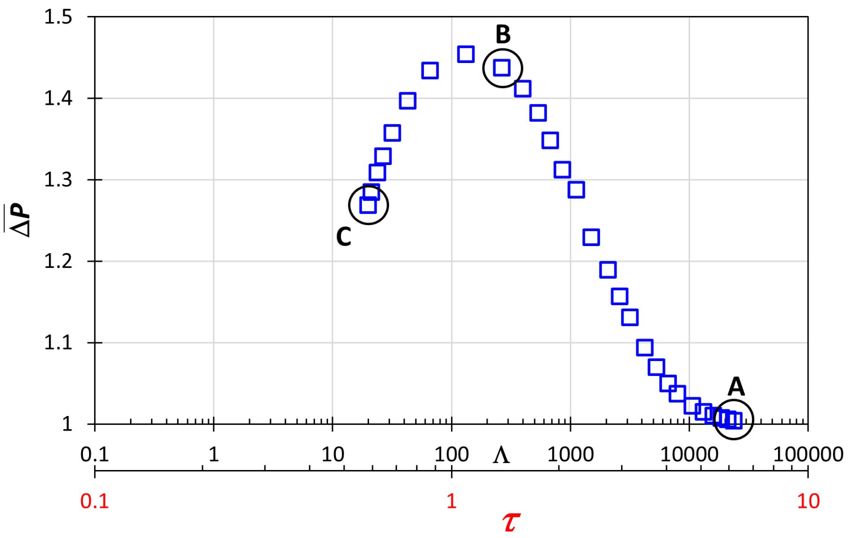

Figure 4.12: Ratio between pressure drop predicted by the thixotropic model and by the time-independent model for the laponite suspension characterized by [9] as a function of imposed flow rate, represented by Λ and τ.

and time-dependent effects can be neglected. Even though the thixotropy number is high, which would lead to very slow rate of change of the liquid structure level and therefore different flow behavior from a liquid that responds instantaneously to the imposed local stress, the very high dimensionless wall stress implies that the viscosity along the capillary wall is almost constant, in the high shear rate plateau. As the flow rate falls, $\overline{\Delta P}$ increases, reaching a maximum value of $\overline{\Delta P} \approx 1.45$ at $\Lambda \approx 10^2$ ($\tau = 1.26$). The pressure difference predicted by the thixotropic model is 45% higher than that obtained using the time-independent model. At lower flow rates, i.e. lower thixotropy number and dimensionless wall stress, the pressure difference ratio $\overline{\Delta P}$ decreases. Although solutions could not be computed below $\Lambda < 10^1$, Newton´s method does not converge, it is well known that the time-independent model predictions are recovered at vanishing flow rates; $\overline{\Delta P} \rightarrow 1$ as $\Lambda \rightarrow 0$ and $\tau \rightarrow 0$. When the residence time is much larger than the liquid characteristic time, the material has enough time to recover its equilibrium state at every point and the viscosity is only a function of the local deformation rate. This is the same behavior discussed by Jamali and McKinley [68], which show that pronounced thixotropic and hysteretic effects occur at intermediate values of the mutation number (reciprocal of the thixotropy number used here).

The viscosity fields for both time-independent model and thixotropic model at the conditions marked as A, B and C in Fig. 4.12 are presented in Fig. 4.13. At the highest flow rate explored, marked as A, $\Lambda \approx 2 \times 10^4$ and $\tau \approx 6$, the viscosity near the capillary wall is almost constant. The imposed stress

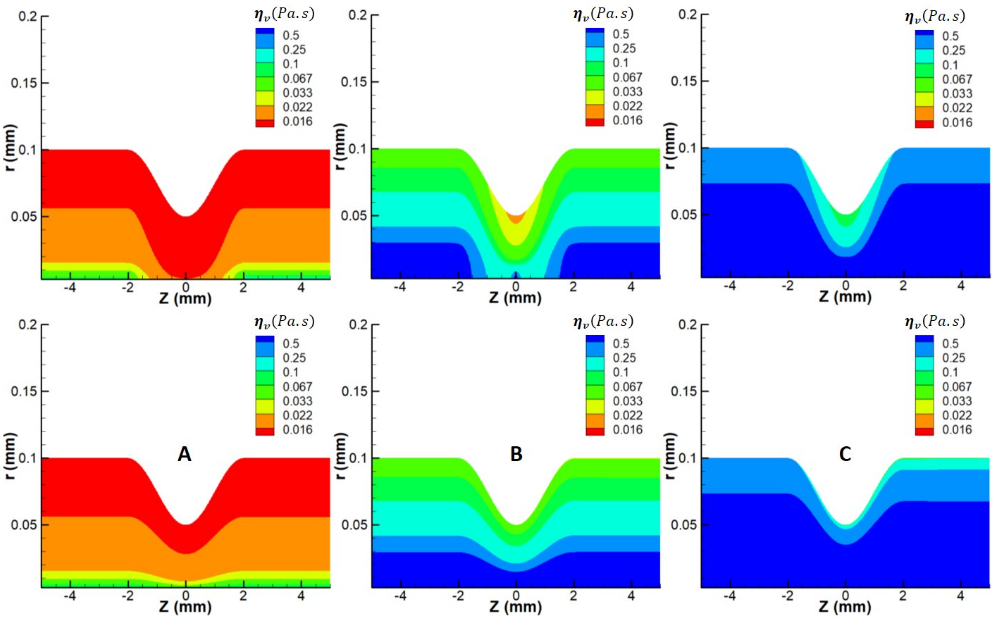

Figure 4.13: Viscosity field near the capillary constriction predicted by both the time-independent model (top row) and thixotropic model (bottom row) at different imposed flow rates: $Q = 3.5\ mm^3/s$, $\tau = 6.12$, $\Lambda = 18,500$ (left column); $Q = 5 \times 10^{-2}\ mm^3/s$, $\tau = 1.57$, $\Lambda = 264$ (center column); $Q = 3.75 \times 10^{-3}\ mm^3/s$, $\tau = 0.69$, $\Lambda = 19.8$ (right column);

along the wall, both in the straight section and in the throat, is high enough that the liquid is fully unstructured. At an intermediate value of flow rate, marked as B, $\Lambda \approx 10^2$ and $\tau \approx 1$, the viscosity near the throat predicted by the thixotropic model is much higher than that of the time-independent model. The level of structuring is high, even though the stress level is high in that region. In the limit of very low flow rate and consequently very high residence time, the liquid has enough time to reach equilibrium and the predictions obtained by both the time-independent model and the thixotropic model are similar. In that case, $\overline{\Delta P} \approx 1$. There is a range of thixotropy number and dimensionless wall stress at which the liquid time-dependency cannot be neglected. Modeling the flow taking into account only the shear dependency of the viscosity leads to inaccurate predictions.

5
Slot coating modeling

The second problem analyzed in this thesis is the flow of thixotropic liquids in a slot coating process. Slot coating is largely used in the manufacturing of functional films with particle suspensions, including battery electrodes. These slurries show thixotropic behavior, which may affect the operability limits of the process. Most analyses presented in the literature on slot coating of particle suspensions do not include time-dependent effects of the coating liquid. As in the previous chapter, two rheological models are used. One considers the thixotropic behavior of the liquid and the other is a time-independent model that neglects the time-dependent effects. Therefore, the goal of this analysis is to compare the flow behavior predicted by both models employed.

This chapter also provides the mathematical methodology, including description of the geometry and boundary conditions used.

5.1
Mathematical formulation

It was considered a small-scale, steady-state flow of a non-Newtonian liquid that exhibits shear-thinning, viscoplasticity and thixotropy.

Gravitational forces are neglected. The flow is described by incompressible mass and momentum conservation equations:

$$\nabla \cdot \boldsymbol{v} = 0 \tag{5-1}$$

and

$$\rho \boldsymbol{v} \cdot \nabla \boldsymbol{v} = \nabla \cdot \boldsymbol{T}, \tag{5-2}$$

where $\boldsymbol{v}$ is the velocity vector, ρ is the liquid density, $\boldsymbol{T}$ is the stress tensor. The stress tensor is split as $\boldsymbol{T} = -p\boldsymbol{I} + \boldsymbol{\sigma}$, where p is the pressure field, $\boldsymbol{I}$ is the identity tensor, and $\boldsymbol{\sigma}$ is the extra stress. The latter obeys Newton's law of viscosity, $\boldsymbol{\sigma} = \eta_v(\nabla \boldsymbol{v} + \nabla \boldsymbol{v}^T)$, where η_v is the local viscosity of the liquid.

5.1.1
Rheological models

Two different rheological models considered in the analysis. The first model neglects fluid time-dependent effects and assumes that the viscosity at each point is a function of the local deformation rate $\dot{\gamma}$ and yield stress σ_y. From now on, this model is referred here as the *time-independent model.*

$$\eta_v = \eta_v(\dot{\gamma}, \sigma_y) \tag{5-3}$$

The function $\eta_v(\dot{\gamma}, \sigma_y)$ is obtained experimentally and it is generally referred to as the liquid flow curve. This model is obtained by the expression of ϕ^*_{eq} in section 2.2.2. ϕ_0 was fixed in 10^{-3} $(Pa.s)^{-1}$ to ease the convergence and this value is not strictly equal to zero. In addition, the latter parameter is registered in the range reported in the literature (10^{-5} - 10^{-3} $(Pa.s)^{-1}$). The plot of ϕ^*_{eq} as a function of stress is presented in Fig. 5.1 for both yield stress values: 0 and 6 Pa, respectively. The latter corresponds to a laponite suspension obtained by Souza Mendes et al. [9].

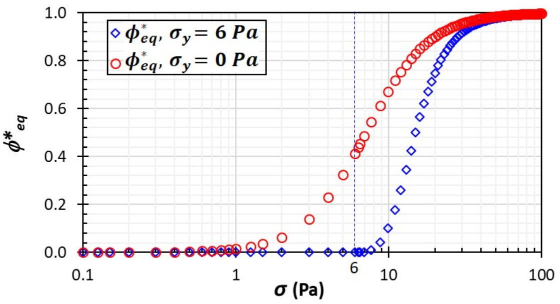

Figure 5.1: Equilibrium fluidity as function of shear stress for $\sigma_y = 0$ and 6 Pa

The fluidity equation, $\phi^*_{eq}(\sigma, \sigma_y)$, shown in Fig. 5.1, is given by:

$$\phi^*_{eq}(\sigma, \sigma_y) = \frac{\frac{1}{\sigma}\left[\frac{|\sigma - \sigma_y|}{K}\right]^{1/n} H(\sigma - \sigma_y)}{(\phi_\infty - \phi_0) + \frac{1}{\sigma}\left[\frac{|\sigma - \sigma_y|}{K}\right]^{1/n}} \tag{5-4}$$

where for the laponite suspension used as example by Souza Mendes et al. [9], $n = 0.32$, $\phi_\infty = 64.1(Pa.s)^{-1}$, and $\phi_0 = 10^{-3}(Pa.s)^{-1}$. $H(\sigma - \sigma_y)$ is a Heaviside function. In this case, it was employed a smooth Heaviside function as explained in section 4.1.1. Likewise, if $\sigma > \sigma_y$ this function is equal to 1, otherwise it is equal to zero. However, there is a smooth transition, between values of σ just before and after the yield stress, by using the following expression:

$$H(\sigma - \sigma_y) = \frac{1}{2}\{1 + tanh[m_y(\sigma - \sigma_y)]\} \tag{5-5}$$

where m_y is the steepness intensity of the smoothed Heaviside function.

Having in mind the concept of fluidity (i.e. reciprocal of viscosity) and the definition of normalized fluidity, the steady-state viscosity as a function of the local stress and yield stress is written as:

$$\eta_v(\sigma, \sigma_y) = 1/\phi_v = [\phi^*_{eq}(\sigma, \sigma_y)(\phi_\infty - \phi_0) + \phi_0]^{-1} \tag{5-6}$$

The second model takes into account the fluid time-dependent response, and is referred here as the *thixotropic model.* The mechanical response of the liquid is described by the model proposed by de Souza Mendes et al.[9]. The main advantage of this model, when compared to existing phenomenological models for thixotropic materials, is that the evolution equation that describes the microscopic state only involves material functions that are directly measurable by means of standard rheological tests. This model is described in detail in section 2.2.2. Considering a Lagrangian frame of reference, the evolution equation for fluidity is written as Eq. 5-7. The function that describes the rate of change of fluidity $F(\phi^*_v, \phi^*_{eq}(\sigma, \sigma_y))$ is written using two different functional forms, depending whether the structure is being broken or recovered, as shown in Eq. 5-8.

$$\boldsymbol{v} \cdot \nabla \phi^*_v = F(\phi^*_v, \phi^*_{eq}(\sigma, \sigma_y)) \tag{5-7}$$

where, $F(\phi^*_v, \phi^*_{eq}(\sigma, \sigma_y))$ is given by:

$$F(\phi^*_v, \phi^*_{eq}(\sigma, \sigma_y)) = \begin{cases} f_b = \frac{s}{t_a \phi^*_{eq}} (\phi^*_{eq} - \phi^*_v)^{\frac{s+1}{s}} {\phi^*_v}^{\frac{s-1}{s}}, & 0 < \phi^*_v \le \phi^*_{eq} \\ \\ f_c = -\frac{(\phi^*_v - \phi^*_{eq})}{t_c}, & \phi^*_{eq} < \phi^*_v \le 1 \end{cases} \tag{5-8}$$

where, the avalanche time t_a and the exponent s are a function of the equilibrium fluidity as shown in the previous chapter.

$$t_a(\phi^*_{eq}) = 59.2 \frac{(1 - \phi^*_{eq})^{1.1}}{{\phi^*_{eq}}^{0.4}}, \tag{5-9}$$

$$s = \frac{8}{\exp(\phi^*_{eq}/0.09) - 1} + 1.2. \tag{5-10}$$

The functional form for $\phi^*_{eq} < \phi^*_v \le 1$ represents the structure buildup dynamics. For the laponite suspension, the construction time is $t_c = 663$ s.

For simplicity $F(\phi^*_v, \phi^*_{eq}(\sigma, \sigma_y))$, from Eq. 5-8, is written as a single function (not as function by parts), as follows:

$$F(\phi_v^*, \phi_{eq}^*(\sigma, \sigma_y)) = H(\phi_v^* - \phi_{eq}^*) f_c + [1 - H(\phi_v^* - \phi_{eq}^*)] f_b \qquad (5\text{-}11)$$

where, $H(\phi_v^* - \phi_{eq}^*)$ is a smooth Heaviside function. It was used the same Heaviside function (with the same value of m) of that shown in section 4.1.1.

It is important to mention that the functional forms presented in Eq. 5-8 were proposed based on the rheological response of a laponite suspension. The functional form $F(\phi_v^*, \phi_{eq}^*(\sigma, \sigma_y))$ will change with the fluid rheological response.

5.1.2
Flow geometry and boundary conditions

We investigate the flow in slot coating process. At the feed slot, the flow kinematics show regions of fully developed flow, at which the fluidity is in equilibrium along every streamline. However, as the liquid enters into the coating bead, the initial equilibrium is perturbed. A liquid particle goes through different regions of the flow, at which the Lagrangian variation of the stress is complex. Since the thixotropic model takes into account the time response to stress changes, modeling the liquid behavior as a thixotropic fluid may lead to very different flow fields from those computed with a TIM.

A sketch of the geometry of the problem is shown in Fig. 5.2. It is possible to visualize how the domain was discretized and what boundary conditions were used. The boundary conditions are the same ones used by Rebouças et al. [35], and Siqueira and Carvalho [7].

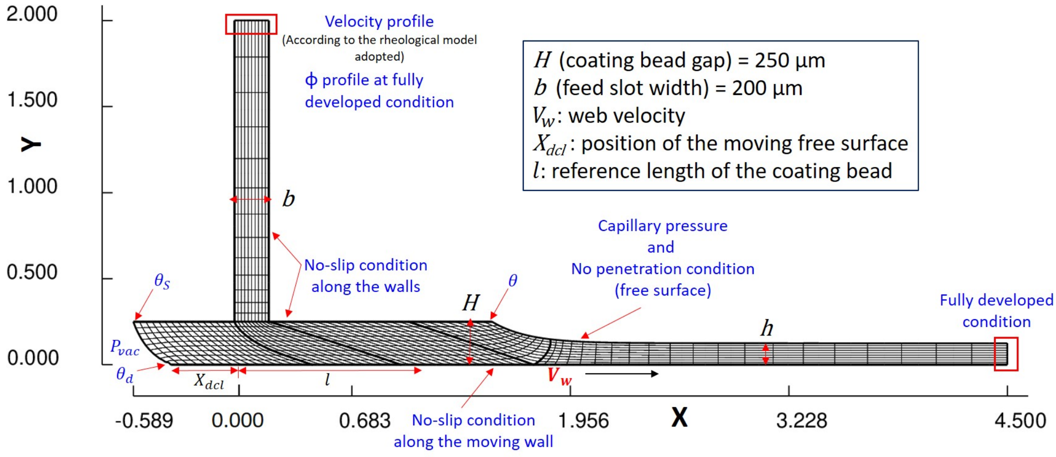

Figure 5.2: Sketch of the slot coater device simulated, including dimensions and boundary conditions

The boundary conditions that were adopted are the following:

1. *Moving substrate: No-slip and no-penetration conditions are used.*

$$u = V_w \quad ; \qquad v = 0. \tag{5-12}$$

V_w is the substrate velocity.

2. *Outflow: Fully developed flow.*

$$\hat{\boldsymbol{n}} \cdot \nabla \boldsymbol{u} = 0. \tag{5-13}$$

and $p = p_{amb}$, where p_{amb} is the ambient pressure and its manometric value is taken as a 0.

3. *Free surfaces:* The shear stress vanishes. Furthermore, there is a force balance due to the external pressure and the capillary pressure originated by the curvature of the free surface.

$$\hat{\boldsymbol{n}} \cdot \boldsymbol{u} = 0 \quad ; \quad \hat{\boldsymbol{n}} \cdot \boldsymbol{T} = \frac{1}{Ca}\frac{d\boldsymbol{t}}{ds_c} - \hat{\boldsymbol{n}} p_g. \tag{5-14}$$

$\boldsymbol{t}$ and $\boldsymbol{n}$ are the unit tangent and unit normal vector along the free surface, while s is the arc length of the free surface and Ca is the capillary number. In addition, P_g is the external gas pressure.

It is important to notice that $P_g = P_{amb}$ at the downstream free surface, while $P_g = P_{vac}$ at the upstream free surface. P_{vac} is the pressure imposed at the vacuum chamber, which is usually lower than P_{amb}. For given values of V_w and h (film thickness), the value of P_{vac} defines the position of the dynamic free surface ($\boldsymbol{X}_{dcl}$).

4. *Static contact line: Pinned at the corner of the die lip.*

$$\boldsymbol{X}_{scl} = \boldsymbol{X}_{corner}. \tag{5-15}$$

5. *At the solid walls: No-slip and no-penetration conditions are employed.*

$$u = 0; \quad v = 0 \tag{5-16}$$

6. *Inflow: Fully developed flow.*

Figure 5.3 presents a sketch of the fully-developed flow in the feed slot. q is the volumetric flow rate per unit width, an input parameter, b is the width of the feed slot, and x is considered from the center of the feed slot. As slot coating is a pre-metered method, deposited film thickness h is only a function of the imposed flowrate and web speed, $h = q/V_w$.

The region bounded between $-x_c$ and x_c in Fig. 5.3 is called unyielded region, where the liquid behaves as a rigid solid and moves at constant velocity. x_c is defined as $\frac{\sigma_y b}{2\sigma_w}$, where σ_w is the wall stress.

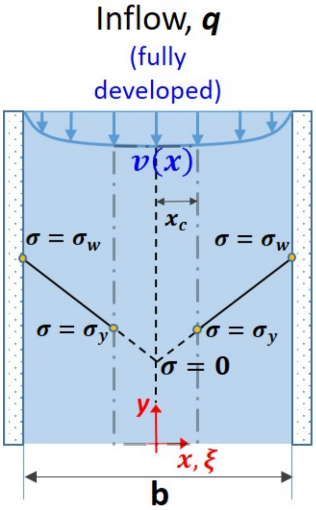

Figure 5.3: Sketch (not-to-scale) of the suspension inflow into the feed slot

It is necessary to impose a coherent velocity profile at the feed slot inlet. In fact, this velocity profile should correspond to a fully developed flow and rheologically coherent to Eq. 5-6. Nevertheless, in the case of low values of V_w and when σ_y is not considered, it is possible to use a velocity profile obtained by the Power-law model (as an approximation):

$$v = \frac{2+1/n}{1+1/n}\left(\frac{q}{b}\right)\left[\left(\frac{2x}{b}\right)^{1+1/n}-1\right] \quad ; \qquad u = 0. \tag{5-17}$$

In the case of high values V_w or when σ_y is considered, the velocity profile is obtained by numerically integrating the shear rate equation shown as follows:

$$\dot{\gamma} = -\frac{dv}{dx} = \frac{H(\sigma-\sigma_y)\sigma}{\eta_\infty + \frac{\sigma}{(\sigma/K)^{1/n}}} \tag{5-18}$$

$$v = -\int_x^{b/2} \frac{\sigma H(\sigma-\sigma_y)}{\eta_\infty + \frac{\sigma}{[(\sigma-\sigma_y)/K]^{1/n}}} dx \tag{5-19}$$

The Eq. 5-19 is obtained by integrating Eq. 5-18, considering the feed slot inlet and Cartesian coordinates. As fully developed flow is assumed, it is possible to relate the local shear stress to the wall stress as $\sigma = 2x\sigma_w/b$ (As shown in Fig. 5.3). Substituting this expression into Eq. 5-19 is obtained the velocity profile required. Considering the dimensionless length, $\xi = 2x/b$, and the Heaviside function, $H(\sigma - \sigma_y)$, the velocity profile needed is shows as:

$$v = \begin{cases} -v_{max}, & 0 \le \xi < \xi_c \\ -\frac{b}{2}\int_{\xi}^{1} \frac{1}{(\sigma_w \xi)^{-1}\eta_\infty + K^{1/n}(\sigma_w \xi - \sigma_y)^{-1/n}} d\xi, & \xi_c \le \xi \le 1 \end{cases} \tag{5-20}$$

where, ξ_c is the dimensionless form of x_c and equal to σ_y/σ_w. v_{max} is estimated as follows:

$$v_{max} = \frac{b}{2}\int_{\xi_c}^{1} \frac{1}{(\sigma_w \xi)^{-1}\eta_\infty + K^{1/n}(\sigma_w \xi - \sigma_y)^{-1/n}} d\xi \tag{5-21}$$

For a given σ_w, the velocity profile is obtained by integration as shown Eq. 5-20. The resulting velocity profile can be also integrated to get an expression which relates q and σ_w:

$$q = b\int_{0}^{1} |v| d\xi \tag{5-22}$$

As initial guess to estimate σ_w, the velocity profile obtained from the Herschel-Bulkley (HB) model is used:

$$v_{HB} = \begin{cases} -v_{max_{HB}}, & 0 \le \xi < \xi_c \\ -v_{max_{HB}}\left[1 - \frac{(\xi-\xi_c)^{1/n+1}}{(1-\xi_c)^{1/n+1}}\right], & \xi_c \le \xi \le 1 \end{cases} \tag{5-23}$$

where $v_{max_{HB}}$ is defined as:

$$v_{max_{HB}} = \frac{b}{2}\left(\frac{\sigma_w}{K}\right)^{\frac{1}{n}} \frac{1}{1/n + 1}\left[(1 - \xi_c)^{1/n+1}\right] \tag{5-24}$$

Integrating Eq. 5-23 is possible to estimate the following expression, which can be used to have an initial value of σ_w:

$$q = b v_{max_{HB}}\left[1 - \frac{1}{1/n + 2}(1 - \xi_c)\right] \tag{5-25}$$

The initial estimation of σ_w can be numerically obtained from Eq. 5-25. Then, the assumed value of σ_w is introduced in Eq. 5-20 to get an assummed velocity profile. This velocity profile is integrated by using Eq. 5-22 to get a $q_{assumed}$. Then, $q_{assumed}$ is compared to the given value of q. Since Herschel-Bulkley model tends to underestimate correct values of q, the value of σ_w is gradually increased until $q_{assumed} \approx q$.

5.1.3
Dimensionless numbers

The velocity of the moving plate (V_w) and the coating gap (H) are used as characteristic velocity and length. The flow is governed by the following dimensionless parameters:

1. Reynolds number, which represents the ratio of inertial and viscous forces, defined as:
$$Re \equiv \rho V_w H / \eta_{ref},$$
where, η_{ref} is a reference viscosity. Re ranges from about 0.127 to 1.27.

2. Capillary number, which represents the ratio of viscous and interfacial forces, defined as:
$$Ca \equiv \eta_{ref} V_w / \Gamma_s,$$
where, Γ_s is the surface tension of the liquid.

3. Gap-over-thickness ratio, defined as:
$$G = H/h,$$
where, h is the film thickness.

4. Dimensionless vacuum pressure, defined as:
$$\overline{P_v} = |P_{vac,g}| H / \Gamma.$$
where, $P_{vac,g}$ is the gauge pressure of the gas at the vacuum chamber, which is defined as: $P_{vac,g} \equiv P_{vac} - P_{atm}$. P_{vac} and P_{atm} are the absolute vacuum and atmospheric pressures, respectively.

5. Dimensionless feed slot height, defined as the ratio of feed slot width to coating gap:
$$S = b/H.$$

6. Power-law index n.

7. Structure number, which is defined as the ratio of the fluidity for a fully unstructured liquid to the fluidity for a fully structured material:
$$Str = \phi_\infty / \phi_0.$$

8. Thixotropy number, which represents the ratio of the construction time to the liquid residence time in the coating bead (or part of it), defined as:

   $$\Lambda = V_w t_c / l.$$

   This is the inverse of the Mutation number Mu, defined by Moors and Winter [67], and discussed in detail by Jamali and McKinley [68].

   In the calculations, it was used $l = 1$ mm. This parameter is the reference length of the coating bead from the beginning of the feed slot, as shown in Fig. 5.2.

All results reported here were obtained considering S=0.8 and Str=6.41×10^4.

5.2
Numerical formulation

Numerical solutions were obtained via finite element approximations of Eqs. 5-1, 5-2, 3-23 and 5-7 (when using the thixotropic model) with the appropriate boundary conditions. For slot coating results, it is necessary to determine the position of the free surfaces. This is done by a mapping between the unknown physical domain and a known computational/reference domain according to the elliptic mesh generation method.

The independent variables of the problem, i.e. velocity, pressure, fluidity (for the thixotropic model) fields, and mesh position are written as a linear combination of a finite number of basis functions. Lagrangian biquadratic functions were used to represent the velocity field and mesh position, linear discontinuous functions were used for the pressure field and Lagrangian biquadratic for the fluidity field. Galerkin's weighting functions are used in the residual equations of mass and momentum conservation, and mesh equation, whereas the stabilized Streamline-Upwind Petrov-Galerkin formulation is applied in fluidity transport equation. The upwinding parameter was defined as the characteristic size of the smallest element in the computational mesh.

The flow domain was divided into quadrangular finite elements using a computational mesh with 760 elements and 3225 nodes. In addition, the domain was divided into 6 regions. The G/SUPG FEM formulation reduces the fully coupled, non-linear model to a large, sparse set of coupled, non-linear algebraic equations with 18,405 degrees of freedom for the thixotropic model and 15,180 degrees of freedom for the time-independent model. The resulting global set of non-linear equations was solved by Newton's Method with a numerical Jacobian matrix calculated using a second-order central difference scheme. The tolerance on the L2-norm of the Newton update and of the global residual vector were both set to 10^{-6}. At each iteration of Newton's Method, the linear system was solved with a frontal solver based on the LU factorization scheme. Solutions were obtained using a computer with an Intel Core i7-7700, 3601 MHz processor, 8.00 GB (RAM), 4 Cores. Each Newton iteration took approximately 47 seconds for the thixotropic model and 4 seconds for the time-independent model.

5.3
Results and discussion

The main goal of this analysis was to evaluate the effects of thixotropy on flow pattern and process limits. The solutions obtained with the TIM were used as a base case to evaluate the time-dependent effect. All results where obtained using the rheological data of a laponite suspension obtained by Souza Mendes et al. [9]. Most results were obtained neglecting the yield stress to ease the convergence in the simulations. However, solutions considering yield stress, $\sigma_y = 6Pa$, were also obtained and presented here. The results are subdivided according to the web speed, at low capillary number, at which $V_w = 25$ mm/s, and high capillary number, at which $V_w = 250$ mm/s.

Since, the viscosity changes along the domain; it is necessary to consider a reference viscosity (η_{ref}) for a particular value of V_w to determine the dimensionless parameter of the flow. This viscosity is estimated by assuming a shear rate equal to V_w/H. The corresponding capillary numbers at $V_w =$ 25 and 250 mm/s are $Ca = 0.021$ and $Ca = 0.074$, respectively. The surface tension was set to $\Gamma = 60$ mN/m.

Other important variable computed in the numerical solutions is the position of the upstream moving free surface (X_{dcl}). Two limiting values of this variable characterize important process limits: $X_{dcl} = 0$ marks invasion of the upstream meniscus into the coating bead and characterizes the lower P_{vac} values that leads to stable process, i.e. sets the low vacuum limit. By working above this limit, the invasion of the upstream meniscus into the feed slot is avoided. On the other hand, X_{dcl}= -1.5 mm marks the invasion of the upstream meniscus into the vacuum box and corresponds to the maximum recommended P_{vac} value. Likewise, working below this limit, invasion of the liquid into the vacuum chamber is avoided.

The other important process limits is defined by the minimum film thickness (h_{min}) or the maximum G ratio. It defines the thinnest film that can be coated and it is characterized by the invasion of the downstream meniscus into the coating bead. Some slot coating operations do not make use of a vacuum box. In these cases, $P_{atm} - P_{vac} = |P_{vac,g}| = 0$ and the minimum possible film thickness when there is no vacuum pressure is represented by h_0. These process limits are represented in Fig. 5.4.

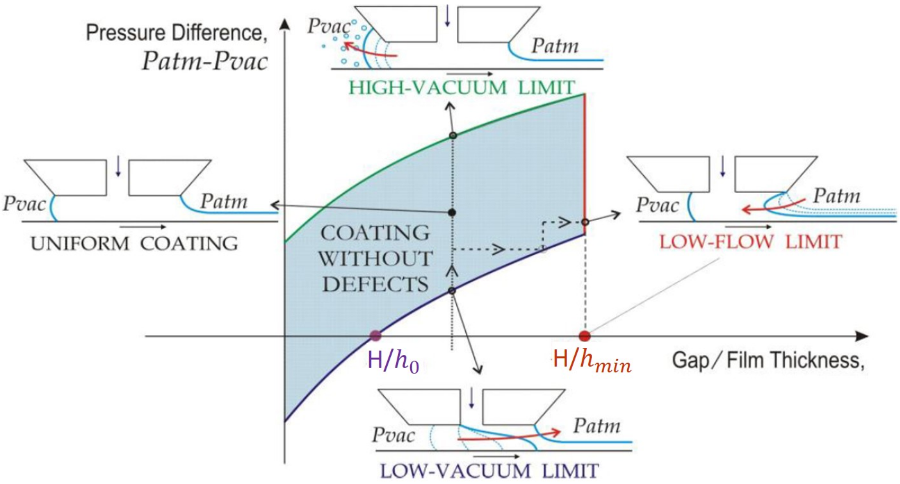

Figure 5.4: Sketch of a typical coating window for Newtonian fluids (Adapted from [8])

5.3.1
Effect of thixotropy

The flow predicted using the TIM and the thixotropic model are compared here. As discussed before, the viscosity curve considered in both models are the same. In the comparison discussed in this section, the yield stress value is set to zero.

We first focus on flow at G =2, i.e. the film thickness is equal half of the gap. At G <2, the pressure gradient is negative, the pressure in the coating bead is larger than atmospheric pressure and drives flow in the direction of the web motion. At G=2, Newtonian or time-independent liquids, and negligible

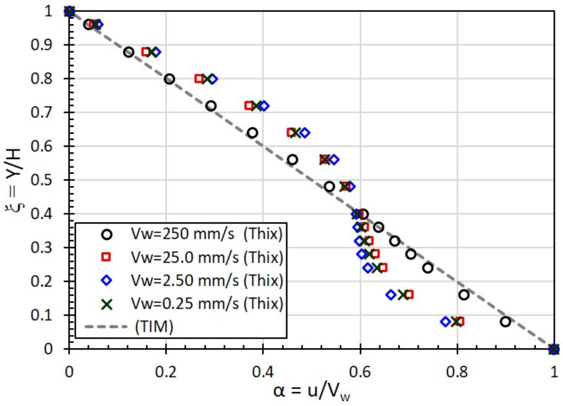

Figure 5.5: Non-dimensional velocity profiles at X=1 mm for V_w=0.25, 2.50, 25.0 and 250 mm/s.

inertial forces, the flow under the downstream die lip is a pure Couette flow. The shear rate is constant, and the velocity profile is linear, as shown in Fig. 5.5.

Figure 5.5 shows the velocity profile under the downstream die lip obtained with the time-independent model and the thixotropic model at different web speeds. The velocity profiles for the flow of the thixotropic liquid departs from linear and varies with web speed, except at the highest speed explored, e.g. $V_w = 250$ mm/s. This flow behavior can be better understood by analyzing the results presented in Fig. 5.6. The figure shows the viscosity field predicted by the time-independent model and the thixotropic model at $V_w = 25$ mm/s. In the feed slot, the viscosity fields predicted by both models are equal. The flow is fully developed, and the microstructure is in equilibrium; the viscosity is lower near the walls, where the shear rate is high, and high in the mid-plane of the feed slot, where the shear rate is zero. For the time-independent model, the viscosity is only a function of the local shear rate. Therefore, as a liquid particle leaves the feed slot and flows under that downstream die lip, its viscosity instantaneously reaches the viscosity defined by the viscosity function. Since, at $G = 2$, the shear rate is constant under the die lip, the viscosity is also constant. As a liquid particles flow from under the die lip towards the film formation region, the shear rate drops and the viscosity rises, reaching a high value as the plug flow state in the coated film is approached. For the thixotropic model, the local viscosity is not only a function of the local shear rate, but also from the stress history suffered by the liquid particle. At $V_w = 25$ mm/s, the value of the thixotropy number is $\Lambda = 1.66\times10^4$, indicating that the characteristic flow time is much shorter than the liquid characteristic time; a liquid particle does not have enough time to accommodate to a new stress level. This time-dependency is clearly illustrated in the viscosity fields of the thixotropic liquid shown in Fig. 5.6. The high value of the viscosity in the middle of the feed slot is convected through the flow. Under the downstream die lip, there is a layer of high viscosity liquid that belongs to a streamline that passes through the mid plane of the feed slot. This high viscosity layer continues to be convected in the film formation region and in the coated layer. Far downstream the coated layer, a liquid particle will have enough time to reach an equilibrium microstructure state and reach the high viscosity associated with a low shear rate (shear stress). The results clearly show that the liquid time-dependent behavior can drastically change the flow characteristics.

At higher velocity, e.g. $V_w = 250$ mm/s, the velocity profile is very close to linear, as shown in Fig. 5.5. The viscosity fields predicted by the time-independent and thixotropic models are presented in Fig. 5.7. The pattern is

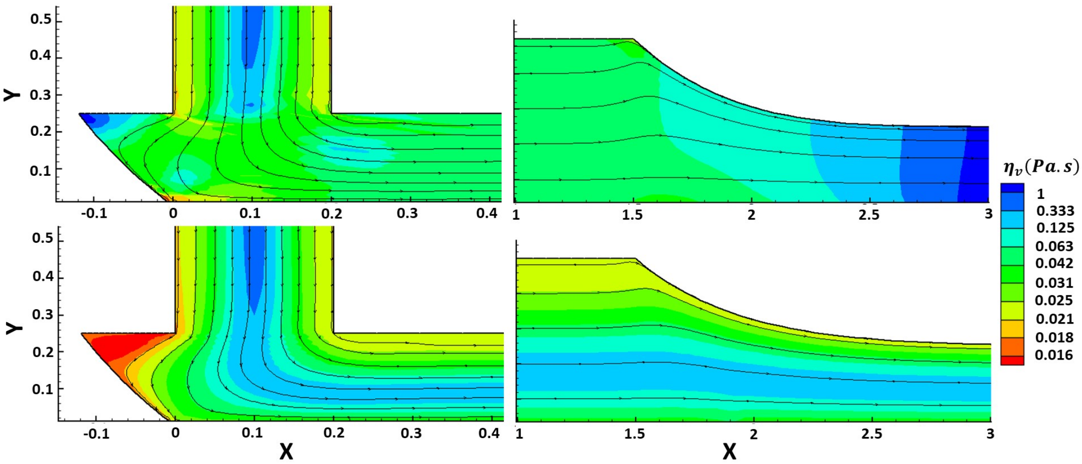

Figure 5.6: Viscosity fields predicted by both the time-independent model (top row) and thixotropic model (bottom row), near the upstream (left) and downstream (right) free surfaces, considering: V_w=25 mm/s, G=2 and X_{dcl} = 0 mm.

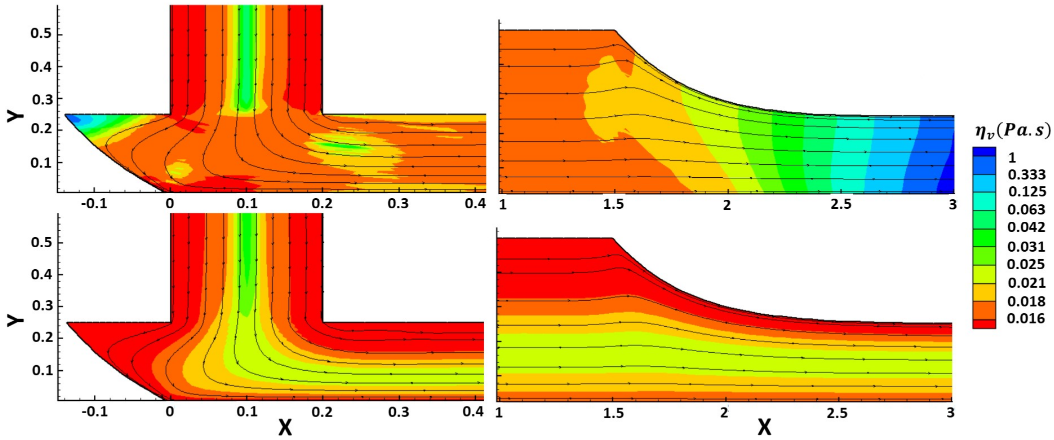

Figure 5.7: Viscosity fields predicted by both the time-independent model (top row) and thixotropic model (bottom row), near the upstream (left) and downstream (right) free surfaces, considering: V_w=250 mm/s, G=2 and X_{dcl} = 0 mm.

like the one presented in Fig. 5.6 and discussed before. However, the higher web speed requires a much higher flow rate and consequently the range of deformation rate (stress) observed in the flow is shifted to higher values, leading to a lower range of viscosity values. Therefore, despite the high value of the thixotropy number, e.g. $\Lambda = 1.66 \times 10^5$, the variation of the viscosity within the flow is weak and so is the thixotropy effect. As presented in the previous chapter, for shear thinning liquids, thixotropic effects become negligible both as $\Lambda \rightarrow 0$ or $\Lambda \rightarrow \infty$., as discussed by Jamali and McKinley [68] and Sanchez-Perez et al. [65].

5.3.1.1
Operability limits at lower web speed

The results presented in this section compares the operability limits in the plane of vacuum pressure and gap-over-thickness ratio predicted by both rheological models at low web velocity, e.g. $V_w = 25$ mm/s. The corresponding capillary and thixotropy number are $Ca = 0.021$ and $\Lambda = 1.66{\times}10^4$. The operability limits predicted by the time-independent model are presented in Fig. 5.8. The high vacuum limit (red squares) is characterized by the conditions at which the dynamic contact line position is equal the length of the upstream die lip, i.e. X_{dcl} = -1.5 mm, whereas the low vacuum limit (blue triangles) is characterized by the conditions at which the dynamic contact line reaches the feed slot, i.e. $X_{dcl} = 0$. The low flow limit (black circles) is marked by the invasion of the downstream meniscus, characterized by a low contact angle between the downstream meniscus and the downstream die lip. $|P_{vac,g}|$ is referred to the gauge vacuum pressure.

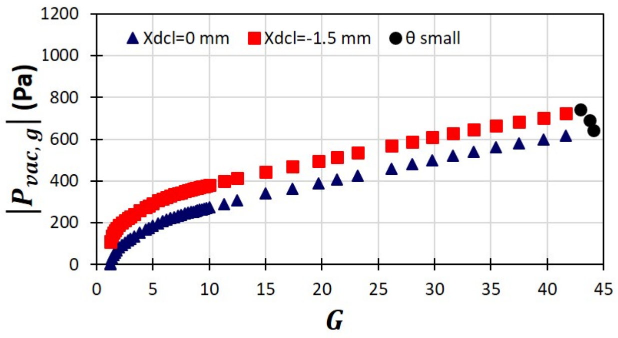

Figure 5.8: Slot coating operating window obtained from the TIM at V_w=25 mm/s.

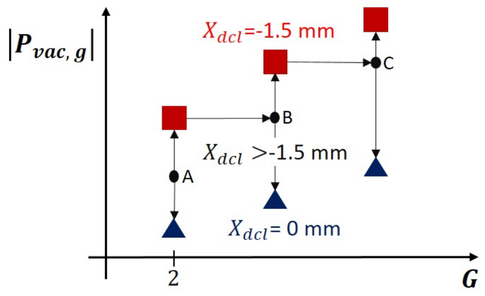

Figure 5.9: Sketch of the procedure carried out to obtain the slot coating operating windows.

The high and low vacuum limit curves were obtained from the numerical solution in the following way, as sketched in Fig. 5.9: First a stable solution at a G=2 was obtained with a value of vacuum pressure such that the dynamic contact line position was in the middle of the upstream die lip, i.e. $-1.5\ mm < X_{dcl} < 0\ mm$. This flow state is labeled A in Fig. 5.9. The value of vacuum pressure was slowly decreased, with all the other parameters fixed, until $X_{dcl} = 0$ mm. This is the first point of the low vacuum limit curve. From flow state A, the value of the vacuum pressure was also slowly increased until X_{dcl} = -1.5 mm, which defines the first point of the high vacuum limit curve. From the high vacuum limit state, the film thickness was slightly decreased, which corresponds to a small increase in the value of gap-over-thickness ratio G. As the flow rate is reduced, the dynamic contact line moves downstream, and $X_{dcl} >$ -1.5 mm. This flow state is labeled B in Fig. 5.9. From flow state B, with a higher value of G, the vacuum pressure is again decreased and increased until $X_{dcl} = 0$ mm and X_{dcl} = -1.5 mm, respectively. The procedure is repeated until numerical solutions of the differential equations could not be obtained. Figure 5.10 presents the flow at the onset of low and high vacuum limit at G = 10. The low and high vacuum pressures were $|P_{vac,g}| = 273.2$ Pa and $|P_{vac,g}|$ = 381.2 Pa, respectively.

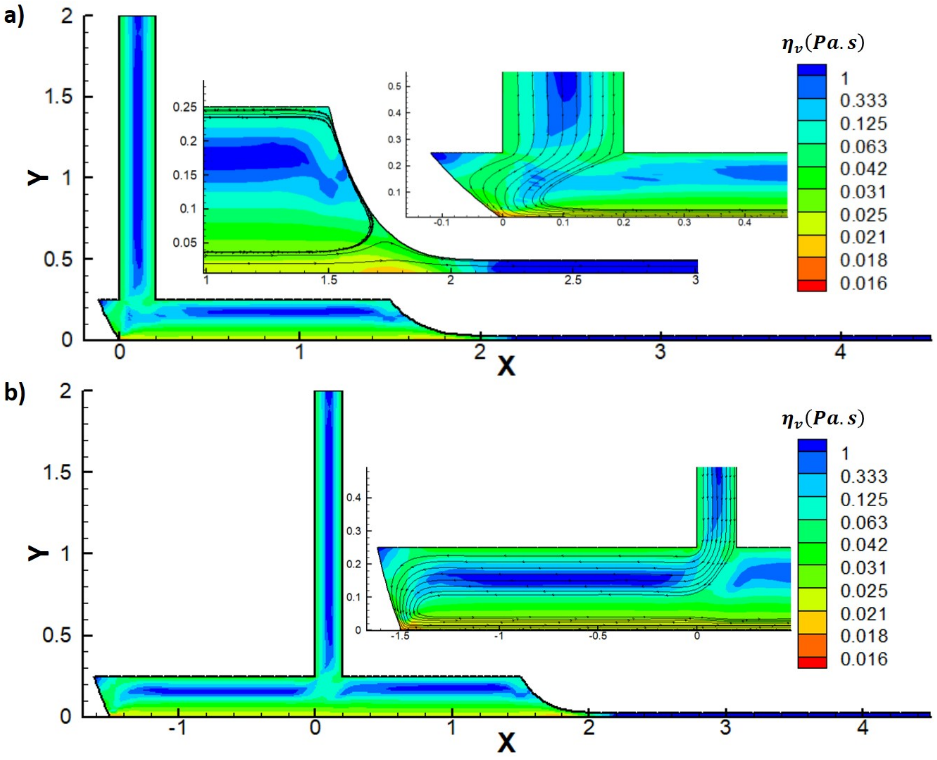

Figure 5.10: Viscosity fields according to the time-independent model for V_w=25 mm/s and G=10, at a) X_{dcl}=0 mm and b) X_{dcl}=-1.5 mm.

There is a value of gap-over-thickness ratio above which the downstream meniscus invades the coating bead, which marks the onset of the low flow limit (black circles in Fig. 5.8). At the conditions considered in this example, the low flow limit occurs at $G \approx 43$. The minimum thickness that can be coated is close to $h \approx H \ / \ 43$. Figure 5.11 illustrates the flow configuration at the onset of low flow limit.

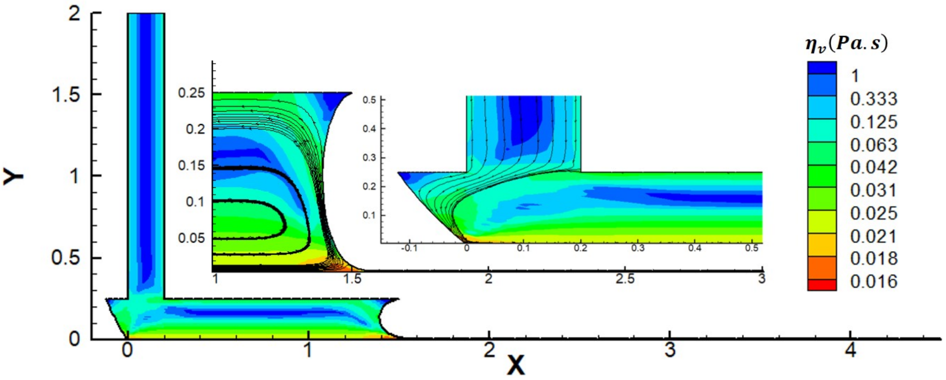

Figure 5.11: Viscosity field according to the time-independent model for V_w=25 mm/s and G=43.3 at X_{dcl}=0 mm.

From flow state A, the procedure was repeated by now lowering the gap-over-thickness G to extend the high and low vacuum limit curves to lower values of G until the later crosses the horizontal axis, which marks the maximum value of G (or minimum value of the film thickness) possible when there is no vacuum pressure. For the time-independent model used, this value was G_0 = 1.23, considering a coating gap of 100 μm, the minimum thickness that can be coated without a vacuum box is $h \approx 81$ μm. At each value of G, there is a small range of vacuum pressure at which the contact line is located on the upstream die lip and the flow is stable. The level of vacuum pressure needed rises as the film thickness becomes smaller.

The operability limits predicted when using the thixotropic model is presented in Fig. 5.12. First, the high and low vacuum limit curves predicted when using the thixotropic model were obtained following the same procedure described before and sketched in Fig. 5.9. The predicted maximum gap-over-thickness without vacuum was G_0 = 1.18. Considering a coating gap of 100 μm, if a vacuum box is not used in the process, the minimum thickness that can be coated is $h \approx 84.7$ μm.

However, at approximately $G \approx 5.5$, the procedure fails, and a solution cannot be obtained. The sequence of flow states that leads to the computation of the onset of process limits was changed and it was possible to construct the low vacuum limit curve continuously up to $G \approx 10$. From each flow state at the low vacuum limit and different values of gap-over-thickness ratio above $G \approx 5.5$, vacuum pressure was increased until X_{dcl} = -1.5 mm. Figure 5.13 presents a flow state at the high vacuum limit and G = 10. The results presented in Fig. 5.12 show an interesting phenomenon: The computed high vacuum limit curve is not continuous. The two branches of the curve were obtained

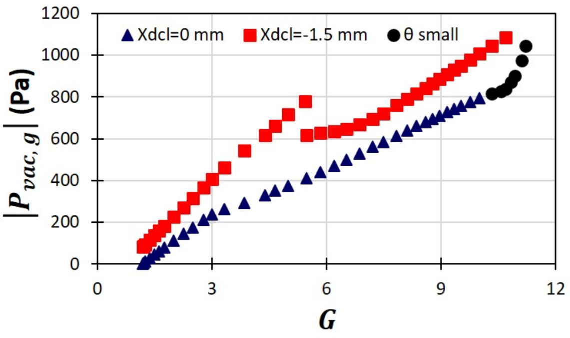

Figure 5.12: Slot coating operating window obtained from the thixotropic model at V_w = 25 mm/s.

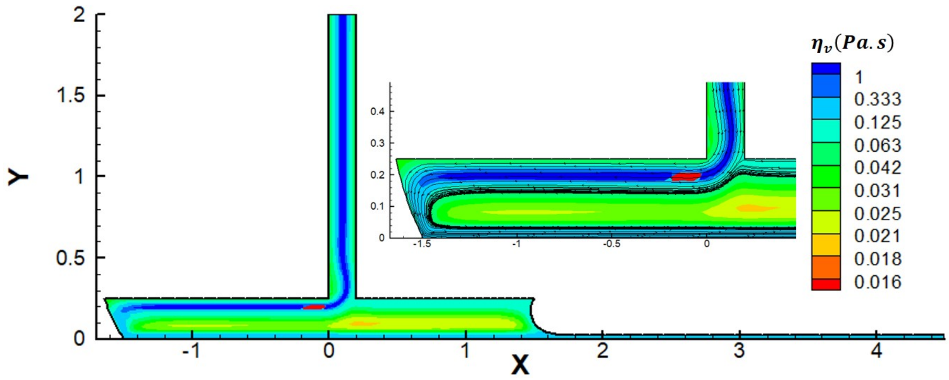

Figure 5.13: Viscosity field according to the thixotropic model for V_w=25 mm/s and G=10, at X_{dcl}=-1.5 mm.

using different continuation strategies of flow states until reaching the desired condition. Two different flow states were obtained at the same flow conditions, which indicates a hysteresis in the dynamics of the system. In practice, this hysteretic behavior may lead to oscillation between the different stable flow states. Figure 5.14 presents the two flow states computed at G = 5.45 and V_w = 25 mm/s, with X_{dcl} = -1.5 mm. The first one, Fig. 5.14a, belongs to the low G branch of the high vacuum limit curve and $|P_{vac,g}|$ = 778 Pa; and the second one, Fig. 5.14b, to the high G branch of the curve with $|P_{vac,g}|$ = 618 Pa. The figure presents the viscosity field and the streamlines near the exit of the feed slot. The main difference between the solutions is the flow pattern near the feed slot and under the upstream die lip. The higher vacuum pressure solution presented in Fig. 5.14a shows a complex recirculation pattern, with two saddle points and three recirculation centers. Part of the liquid coming out of the feed slot flows upstream, filling the upstream part of the coating bead, and part of the pumped volume flows directly downstream under the downstream die lip. The lower vacuum pressure solution presented in Fig. 5.14b presents a much simpler flow pattern. The recirculation under the upstream and downstream die lips are merged and all the liquid coming out of the feed slot flows upstream around the vortex before flowing downstream.

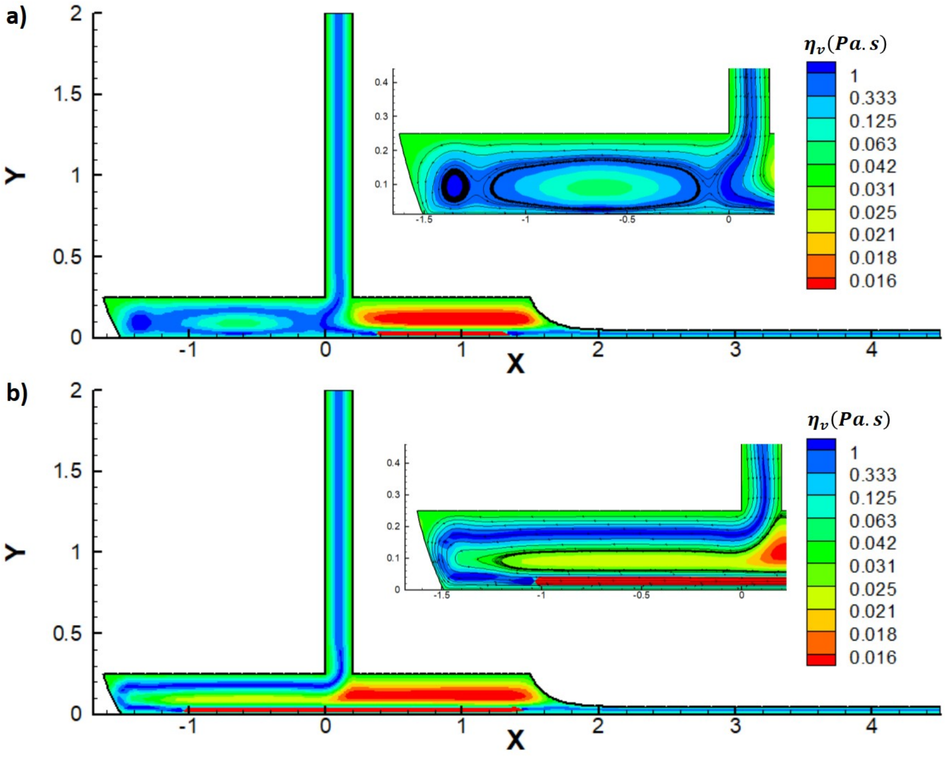

Figure 5.14: Hysteresis phenomenon for V_w=25 mm/s, G=5.45 and X_{dcl}=-1.5 mm: a) $|P_{vac,g}|$ = 778 Pa and b) $|P_{vac,g}|$ = 618 Pa

A simple comparison between the operability limits presented in Fig.5.8 and 5.12 shows that the range of operating parameters, e.g. gap-over-thickness ratio G and vacuum pressure P_{vac}, that leads to stable flow in the coating bead is remarkably different. The range of vacuum pressure required to stabilize the upstream meniscus predicted by the thixotropic model is much higher than that predicted by the time-independent model. Figure 5.15 presents the flow states computed using both rheological models at the onset of the low vacuum pressure limit, i.e. $X_{dcl} = 0$, $V_w = 25\text{mm/s}$ and $G = 10$. The necessary vacuum pressure when using the time-independent model is $|P_{vac,g}| = 273.2$ Pa, whereas it is $|P_{vac,g}| = 795$ Pa for the thixotropic model. The figure shows the computed viscosity field and the streamline pattern near the downstream meniscus and the exit of the feed slot. The viscosity near the upstream meniscus predicted by the thixotropic model is much higher than that predicted by the time-independent model. In the later, the viscosity is only a function of the local shear rate. Since the deformation rate under the die lip and close to the dynamic contact line are very high, the liquid viscosity is low in that region. With the thixotropic model, the liquid does not have enough time to change its microstructure and lower its viscosity in response to a high stress region, leading to a higher viscosity fluid near the upstream meniscus. Therefore, a higher vacuum pressure is required to push the upstream free surface upstream.

Another important difference between the two flow states is the configuration of the downstream free surface. The meniscus curvature in the time-independent model prediction is much smaller than that predicted by the thixotropic model. This can be explained also by comparing the viscosity field of both flows. It is important to remember that the downstream meniscus curvature creates the necessary adverse pressure gradient when the flow rate is low (thin coated film and high G). The more curved is the meniscus, the stronger adverse pressure gradient is formed. The deformation rate in the film formation region, e.g. 1.5 mm $< X <$ 2 mm, is high due to the strong liquid acceleration. This leads to a low viscosity region in the time-independent flow. In the thixotropic flow, the viscosity is high in this region; the liquid does not have enough time to respond to the high stress in that region. Therefore, the necessary adverse pressure gradient in the thixotropic flow is higher than that required in the time-independent flow, which explains the higher curvature of the downstream free surface. This is also clear by comparing the velocity profiles under the downstream die lip at $X = 1$ mm predicted by both models and shown in Fig. 5.16. Because of the high viscosity region near the web in the thixotropic solution, a higher adverse pressure gradient is necessary to meter the flow.

As discussed before, the configuration of the downstream meniscus has a strong effect on the onset of the low flow limit. The higher curvature of the downstream free surface observed in the thixotropic solution implies that the low flow limit occurs at lower values of the gap-over-thickness ratio, with implies that the minimum thickness that can be coated predicted with the thixotropic model is much larger than that predicted when time-dependent effects are neglected. The onset of the low flow limit predicted by the time-independent model is approximately $G = 43.3$, whereas the value predicted by the thixotropic model is close to $G = 10.3$. Considering a coating gap of 100 μm, a model that does not take into account the liquid time-dependent response predicts that the minimum thickness that can be coated at the conditions explored here is $h \approx 2.3$ μm and would require a vacuum pressure of $|P_{vac,g}| \approx 650$ Pa. When time-dependent effects are considered in the model, the predicted minimum thickness that can be coated is $h \approx 9.3$ μm and would require a vacuum pressure of $|P_{vac,g}| \approx 950$ Pa.

The results discussed in this section clearly show that at low capillary number, modeling coating flow of inelastic liquids that exhibit time-dependent behavior, as particle suspensions, with a time-independent model can lead to

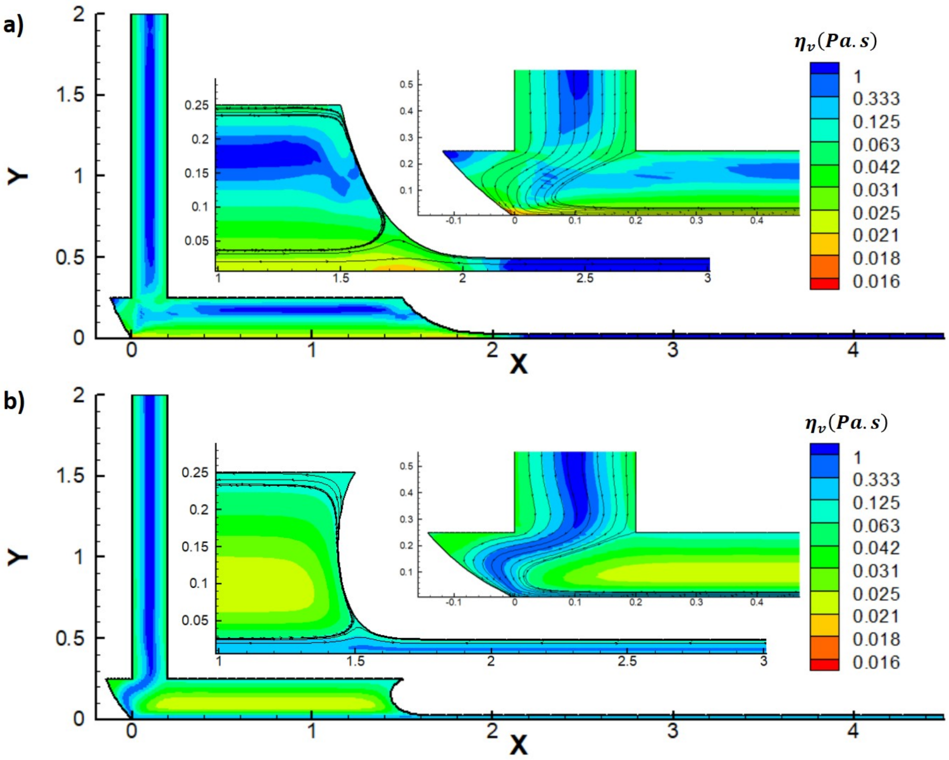

Figure 5.15: Viscosity fields according for V_w=25 mm/s, G=10 at X_{dcl}= 0 mm, according to: a) time-independent model and b) thixotropic model.

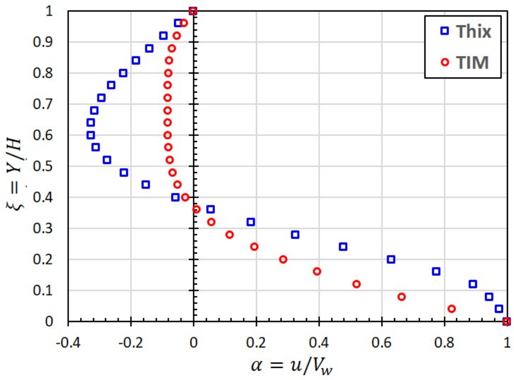

Figure 5.16: Non-dimensional velocity profile at X=1 mm, V_w=25 mm/s and G=10 obtained from the thixotropic model (Thix) and time-independent model (TIM).

very inaccurate predictions of operability window of the process. Moreover, the solutions obtained with a thixotropic model show hysteretic behavior, at which two different solutions were computed at the same set of flow parameters. This may lead to strong oscillation of the flow.

5.3.1.2
Operability limits at higher web speed

The results presented in this section compares the operability limits in the plane of vacuum pressure and gap-over-thickness ratio predicted by both rheological models at high web velocity, e.g. V_w = 250 mm/s. The corresponding capillary and thixotropy number are Ca = 0.074 and Λ = $1.66{\times}10^5$. The operability limits predicted by the time-independent model are presented in Fig. 5.17. The high vacuum limit (red squares) is characterized by the conditions at which the dynamic contact line position is equal the length of the upstream die lip, i.e. X_{dcl} = -1.5 mm, whereas the low vacuum limit (blue triangles) is characterized by the conditions at which the dynamic contact line reaches the feed slot, i.e. $X_{dcl} = 0$. The low flow limit (black circles) is marked by the invasion of the downstream meniscus, characterized by a low contact angle between the downstream meniscus and the downstream die lip.

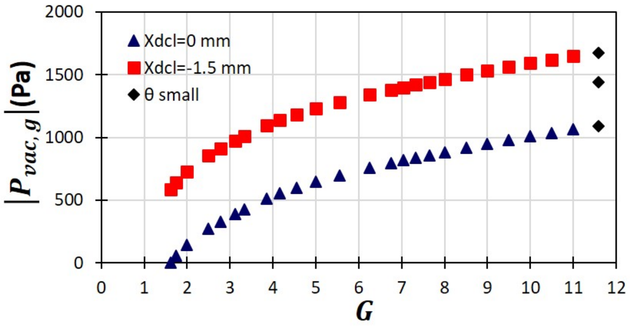

Figure 5.17: Slot coating operating window obtained from the TIM at Vw=250 mm/s.

The high and low vacuum limit curves were obtained following the same numerical solution path explained in the previous section 5.3.1.1 and sketched in Fig. 5.9. Figure 5.18 presents the flow at the onset of low and high vacuum limit at G = 7.6. The low and high vacuum pressures were $|P_{vac,g}|$ = 854 Pa and $|P_{vac,g}|$ = 1439 Pa, respectively.

There is a value of gap-over-thickness ratio above which the downstream meniscus invades the coating bead, which marks the onset of the low flow limit (black circles in Fig. 5.8). At these conditions, the low flow limit occurs at G=11.6. The minimum thickness that can be coated is close to $h \approx H$ / 11. Figure 5.19 illustrates the flow configuration at the onset of low flow limit.

According to the results presented here and the previous section, there is a much thicker h_{min} at V_w=250 mm/s compared to that at V_w=25 mm/s. In fact, the corresponding values are $h \approx H$ / 11 and $h \approx H$ / 43 respectively. The higher web speed requires much higher flow rate, which restricts the value

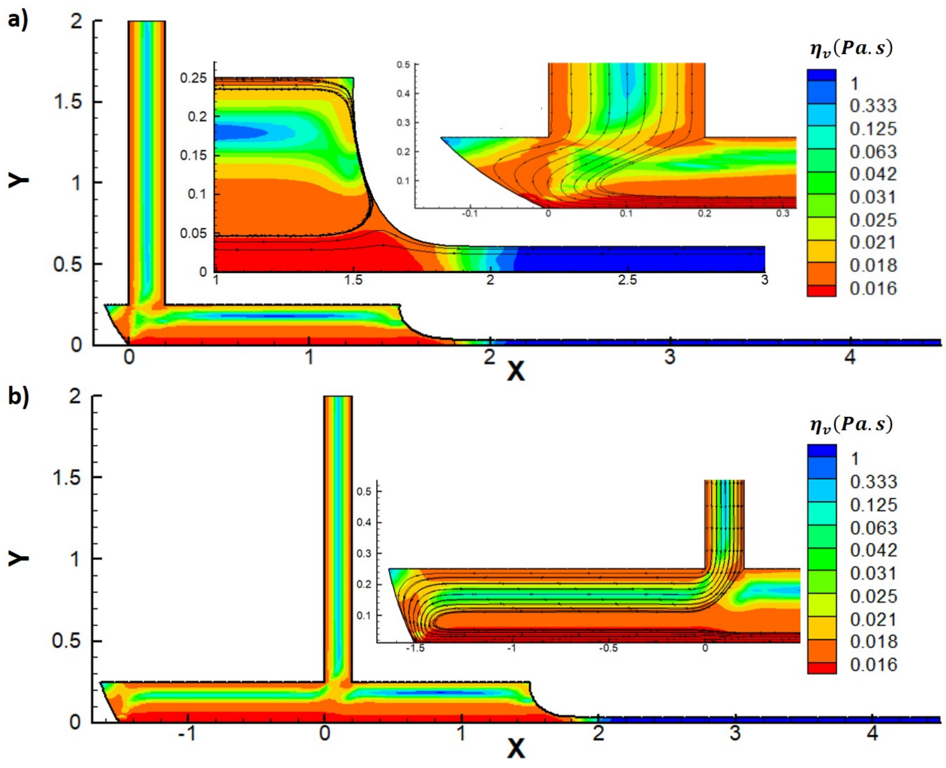

Figure 5.18: Viscosity fields according to the time-independent model for V_w=250 mm/s and G=7.6, at a) X_{dcl}=0 mm and b) X_{dcl}=-1.5 mm.

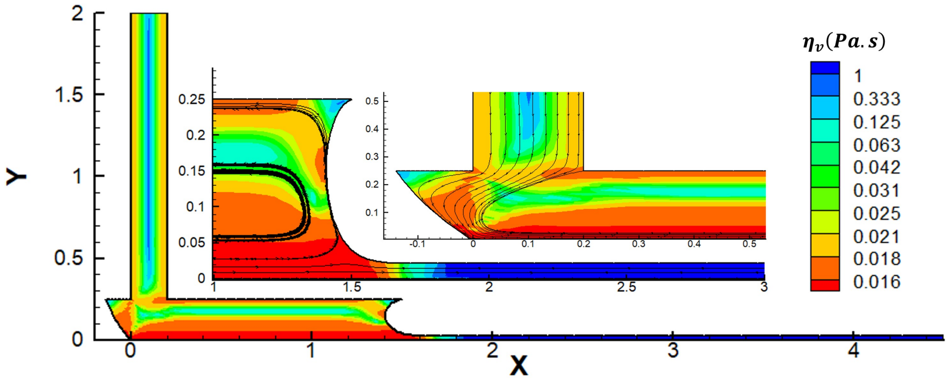

Figure 5.19: Viscosity field according to the time-independent model for V_w=250 mm/s and G=11.6 at X_{dcl}=0 mm.

of the low flow limit reported as h_{min} or the maximum value of G. As the flow rate increases at V_w= 250 mm/s and consequently the range of deformation rate (stress) observed in shifted to higher values, leading in a higher range of $|P_{vac,g}|$ in the vacuum box as reflected in Fig. 5.17.

It was also obtained the maximum value of G (or minimum value of the film thickness) possible when there is no vacuum pressure. The procedure was same followed in section 5.3.1.1. For the time-independent model used, this value was $G_0 = 1.62$, considering a coating gap of 100 μm, the minimum thickness that can be coated without a vacuum box is $h \approx 62$ μm.

The operability limits predicted when using the thixotropic model are presented in Fig. 5.20. First, the high and low vacuum limit curves predicted when using the thixotropic model were obtained following the same procedure described before and sketched in Fig. 5.9. The predicted maximum gap-over-thickness without vacuum was G_0 = 1.63. Considering a coating gap of 100 μm, if a vacuum box is not used in the process, the minimum thickness that can be coated is $h \approx 61$ μm. This value very similar to that obtained from the TIM.

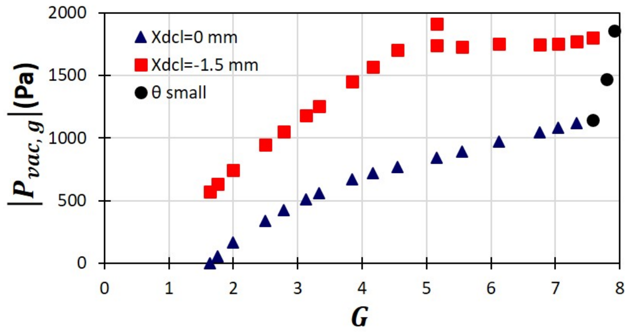

Figure 5.20: Slot coating operating window obtained from the thixotropic model at V_w=250 mm/s.

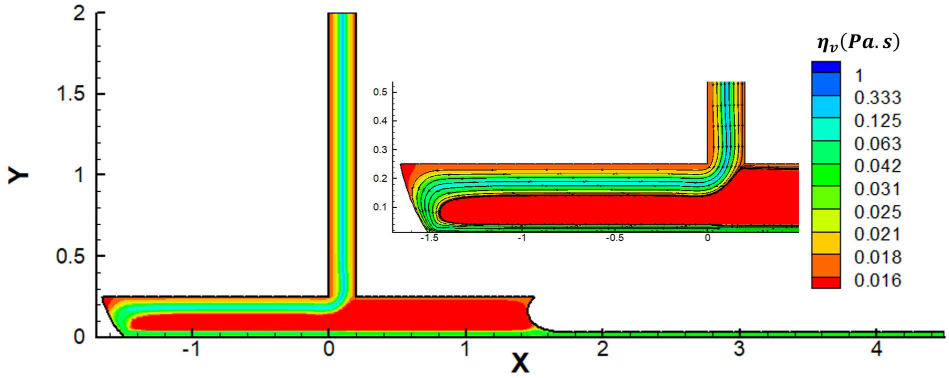

Figure 5.21: Viscosity field according to the thixotropic model for V_w=250 mm/s and G=7.6, at X_{dcl}=-1.5 mm.

However, at approximately $G \approx 5.2$, the procedure fails, and a solution cannot be obtained. The sequence of flow states that leads to the computation of the onset of process limits was changed and it was possible to construct the low vacuum limit curve continuously up to $G = 7.6$. From each flow state at the low vacuum limit and different values of gap-over-thickness ratio above $G \approx 5.2$, vacuum pressure was increased until X_{dcl} = -1.5mm. Figure 5.21 presents a flow state at the high vacuum limit and $G = 7.6$. The results presented in Fig. 5.20 show the same phenomenon presented at V_w= 25 mm/s: The computed high vacuum limit curve is not continuous. The two branches of the curve were obtained using different continuation strategies of flow states until reaching the desired condition. Two different flow states were obtained at the same flow conditions, which indicates a hysteresis in the dynamics of the system. In practice, this hysteretic behavior may lead to oscillation between the different stable flow states. Figure 5.22 presents the two flow states computed at $G = 5.2$ and $V_w = 250$ mm/s, with $X_{dcl} =$ -1.5 mm. The first one, Fig. 5.22a, belongs to the low G branch of the high vacuum limit curve and $|P_{vac,g}| = 1914$ Pa; and the second one, Fig. 5.22b, to the high G branch of the curve with $P_{vac} = 1744$ Pa. The figure presents the viscosity field and the streamlines near the exit of the feed slot. The main difference between the solutions is the flow pattern near the feed slot and under the upstream die lip. The higher vacuum pressure solution presented in Fig. 5.22a shows a complex recirculation pattern, with two saddle points and two recirculation centers. Part of the liquid coming out of the feed slot flows upstream, filling the upstream part of the coating bead, and part of the pumped volume flows directly downstream under the downstream die lip. Nevertheless, the upstream recirculation pattern shown in Fig. 5.14a at $V_w =$ 25 mm/s at is more complex than that shown in Fig. 5.22a. The lower vacuum pressure solution presented in Fig. 5.22b presents a simpler flow pattern. The recirculation under the upstream and downstream die lips are merged and all the liquid coming out of the feed slot flows upstream around the vortex before flowing downstream.

A simple comparison between the operability limits presented in Fig.5.17 and 5.20 shows that the range of operating parameters, e.g. gap-over-thickness ratio G and vacuum pressure $|P_{vac,g}|$, that leads to stable flow in the coating bead is very different. The range of vacuum pressure required to stabilize the upstream meniscus predicted by the thixotropic model is higher than that predicted by the time-independent model. Figure 5.23 presents the flow states computed using both rheological models at the onset of the low vacuum pressure limit, i.e. $X_{dcl} = 0$, $V_w = 250$ mm/s and $G = 7.6$. The necessary vacuum pressure when using the time-independent model is $|P_{vac,g}| \approx 855$ Pa, whereas it is $|P_{vac,g}| = 1146$ Pa for the thixotropic model. The figure shows the computed viscosity field and the streamline pattern near the downstream meniscus and the exit of the feed slot. The viscosity near the upstream meniscus predicted by the thixotropic model is higher than that predicted by the time-independent model. In the later, the viscosity is only a function of the local shear rate. Since the deformation rate under the die lip and close to the dynamic contact line are very high, the liquid viscosity is low in that region. With the thixotropic model, the liquid does not have enough time to change its microstructure and lower its viscosity in response to a high stress region,

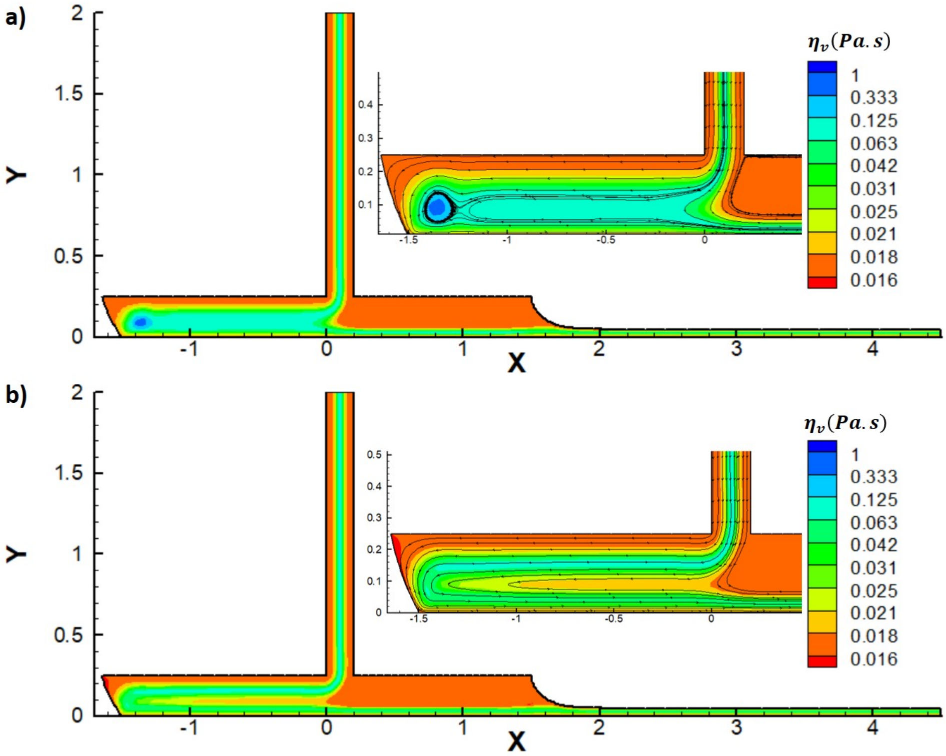

Figure 5.22: Hysteresis phenomenon for V_w=250 mm/s, G=5.16 and X_{dcl}=-1.5 mm: a) $|P_{vac,g}|$=1914 Pa and b) $|P_{vac,g}|$=1744 Pa

leading to a higher viscosity fluid near the upstream meniscus. Therefore, a higher vacuum pressure is required to push the upstream free surface upstream.

Another important difference between the two flow states is the configuration of the downstream free surface. The meniscus curvature in the time-independent model prediction is smaller than that predicted by the thixotropic model. This can be explained also by comparing the viscosity field of both flows. It is important to remember that the downstream meniscus curvature creates the necessary adverse pressure gradient when the flow rate is low (thin coated film and high G). The more curved is the meniscus, the stronger adverse pressure gradient is formed. The deformation rate in the film formation region, e.g. 1.5 mm $< X <$ 2 mm, is high due to the strong liquid acceleration. This leads to a low viscosity region in the time-independent flow. In the thixotropic flow, the viscosity is high in this region; the liquid does not have enough time to respond to the high stress in that region. Therefore, the necessary adverse pressure gradient in the thixotropic flow is higher than that required in the time-independent flow, which explains the higher curvature of the downstream free surface. This is also clear by comparing the velocity profiles under the downstream die lip at X = 1 mm predicted by both models and shown in Fig. 5.24. Because of the high viscosity region near the web in the thixotropic solution, a higher adverse pressure gradient is necessary to meter the flow.

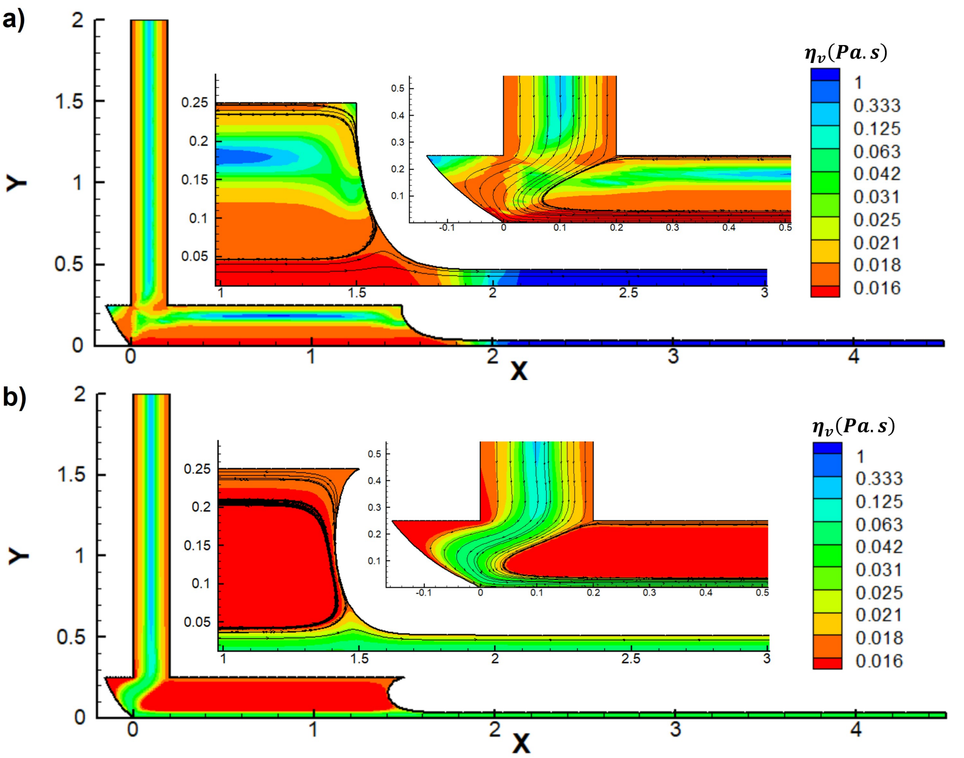

Figure 5.23: Viscosity fields according for V_w=250 mm/s, G=7.6 at X_{dcl}=-1.5 mm, according to: a) time-independent model and b) thixotropic model.

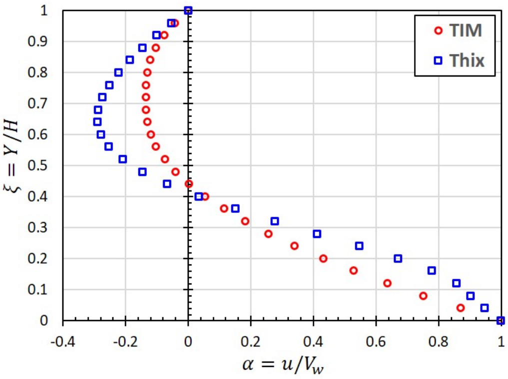

Figure 5.24: Non-dimensional velocity profile at X=1 mm, V_w=250 mm/s and G=7.6 obtained from the thixotropic model (Thix) and time-independent model (TIM).

As discussed before, the configuration of the downstream meniscus has a strong effect on the onset of the low flow limit. The higher curvature of the downstream free surface observed in the thixotropic solution implies that the low flow limit occurs at lower values of the gap-over-thickness ratio, with implies that the minimum thickness that can be coated predicted with the thixotropic model is larger than that predicted when time-dependent effects are neglected. The onset of the low flow limit predicted by the time-independent model is approximately G = 11.6, whereas the value predicted by the thixotropic model is close to $G = 7.6$. Considering a coating gap of 100 μm, a model that does not take into account the liquid time-dependent response predicts that the minimum thickness that can be coated at the conditions explored here is $h \approx 8.6$ μm and would require a vacuum pressure of $|P_{vac,g}| \approx 1088$ Pa. When time-dependent effects are considered in the model, the predicted minimum thickness that can be coated is $h \approx 13.2$ μm and would require a vacuum pressure of $|P_{vac,g}| \approx 1146$ Pa.

The results discussed in this section clearly show that at high capillary number, modeling coating flow of inelastic liquids that exhibit time-dependent behavior, as particle suspensions, with a time-independent model can lead to inaccurate predictions of operability window of the process. Moreover, the solutions obtained with a thixotropic model show hysteretic behavior, at which two different solutions were computed at the same set of flow parameters. This may lead to oscillation of the flow. Nevertheless, comparing the results at high capillary number with those at low capillary number, the results at $V_w = 250$ mm/s show a lower impact of the time dependency. For example, there is lower a difference between the low flow limit values predicted by both models. In addition, the hysteretic effect seems weaker at high capillary number.

5.3.2
Effect of yield stress

All the solutions and discussions up to this point have considered a vanishing yield stress. Particle suspension that exhibits time-dependent inelastic behavior usually also have a non-zero yield stress value. Therefore, it is important to analyze how the yield stress affects the flow pattern and process limits. Including a non-zero yield stress makes the non-linearities of the system of partial differential equations much stronger, which makes the convergence process more challenging. For that reason, we limit the analysis of the effect of yield stress to a limited number of cases.

A non-zero yield stress was included both in the time-independent and thixotropic models. We considered the value of yield stress equal to that measured for the laponite suspension analyzed by de Souza Mendes et al. [9], e.g. $\sigma_y = 6$ Pa.

First, we consider the flow at $G = 2$, at which the film thickness is half of the gap and, for time-independent model, the flow under the downstream die lip is a pure Couette flow with a linear velocity profile. Figure 5.25 presents the viscosity field and streamline patterns computed with the time-independent model at (a) $\sigma_y = 0$ and (b) $\sigma_y = 6$ Pa at the onset of the low vacuum limit, i.e. $X_{dcl} = 0$, at $V_w = 250$ mm/s. The vacuum pressure required, which represents

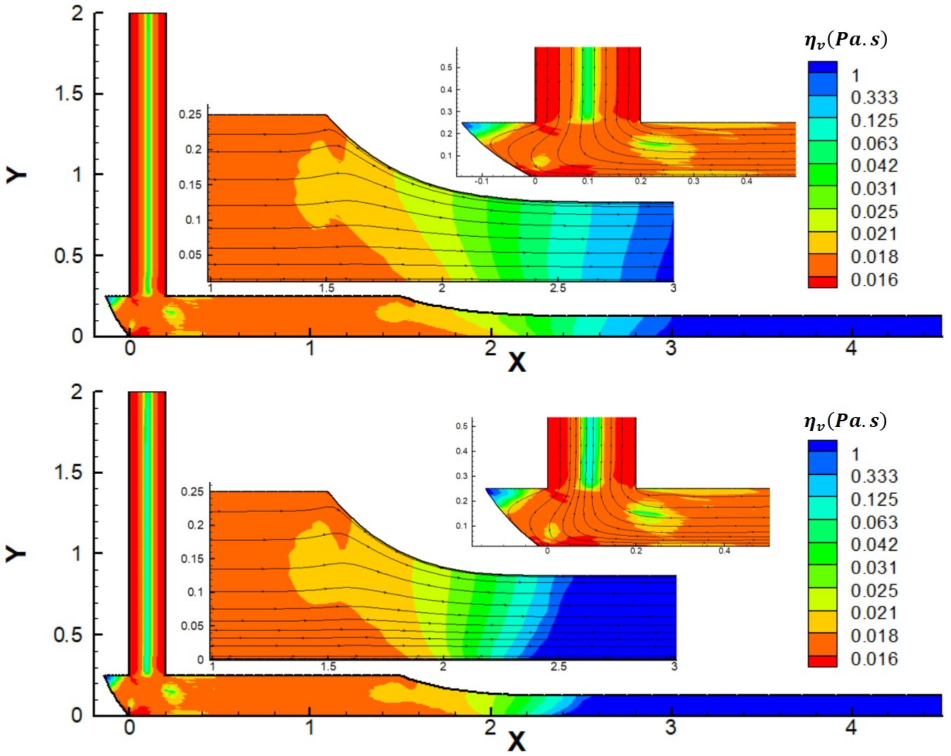

Figure 5.25: Viscosity field according to the time-independent model at V_w=250 mm/s, G=2, and X_{dcl}=0 mm; for: a) σ_y=0 Pa (top) and b) σ_y=6 Pa (bottom).

the low vacuum limit, was $|P_{vac,g}| = 142$ Pa at $\sigma_y = 0$ and $|P_{vac,g}| = 157.1$ Pa at $\sigma_y = 6$ Pa. The vacuum pressure is 10.6% higher when yield stress is considered. When considering a non-vanishing yield stress model, there are unyielded regions within the flow, at which $\sigma < \sigma_y$. The differences in the viscosity fields of both cases are small, mainly in the feed slot and in the film formation region.

The predictions obtained with the thixotropic model at the onset of low vacuum limit are presented in Fig. 5.26. When considering yield stress, the viscosity in the coating bead is higher, which requires a higher vacuum pressure. The onset of the low vacuum limit was $|P_{vac,g}| = 166$ Pa at $\sigma_y = 0$ and $|P_{vac,g}| = 206.5$ Pa at $\sigma_y = 6$ Pa; the required vacuum pressure with a non-vanishing yield stress was 24.4% higher.

The flow at $V_w = 250$ mm/s, $G = 2.8$ and high vacuum limit (X_{dcl} = -1.5 mm) predicted by the thixotropic model with (a) σ_y= 0 and (b) $\sigma_y = 6$ Pa are presented in Fig. 5.27. The onset of the high vacuum limit was $|P_{vac,g}| = 1050$ Pa at σ_y= 0 and $|P_{vac,g}| = 1239$ Pa at $\sigma_y = 6$ Pa; the required vacuum pressure with a non-vanishing yield stress was 18 % higher. There are regions of higher viscosity when yield stress is considered. This leads to a larger recirculation under both the upstream and downstream die lips.

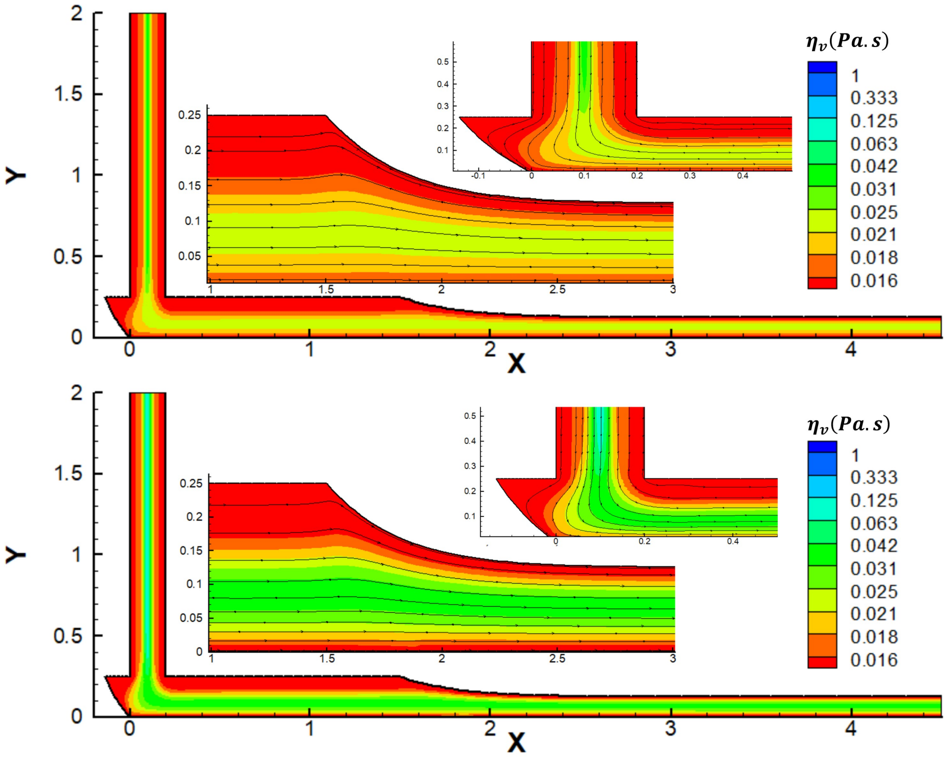

Figure 5.26: Viscosity field according to the thixotropic model at V_w=250 mm/s, G=2, and X_{dcl}=0 mm; for: a) σ_y=0 Pa (top) and b) σ_y=6 Pa (bottom).

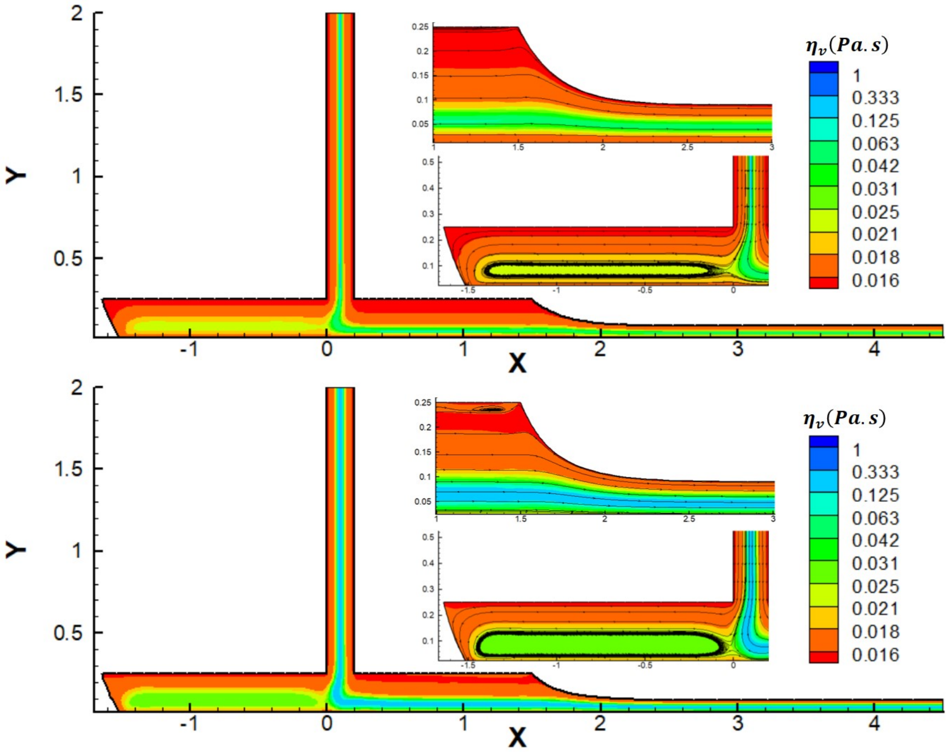

Figure 5.27: Viscosity field according to the thixotropic model at V_w=250 mm/s, G=2.8, and X_{dcl}=0 mm, for: a) σ_y=0 Pa (top) and b) σ_y=6 Pa (bottom).

6
Conclusions

In the final chapter of this thesis, the general conclusions from effects of thixotropy in complex flows are presented. Suggestions for future work are presented in section 6.3.

Small scale flows of thixotropic liquids were analyzed and the range of parameters at which neglecting time-dependent effects might lead to inaccurate results were determine. Two rheological models were used in the calculations: a thixotropic model at which time dependency is considered, and a time-independent model. The thixotropic model adopted here, was proposed by Souza Mendes et al. (2018) [9], and is based on fluidity (i.e. reciprocal of viscosity) instead of the traditional structure factor (λ). In the time-independent model, the viscosity is solely dependent on the shear stress (or shear rate). In order to illustrate time-dependent effects, the time-independent model used corresponds to the equilibrium fluidity of the thixotropic model. Both models were used to describe two small scale flows: through a constricted microcapillary and in a slot coating process, where residence times are usually very short.

6.1
Flow through a constricted capillary

In the first geometry considered, despite being simple, there are significant changes in the liquid structure state as a liquid particle flows through different regions. In fact, a fluid particle flows through a region at which the microstructure is in equilibrium (before the constriction), through a region at which the structure is destroyed (converging section) and through a region at which the microstructure is recovered (diverging section) until reaching equilibrium in the outlet tube. Due to the time dependency of the liquid, the behavior of the liquid particle in the constriction and the outlet tube may be predicted differently by the rheological model used.

According to the time-independent model, the liquid instantaneously adapts itself to the flow condition changes as it moves into the constriction. In the converging part, it is predicted a sustained decrease of viscosity as deformation rate increases. In the diverging part, it is predicted an instantaneous recovery of microstructuring level represented by a continues increase in viscosity. In both sections, it is only considered the stress imposed on the liquid particle. Eventually, the model predicts a recovery of the initial viscosity values (i.e. those before the constriction) when the liquid has just passed through the constriction and goes into the outlet tube. On the other hand, complex thixotropic flows are not steady in a Lagrangian frame of reference. In fact, a thixotropic liquid particle may not have enough time to reach the steady-state viscosity described by the rheological model at each point of the flow. Therefore, the use of time-independent models may lead to inaccurate results.

For the laponite suspension used here, as example, the thixotropic model predicts higher pressure drop at the constriction than the time-independent model does. For certain range of flow and rheological parameters, this difference could be about 50 %. It means that neglecting the liquid time-dependency could lead to very erroneous results.

However, the pressure drops at the constriction predicted by the thixotropic and time-independent models may be similar (i.e. the ratio of pressure drops may be about one). First, at low enough flow rate, the thixotropy number (i.e. ratio between liquid's characteristic time and its residence time) is low enough to allow the material to have time to achieve the equilibrium (i.e. steady-state) viscosity at each point of the flow. In the other extreme, at high enough flow rates, the dimensionless wall stress is high enough leading to a fully unstructured liquid almost everywhere within the flow upstream the constriction. Therefore, the viscosity along the microcapillary wall is almost constant and does not change near the capillary throat.

6.2
Slot coating modeling

Slot coating is largely used in the manufacturing of functional films with particle suspensions, including battery electrodes. These slurries show thixotropic behavior, which may affect the operability limits of the process. Most analyses presented in the literature on slot coating of particle suspensions do not include time-dependent effects of the coating liquid.

In the present work, the effects of thixotropy on flow pattern and process limits were analyzed. The solutions obtained with the time-independent model were used as a base case to evaluate the time-dependent effects. All results were obtained using the rheological data of a laponite suspension obtained by Souza Mendes et al. [9].

For the laponite suspension, used as example, the results reveal that modeling slot coating flow of inelastic liquids that exhibit time-dependent behavior with a time-independent model can lead to very inaccurate predictions of the operability window of the process. Moreover, the solutions obtained with the thixotropic model show hysteretic behavior, which a TIM is not able to predict. This behavior implies two different solutions at the same flow parameters, which may lead to strong oscillation of the flow.

The most remarkable differences in the prediction of operability limits were presented at the lower wed speed studied, $V_w = 25$ mm/s. For example, the low flow limit predictions were: $G \approx 43.3$ according to the time-independent model, whereas $G = 10.3$ according to the thixotropic model. Considering a coating gap of 100 μm, the model that does not take into account the time-dependent response of the thixotropic material predicts that the minimum thickness that can be coated at the conditions explored here is $h \approx 2.3$ μm and would require a vacuum pressure of $|P_{vac,g}| = 650$ Pa. When time-dependent effects are considered in the model, the predicted minimum thickness that can be coated is $h \approx 9.3$ μm and would require a vacuum pressure of $|P_{vac,g}| = 950$ Pa.

6.3
Future work

Experimental work, in both constricted capillary and slot coating, could be beneficial to validate the results properly.

It could be also very interesting to run the simulations in other geometries with higher range of flow rate conditions. It might also be beneficial to include data from various particle suspensions.

Bibliography

[1] CHHABRA, R.P.; RICHARDSON, J.F.. **Non-Newtonian Flow and Applied Rheology: Engineering Applications**. Butterworth-Heinemann, 2008.

[2] BARNES, H. A.. **Thixotropy—a review**. Journal of Non-Newtonian Fluid Mechanics, 70(1):1–33, 1997.

[3] BONN, D.; DENN, M.. **Yield stress fluids slowly yield to analysis**. Science, 324(5933):1401–1402, 2009.

[4] JFE TECHNO-RESEARCH CORPORATION. **Battery and capacitor prototyping**. `https://www.jfe-tec.co.jp/en/battery/trial/coating-materials.html`, 2023. Accessed: 2023-13-01.

[5] MEWIS, J.; WAGNER, N. J.. **Thixotropy**. Advances in Colloid and Interface Science, 147-148:214–227, 2009. Colloids, polymers and surfactants.Special Issue in honour of Brian Vincent.

[6] GRILLET, A. M.; RAO, R. R.; ADOLF, D. B.; KAWAGUCHI, S. ; MONDY, L. A.. **Practical application of thixotropic suspension models**. Journal of Rheology, 53(1):169–189, 2009.

[7] SIQUEIRA, I. R.; CARVALHO, M. S.. **A computational study of the effect of particle migration on the low-flow limit in slot coating of particle suspensions**. Journal of Coatings Technology and Research, p. 1–10, 2019.

[8] VALDEZ, L. D.. **Slot coating of particle suspensions**. Master's thesis, Pontificia Universidade Catolica do Rio de Janeiro, Rio de Janeiro, Brasil, 2013.

[9] DE SOUZA MENDES, P. R.; ABEDI, B. ; THOMPSON, R. L.. **Constructing a thixotropy model from rheological experiments**. Journal of Non-Newtonian Fluid Mechanics, 261:1–8, 2018.

[10] DE SOUZA MENDES, P. R.. **Modeling the thixotropic behavior of structured fluids**. Journal of Non-Newtonian Fluid Mechanics, 164(1):66–75, 2009.

[11] OSTWALD. **De Waele-Ostwald equation**. Kolloid Zeitschrift, 47:176–187, 1929.

[12] YASUDA, K.; ARMSTRONG, R. ; COHEN, R.. **Shear flow properties of concentrated solutions of linear and star branched polystyrenes**. Rheologica Acta, 20:163–168, 1981.

[13] BINGHAM, E.. **An investigation of the laws of plastic flow**. Bulletin of the Bureau of Standards, 13(2):309–353, 1916.

[14] HERSCHEL, W. H.; BULKLEY, R.. **Konsistenzmessungen von gummibenzollösungen**. Kolloid-Zeitschrift, 39:291–300, 1926.

[15] LIN, Y.; ZHU, H.; WANG, W.; CHEN, J.; PHAN-THIEN, N. ; PAN, D.. **Rheological behavior for laponite and bentonite suspensions in shear flow**. AIP Advances, 9(12):125233, 2019.

[16] FREUNDLICH, H.. **Thixotropy**. Hermann et Cie, Paris, 2008.

[17] PETERFI, T.. **Die abhebung der befruchtungsmembran bei seeigeleiern : Eine kolloidchemische analyse des befruchtungsvorganges**. Wilhelm Roux Arch Entwickl Mech Org., 112(1):660–695, 1927.

[18] LARSON, R. G.; WEI, Y.. **A review of thixotropy and its rheological modeling**. Journal of Rheology, 63(3):477–501, 2019.

[19] DE SOUZA MENDES, P. R.. **Thixotropic elasto-viscoplastic model for structured fluids**. Soft Matter, 7:2471–2483, 2011.

[20] SOCHI, T.. **Non-Newtonian flow in porous media**. Polymer, 51(22):5007–5023, 2010.

[21] VARCHANIS, S.; MAKRIGIORGOS, G.; MOSCHOPOULOS, P.; DIMAKOPOULOS, Y. ; TSAMOPOULOS, J.. **Modeling the rheology of thixotropic elasto-visco-plastic materials**. Journal of Rheology, 63(4):609–639, 2019.

[22] EWOLDT, R. H.; MCKINLEY, G. H.. **Mapping thixo-elasto-visco-plastic behavior**. Rheologica Acta, 56(3), 2017.

[23] DE SOUZA MENDES, P. R.; THOMPSON, R. L.. **A critical overview of elasto-viscoplastic thixotropic modeling**. Journal of Non-Newtonian Fluid Mechanics, 187-188:8–15, 2012.

[24] DE SOUZA MENDES, P. R.; THOMPSON, R. L.. **A unified approach to model elasto-viscoplastic thixotropic yield-stress materials and apparent yield-stress fluids**. Rheologica Acta, 52:673–694, 2013.

[25] MUELLER, S.; LLEWELLIN, E. W. ; MADER, H. M.. **The rheology of suspensions of solid particles**. Proceedings of the Royal Society A: Mathematical, Physical and Engineering Sciences, 466(2116):1201–1228, 2010.

[26] DAINTITH, J.. **A Dictionary of Chemistry**. Oxford Press, Oxford-United Kingdom, 2008.

[27] MOAN, M.; AUBRY, T. ; BOSSARD, F.. **Nonlinear behavior of very concentrated suspensions of plate-like kaolin particles in shear flow**. Journal of Rheology, 47(6):1493–1504, 2003.

[28] VOLTZ, C.; NITSCHKE, M.; HEYMANN, L. ; REHBERG1, I.. **Thixotropy in macroscopic suspensions of spheres**. Physical Review E, 65:051402, 2002.

[29] EINSTEIN, A.. **Eine neue bestimmung der moleküldimensionen**. Annalen der Physik, 1911.

[30] KRIEGER, I.; DOUGHERTY, T.. **A mechanism for non-Newtonian flow in suspensions of rigid spheres**. Trans. Soc. Rheol., 3:137–148, 1959.

[31] SANTAMARÍA-HOLEK, I.; MENDOZA, C.. **The rheology of concentrated suspensions of arbitrarily-shaped particles**. Colloid Interface Sci, 346(1):118–126, 2010.

[32] PHILLIPS, R. J.; ARMSTRONG, R. C.; BROWN, R. A.; GRAHAM, A. L. ; ABBOTT, J. R.. **A constitutive equation for concentrated suspensions that accounts for shear-induced particle migration**. Physics of Fluids A: Fluid Dynamics, 4(1):30–40, 1992.

[33] FONSECA, C.; FREY, S.; NACCACHE, M. F. ; DE SOUZA MENDES, P. R.. **Flow of elasto-viscoplastic thixotropic liquids past a confined cylinder**. Journal of Non-Newtonian Fluid Mechanics, 193:80–88, 2013. Viscoplastic Fluids: From Theory to Application.

[34] KISLER, S. F.; SCHWEIZER, P. M.. **Coating science and technology: An overview**. In: Kistler, S. F.; Schweizer, P. M., editors, LIQUID FILM

COATING: SCIENTIFIC PRINCIPLES AND THEIR TECHNOLOGICAL IMPLICATIONS, chapter 1, p. 137–183. Springer Netherlands, Dordrecht, 1997.

[35] REBOUÇAS, R.; SIQUEIRA, I. ; CARVALHO, M.. **Slot coating flow of particle suspensions: Particle migration in shear sensitive liquids**. Journal of Non-Newtonian Fluid Mechanics, 258:22–31, 2018.

[36] YOON, J.; KIM, D.; LEE, S.-H.; KANG, D. ; NAM, J.. **Simplified model for operability window of slot coating without vacuum**. Chemical Engineering Science, 259:117766, 2022.

[37] CARVALHO, M. S.; KHESHGI, H. S.. **Low-flow limit in slot coating: Theory and experiments**. AIChE Journal, 46(10):1907–1917, 2000.

[38] DING, X.; LIU, J. ; HARRIS, T. A. L.. **A review of the operating limits in slot die coating processes**. AIChE Journal, 62(7):2508–2524, 2016.

[39] GATES, I. A.. **Slot Coating Flows: Feasibility, Quality**. PhD thesis, University of Minnesota, Minneapolis, United States, 1999.

[40] HIGGINS, B.; SCRIVEN, L.. **Capillary pressure and viscous pressure drop set bounds on coating bead operability**. Chemical Engineering Science, 35(3):673–682, 1980.

[41] RUSCHAK, K. J.. **Limiting flow in a pre-metered coating device**. Chemical Engineering Science, 31:1057–1060, 1976.

[42] TSUDA, T.. **Coating flows of power-law non-newtonian fluids in slot coating**. Journal of the Society of Rheology, Japan, 38(4-5):223–230, 2010.

[43] KOH, H. J.; KWON, I.; JUNG, H. W. ; HYUN, J. C.. **Operability window of slot coating using viscocapillary model for carreau-type coating liquids**. Korea-Australia Rheology Journal, 24(2):137–141, 2012.

[44] CREEL, E. B.; TJIPTOWIDJOJO, K.; ALEX LEE, J.; LIVINGSTON, K. M.; RANDALL SCHUNK, P.; BELL, N. S.; SEROV, A. ; WOOD III, D. L.. **Slot-die-coating operability windows for polymer electrolyte membrane fuel cell cathode catalyst layers**. Journal of Colloid and Interface Science, 610:474–485, 2022.

[45] LEE, Y. W.; AHN, W.-G.; NAM, J.; JUNG, H. W. ; HYUN, J. C.. **Operability windows in viscoelastic slot coating flows using a simplified viscoelastic-capillary model**. Rheol Acta, 56:707–717, 2017.

[46] LINK, F. B.; FREY, S.; THOMPSON, R. L.; NACCACHE, M. F. ; DE SOUZA MENDES, P. R.. **Plane flow of thixotropic elasto-viscoplastic materials through a 1:4 sudden expansion**. Journal of Non-Newtonian Fluid Mechanics, 220:162–174, 2015. Viscoplastic fluids: From theory to application 2013.

[47] SLIBAR, A.; PASLAY, P. R.. **Intern Symp on Second Order Effects in Elasticity, Plasticity and Fluid Dynamics**. Pergamon Press, 1964.

[48] HARRIS, J.. **A continuum theory of time-dependent inelastic flow**. Rheol Acta, 6(2):6–12, 1967.

[49] MONTES, S.; WHITE, J. L.. **Rheological models of rubber-carbon black compounds: low interaction viscoelastic models and high interaction thixotropic - plastic - viscoelastic models**. Journal of Non-Newtonian Fluid Mechanics, 49(2):277–298, 1993.

[50] MEWIS, J.; WAGNER, N. J.. **Colloidal Suspension Rheology**. Cambridge Series in Chemical Engineering. Cambridge University Press, 2011.

[51] DE SOUZA MENDES, P. R.; DUTRA, E. S. S.. **Viscosity function for yield-stress liquids**. Applied Rheology, 14(6):296–302, 2004.

[52] FREDRICKSON, A. G.. **A model for the thixotropy of suspensions**. AIChE Journal, 16(3):436–441, 1970.

[53] BIRD, R. B.; ARMSTRONG, R. C. ; HASSAGER, O.. **Dynamics of polymeric liquids. Vol. 1, 2nd Ed. : Fluid mechanics**. John Wiley & Sons, United States, 1987.

[54] HIRSCH, C.. **Numerical Computation of Internal and External Flows, Vol. 1: Fundamentals of Computational Fluid Dynamics**. BH, Oxford, UK, 2nd edition, 2007.

[55] REDDY, J. N.; GARTLING, D. K.. **The finite element method in heat transfer and fluid dynamics**. CRC Press, Boca Raton, FL-United States, 3rd ed. edition, 2010.

[56] CARVALHO, M. S.; VALERIO, J. V.. **Introdução ao Método de Elementos Finitos: Aplicação em Dinâmica dos Fluidos**. SBMAC, Sao Carlos, Brazil, 2012.

[57] SIQUEIRA, I.. **Slot coating flows of elliptical particle suspensions**. Master's thesis, Pontificia Universidade Catolica do Rio de Janeiro, Rio de Janeiro, Brasil, 2016.

[58] ROMERO GUZMAN, O. J.. **Limite de Vazão Mínima do Processo de Revestimento por Extrusão de Solucões Poliméricas**. PhD thesis, Pontificia Universidade Catolica do Rio de Janeiro, Rio de Janeiro, Brasil, 2003.

[59] KISTER, S. F.. **The Fluid Mechanics of Curtain Coating and related Viscous Free Surface Flows with Contact Lines**. PhD thesis, University of Minnesota, Minneapolis, United States, 1983.

[60] KISTER, S. F.; SCRIVEN, L. E.. **Coating flow theory by finite element and asymptotic analysis of the navier-stokes system**. International Journal for Numerical Methods in Fluids, 4:207–229, 1984.

[61] CHRISTODOULOU1992, K. N.. **Computational Physics of Slide Coating Flow**. PhD thesis, University of Minnesota, Minneapolis, United States, 1990.

[62] CHRISTODOULOU, K. N.; SCRIVEN, L. E.. **Discretization of free surface flows and other moving boundary problems**. Journal of Computational Physics, 99:39 – 55, 1992.

[63] DE ALMEIDA, V. F.; SCRIVEN, L. E.. **Domain deformation mapping: application to variational mesh generation**. Journal of Scientific Computing, 20:1252–1275, 1999.

[64] HOOD, P.. **Frontal solution program for unsymmetric matrices**. International Journal for Numerical Methods in Engineering, 10:379–399, 1976.

[65] SANCHEZ-PEREZ, C.; MAZA, D.; DE SOUZA MENDES, P. R. ; CARVALHO, M. S.. **Is thixotropy important in small-scale, steady-state flow modeling?** Journal of Non-Newtonian Fluid Mechanics, 313:104991, 2023.

[66] GASPER, G.; RAHMAN, M.. **Basic Hypergeometric Series**. Encyclopedia of Mathematics and its Applications. Cambridge University Press, 2 edition, 2004.

[67] MOURS, H.; WINTER, H.. **Time-resolved rheometry**. Rheological Acta, 33(5):385–397, 1994.

[68] JAMALI, S.; MCKINLEY, G. H.. **The mnemosyne number and the rheology of remembrance**. Journal of Rheology, 66(5):1027–1039, 2022.